Generation of High Power Single-cycle and Multiple-cycle Terahertz Pulses

by

Zhao Chen

Submitted to the Department of Chemistry
in partial fulfillment of the requirements for the degree of

Master of Science

at the

MASSACHUSETTS INSTITUTE OF TECHNOLOGY

February 2013

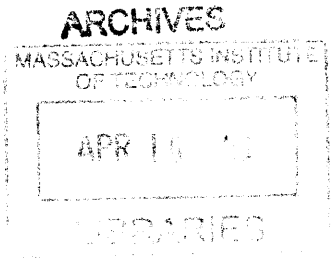

Author .....
Department of Chemistry
February, 2013

Certified by .....
Keith A. Nelson
Professor of Chemistry
Thesis Supervisor

Accepted by .....
Robert W. Field
Chairman
Departmental Committee on Graduate Students

DISCLAIMER

MISSING PAGE(S)

4-7

Generation of High Power Single-cycle and Multiple-cycle Terahertz Pulses

by

Zhao Chen

Submitted to the Department of Chemistry
on February, 2013, in partial fulfillment of the
requirements for the degree of
Master of Science

Abstract

In this thesis, we present experimental methods and results of tabletop generation of high power single-cycle and frequency-tunable multiple-cycle terahertz (THz) pulses pumped with near-infrared ultrashort optical pulses at 1 kHz and 10 Hz repetition rates. Single-cycle THz pulses with sub-picosecond duration and more than 50 μJ pulse energy, and multiple-cycle THz pulses with picosecond duration and more than 10 μJ pulse energy, are achieved respectively. These THz outputs are very close approximations to Gaussian beams, and can be well collimated and focused into samples for time-resolved spectroscopic experiments. This may allow for explorations in coherent nonlinear spectroscopy in the THz region such as the photon echo and multidimensional spectroscopy, revealing novel phenomena in solids, liquids, gases, and complex materials.

Thesis Supervisor: Keith A. Nelson
Title: Professor of Chemistry

DISCLAIMER

MISSING PAGE(S)

4-7

Contents

List of Figures

List of Tables

Chapter 1

Introduction

The modern spectroscopy and light-matter interactions began in the 1950s with the invention of the maser and laser technologies. This has facilitated numerous scientific and technological explorations in atomic and molecular spectroscopy, nonlinear optical phenomena, precision measurement and engineering, and quantum computations due to the newly accessible high-intensity, narrow spectral width, and phase coherence. The advent of ultrashort laser pulses allowed for the observation of many fascinating dynamic processes in solids, liquids, glassy states, complex materials and structures that typically occur on the order of nanoseconds, picoseconds, or even a few femtoseconds. Some examples of these processes include strongly correlated electron systems, molecular vibrations and relaxations, transient optical nonlinearity, and multiple-quantum coherence. In the electromagnetic and mechanical spectra, elementary excitations in condensed matter materials cover a wide range of frequencies, from megahertz (MHz) to gigahertz (GHz) for acoustic phonons, terahertz (THz) for optic phonons and phonon-polaritons, infrared for intramolecular vibrations, and visible to ultraviolet for electronic energy levels. While many light sources and experimental methods have been successfully developed to excite and probe these dynamics at the microscale, coherent radiation and applications in the THz region have remained relatively unexplored until the recent decades due to the challenges of generating and guiding high-energy, efficient THz sources.

In this thesis, we present and demonstrate a few experimental techniques for the

generation and enhancement of near-single-cycle and multi-cycle THz pulses based on nonlinear optical excitation of coherent phonon-polaritons through impulsive stimulated Raman scattering in ferroelectric crystals, such as lithium tantalate (LT) and lithium niobate (LN), and generation of coherent THz pulses by optical rectification of the near-infrared pump pulse. These phase-coherent THz pulses with picosecond durations and well defined waveforms are attractive not only because the oscillation periods are suitable for time-resolved measurement of many dynamics in semiconductors, liquids, superconductors, and organic materials, but the frequency components can directly excite and efficiently drive intermolecular vibrational modes with fewer nonlinear optical processes such as higher order phase modulations, white-light continuum generation, cascaded processes [86, 68], or multi-photon absorption [59] that may lead to photorefractive damage. In particular, recently developed high-energy THz pulses [132, 133, 58, 52, 54] enabled the observation of various aspects of nonlinear optics and spectroscopy in the THz regime [62, 109], including self-phase modulation and harmonic generation [55], the dynamic Franz-Keldysh effect, the THz Kerr Effect in nonpolar liquids [60], impact ionization and carrier cooling [61], intrinsic lattice anharmonicity [69, 72], and THz-induced molecular alignment [39]. With the development of THz technologies and phase and amplitude shaping of THz pulses, explorations of nonlinear THz photon echo and multidimensional spectroscopy, coherent collective ionic motions associated with macroscopic structure, and complex lattice mode coupling dynamics will become increasingly accessible in the near future.

1.1 Elementary excitations and phonon-polaritons

Since the source of THz radiation and one of its spectroscopic applications is in a solid state medium [49], a brief overview of the material structure and elementary excitations [87] is presented here as an introduction. Solid state is one of the common states of matter on Earth, and its constituent atoms, molecules, or ions have a distinct spatially periodic pattern that forms a lattice in all three dimensions. Interactions between the closely-packed nuclei and the electron clouds bound around them result

in many distinct physical, thermal, electromagnetic, and optical properties, such as superconductivity, energy transfer, chemical reactions, ferroelectricity and structural rearrangements.

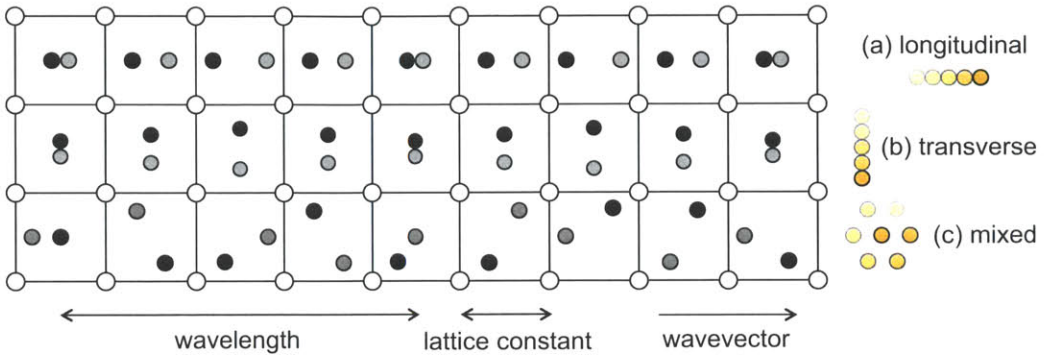

Figure 1-1: An illustration of a crystal lattice structure with translational symmetry. The collective vibrations of atoms and molecules around their equilibrium sites can be described as motions that follow many characteristic (a) longitudinal or (b) transverse normal modes that are internal degrees of freedom of the crystal. The lattice constants are usually a few Angstroms (or 10^{-10} m), and the phonon wavelengths can range from several lattice constants to much longer sizes, on the order of microns to 100 microns or 10^{-6} m to 10^{-4} m.

Vibrations of atoms around their equilibrium locations at small amplitudes can be well approximated as harmonic oscillations, and collective motions can be described by characteristic modes due to the translational symmetry and long range order of the lattice structure, as shown in Figure 1-1. The energy quantum, or quasi-particle, of this type of collective motion is a phonon. The phonon modes can be categorized as transverse or longitudinal, depending on the relationship between the direction of vibration and wave propagation, and acoustic or optical, depending on the change in the unit cell structure. Acoustic phonons are mechanical motions associated with longitudinal or shearing of the basic lattice element, while optical phonons are vibrations internal to unit cells that are sometimes accompanied by electromagnetic absorption and emission, along with mechanical motions. Crystal lattice constants are usually a few Angstroms or 10^{-10} m, and phonon wavelengths can be much longer, on the order of microns to 100 microns or 10^{-6} m to 10^{-4} m, in which case about 10^3 to 10^5 neighboring nuclei move in exactly the same way, synchronized in a phase-coherent manner.

In a polar or ionic crystal, oscillations in the form of optical phonons are intrinsically polarization waves or dipole oscillations that will generate new transverse electromagnetic waves along with their vibrational motions, which in turn will be strongly coupled with optical phonons with comparable frequency and wavevector components. Different electromagnetic frequency components can only propagate with speeds depending on the strength of interaction with the phonon modes, the later of which are determined by electronic and lattice properties. The energy quantum, or quasiparticle, of this type of cooperative motion is a phonon-polariton [21, 36, 12, 65], and it has both a vibrational phonon part as well as an electromagnetic photon part. The THz radiation that will be presented in this thesis is based on coherently excited phonon-polaritons in ferroelectric crystals.

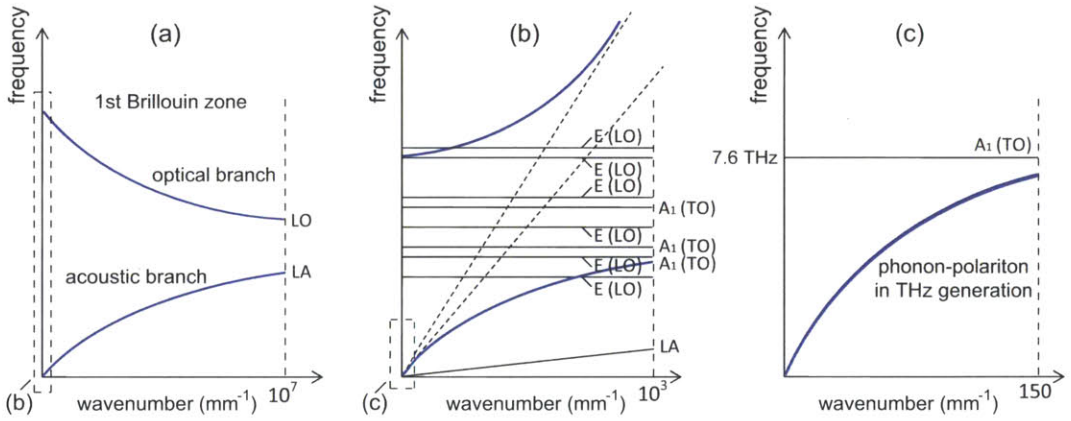

Figure 1-2: Qualitative illustration of (a) typical acoustic and optical phonon dispersions, (b) long wavelength phonon-polaritons near the center of the first Brillouin zone, and (c) the frequency and wavenumber components of the phonon-polaritons associated with the A_1 transverse optical phonons in THz generation in lithium niobate (whose lowest optic phonon frequency is 7.6 THz).

As shown in Figure 1-2, the frequency and wavenumber components of phonon-polaritons are near the center of the first Brillouin zone in the phonon dispersion diagram of a typical solid state polar crystal. The acoustic phonon modes and the majority of the longitudinal optical phonon modes do not interact with electromagnetic radiation. The phonon-polaritons in THz generation are associated with the lowest A_1 transverse optical phonon mode, with wavenumber components generally less than 100 cm^{-1}. The concave shape of the dispersion shows that higher frequency

electromagnetic radiation in this region correlates with stronger interaction with optical phonons.

Both acoustic and optical phonon modes, as well as phonon-polariton modes, are internal degrees of freedom of the crystal, which means that collective motions of nuclei can be described by combinations of these normal modes, independent of their external conditions or how they are excited. For example, with room temperature thermal energy at about 25.6 meV (which is 6.1 THz), phonon modes with eigenfrequencies at a few THz are already excited, randomly fluctuating, and statistically populated.

There are many other elementary excitations in solids, such as magnon-polaritons, the coupling of spin waves with electromagnetic fields, plasmons, electron oscillations around the lattice of ions, and excitons, bound states of electrons and holes. With combinations of materials, defects and doping, and engineered structures, these quasi-particles can exist in many varieties. Examples include the excitations of quantum wells and superlattices, carbon nanotubes and graphene, photonic and phononic crystals, and their surface versions, such as surface exciton-polaritons and surface plasmon-polaritons.

Excitations of electronic and lattice motions are studied in a variety of ways, including the spectroscopic methods in studying condensed matter that we will briefly introduce below.

1.2 The development of experimental methods

Light has been one of the important experimental methods over the course of scientific explorations. Even understanding what light is, in terms of its wave and particle nature, was not achieved until the beginning of the twentieth century. The classical spectral nature of light and the concept of spectroscopy, however, date back as early as Newton's sunlight dispersion and recombination experiment with a glass prism in 1665. The study of characteristic emission and absorption spectra from atoms such as hydrogen helped the establishment of the atomic structure, and efforts to

identify the origins of fine spectral intensity and position under various thermal and electromagnetic conditions contributed to our understanding of nuclear structure, particle spins, and quantum and statistical theory. Early atomic spectrum analyses were primarily around the visible region, but gradually extended into other parts of the spectrum along with the identification of invisible radiation, from ultraviolet, x-ray, and gamma ray frequencies on one end, to infrared, microwave, and radio frequencies on the other.

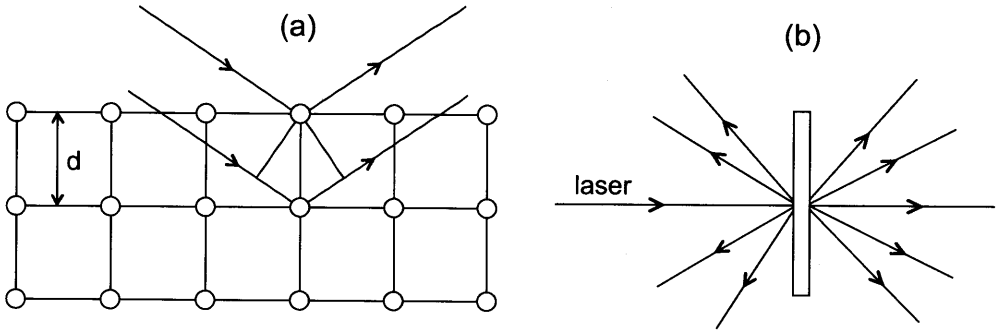

Figure 1-3: A qualitative illustration of (a) elastic light scattering with x-rays that can resolve the lattice structure at the atomic level, and (b) inelastic light scattering, such as Brillouin and Raman scattering, that can resolve the vibrational properties of matter. Note that the scattering angle can be as small as a few degrees in some cases.

The experimental study of condensed phase materials advanced with the development of light scattering techniques, including x-ray diffraction. The wavelengths of x-rays are typically on the order of Angstroms, or 10^{-10} m, which matches well with the structural features of lattices, as shown in Figure 1-3. This method allowed for atomic level research into chemical bonds, biological, and macromolecular structures, such as the nucleic acid DNA. Inelastic light scattering, such as Brillouin and Raman scattering, were discovered in the 1920s [15, 95], and have been the primary experimental methods to study the vibrational properties of matter.

The advent of maser and laser technologies revolutionized the world of spectroscopy. During the first several years after the invention, coherent radiation in the visible and infrared regions became available for coherent Brillouin and Raman scattering. A HeNe laser operating at 6328 Å was implemented in the Raman scat-

tering experiments of optical phonon modes in $LiNbO_3$ [6] and phonon-polaritons in GaP [57]. In the Raman scattering experiment of phonon-polaritons in ZnO [92] and electro-optic measurement in $LiNbO_3$ [70], the light source was an argon ion laser operating at 4880 Å. Just as the generation of the laser is itself a process of stimulated amplification, these scattering processes also have stimulated versions. In the experimental observation of stimulated Brillouin scattering [20, 44], the light source was an intense ruby laser operating at 6940 Å. Stimulated Raman scattering [32, 10] was also discovered through the radiation at 7670 Å while researching the operation of the ruby laser.

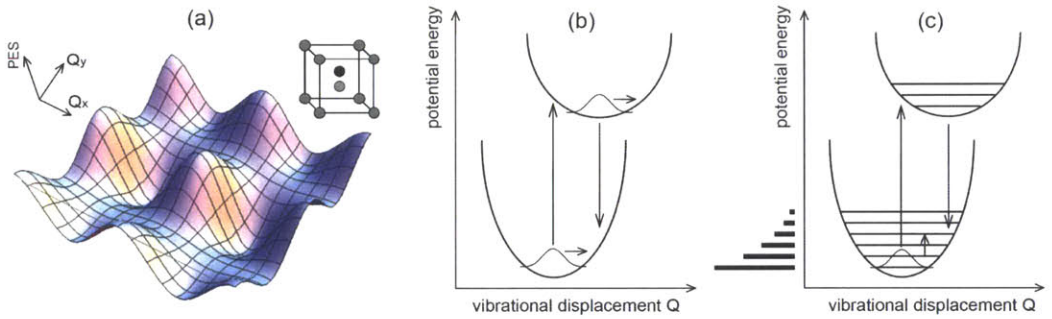

Figure 1-4: A qualitative illustration of (a) typical potential energy surface at the ground electronic state, (b) the classical picture of electronic energy levels and the initiation of coherent vibrations, (c) the quantum picture of electronic energy levels, the phonon-coupled electronic transition, and coherent vibrational modes in the harmonic potential energy surface.

In a typical crystalline material with translational symmetry, absorption and emission between electronic levels occur in the visible to ultraviolet region, and are usually accompanied by vibrational transitions that forms phonon sidebands in the spectrum. Experimentally, inelastic and stimulated light scattering techniques [50] and theories [65, 12, 103] have allowed the careful assignment of phonon [6, 98] and phonon-polariton modes [57, 21, 85], as well as the measurement of anisotropic polaritons [22], dielectric dispersions, and electro-optic coefficients [70].

The invention of the laser made possible numerous measurements of condensed phase materials with frequency-domain spectroscopy, and the development of pico- to femtosecond laser technologies [102] enabled ultrafast methods to reveal transient

phenomena and bring spectroscopy into the dynamic regime. The classical experimental method is the pump-probe technique, where a pump light pulse excites the sample and creates a coherent nonequilibrium state, followed by a variably delayed probe pulse that monitors the state relaxation that typically takes place on a very short time scale. In condensed phase materials, the collective resonances of electrons are close to the visible region, while the heavier nuclei have a longer characteristic time of collective motions on the picosecond scale. Upon irradiation of an intense laser pump in the visible region, the typical dynamics are that the electrons respond immediately and relax quickly, and the nuclei respond and relax relatively slower.

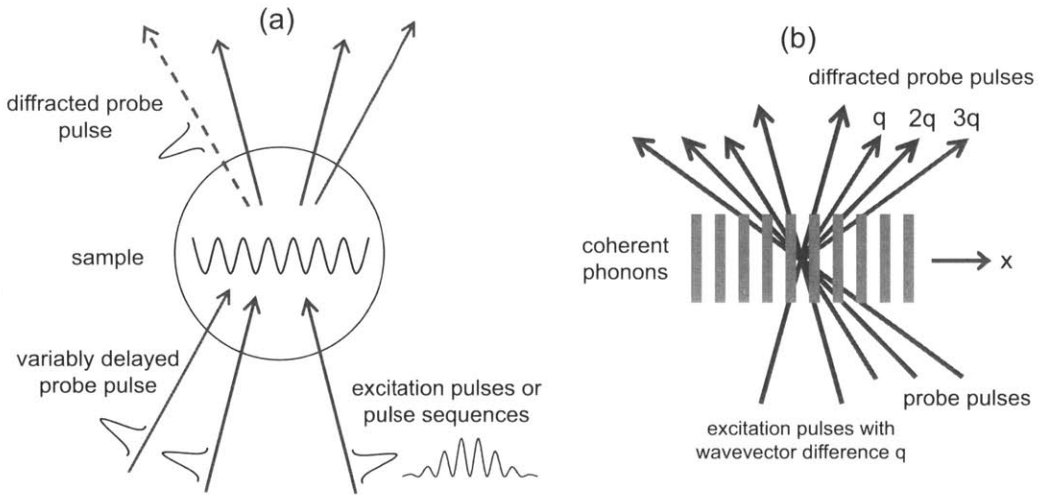

Figure 1-5: An illustration of (a) impulsive stimulated Raman scattering [126, 27] with temporally impulsive and spatially periodic excitation geometry (pulse sequences [117] can also be implemented to excite a selected frequency) and (b) wavevector overtone spectroscopy [14] with the same type of laser excitation geometry. Diffracted signals at wavevector overtones will appear with large coherent phonon vibrational motions.

The impulsive stimulated Raman and Brillouin scattering technique [126, 34] involves two excitation pulses crossed at the sample with a wavevector difference to create a transient grating pattern, as shown in Figure 1-5. This temporally impulsive, spatially periodic excitation can selectively excite coherent phonons at the wavevector difference, and the variably delayed probe pulse can be scattered at the phase-matching angle. The impulsive limit was realized with picosecond lasers for the excitation of acoustic phonons, and femtosecond lasers for the excitation of optical

phonons and phonon-polaritons, which means that the pulse duration is smaller than the oscillation period of the targeted phonons. In the classical picture, impulsive excitation exerts a sudden force on the nuclei in the potential surface of the ground electronic level. Many improvements were also made based on this method, namely impulsive stimulated thermal scattering, pulse sequence excitation [118, 119, 117] with pulse shaping techniques [73], the implementation of a phase mask to improve beam overlap [83], and wavevector overtone spectroscopy [14] to monitor large coherent vibrational motions.

1.3 Terahertz optics and spectroscopy

The Raman spectroscopy technique can be implemented to study vibrational modes and to launch coherent vibrations that are Raman active and associated with changes in polarizability. For many samples lacking a center of inversion symmetry, the optical phonon modes that are Raman active are also infrared (IR) active and associated with changes in dipole moment, so the system will have a strong response if directly excited by radiation in the THz region.

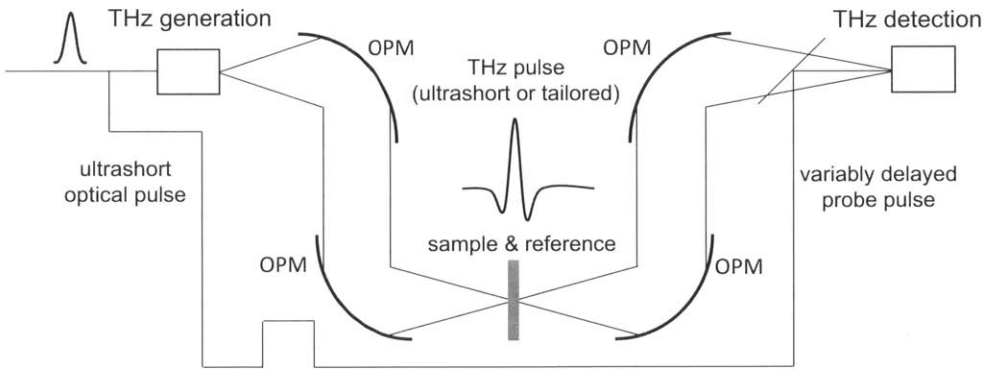

Figure 1-6: An illustration of THz time-domain spectroscopy. Based on optical generation with ultrashort laser pulses, THz radiation can be well-integrated into the spectroscopy experiment as the pump pulse, the probe pulse, or both. Time-resolved absorption spectroscopies can be conducted.

Phonon-polaritons in polar ionic and molecular crystals have been of considerable interest as a source of far-infrared electromagnetic waves given the mixed phonon-

photon character. Coherent generation with pico- and femtosecond optical pulses through stimulated Raman scattering in electro-optic $LiNbO_3$ and $LiTaO_3$ crystals were carefully studied and observed [130, 23, 28, 124]. An integrated polaritonic platform [36] was developed to observe and image the generation and control of phonon-polaritons that travel at light-like speed in the crystal, with optical pulses that are shaped temporally [116], spatially [23, 38, 73], and spatiotemporally [37]. Many integrated functional elements have also been demonstrated, such as waveguide and diffractive elements [36], with potential applications in THz signal processing.

THz time-domain spectroscopy [48, 100] was made possible with the development of coherent free-space THz radiation. This can be generated through photoconductive antennas [4, 35], electro-opic crystals [130, 9], air plasmas [33, 71], and free electron lasers [17]. As shown in Figure 1-6, based on optical generation with ultrashort laser pulses, THz radiation can be well integrated into the spectroscopy experiment as the pump pulse, the probe pulse, or both for absorption as well as time-resolved spectroscopy and measurements.

The generation of intense THz pulses based on the tilted intensity front [132, 52, 54, 58, 62, 55] technique has enabled many spectroscopy experiments [61, 109, 60, 39] in solids, liquids and gases at the high-field regime. Numerous investigations into collective electronic and nuclear dynamics remain to be explored.

This thesis is organized as follows: in Chapter 2, the theoretical background and simulations of phonon-polariton generation and control through impulsive stimulated Raman scattering with ultrashort laser pulses is introduced. Chapter 3 describes the experimental methods and general considerations. In Chapter 4, generation of high power single-cycle and tunable multi-cycle THz pulses are elaborated. Chapter 5 is the nonlinear phenomena observed in THz generation process where simulations as well as experimental results are presented.

Chapter 2

Generation, Control, and Enhancement of Phonon-polaritons

This work is in collaboration with Dr. Christopher A. Werley of the Massachusetts Institute of Technology.

The theoretical background of optical phonons [6] and phonon-polaritons [12, 21, 22] in polar ionic and molecular crystals, and their coherent excitation mechanism through stimulated Raman scattering [103, 16] as well as in the impulsive limit [126, 127, 128], have been extensively studied. These properties were experimentally confirmed by near-forward Raman scattering [57], stimulated Raman scattering with picosecond pulses [130], and femtosecond excitation in the impulsive limit [28, 124]. In this chapter, we briefly present the theoretical background and coherent excitation of phonon-polaritons in ferroelectric crystals $LiNbO_3$ and $LiTaO_3$ with standard Gaussian and shaped ultrashort optical pulses in the classical framework, with emphasis on how the THz waveform, and the frequency and wavevector components, are influenced by laser pulses in the generation process. Phonon-polaritons in a thin ferroelectric crystal and methods of amplitude enhancement by spatiotemporal focusing and optical waveform control are also introduced.

2.1 Phonon-polariton properties in ferroelectrics

The platform for generation of THz phonon-polaritons in this thesis is based primarily on uniaxial ferroelectric crystals $LiNbO_3$ and $LiTaO_3$, which have a ten-atom trigonal structure periodicity along all three dimensions. These crystals have an optic axis or the extraordinary axis, along which the Li, Nb, and Ta ions are positioned with slight asymmetry in the room temperature ferroelectric phase, and the crystal shows macroscopic spontaneous polarization. The Curie temperatures for $LiNbO_3$ and $LiTaO_3$ are approximately 1415 K and 883 K respectively, and the melting temperatures are approximately 1530K and 1923 K respectively. Both crystals have a wide transparency range that covers the entire visible and infrared spectrum, and both have large electro-optic coefficients, which is one of the major reasons for the application of THz generation with ultrashort optical laser pulses and appropriate phase matching techniques.

2.1.1 Phonon and phonon-polariton modes

The polar optical phonons in $LiNbO_3$ and $LiTaO_3$ have well-known ($4A_1 + 9E$) modes [70, 6] for both transverse (TO) and longitudinal (LO) optical phonons. Mode assignments, Raman scattering efficiencies, and contributions to electro-optic coefficients can be measured through Raman spectra. The A_1 symmetry modes correspond to the vibrations of Li and Nb ions along the optic axis, and the E symmetry modes correspond to the stretching of oxygens in the plane perpendicular to the optic axis, as shown in Figure 2-1. As an example, in the A_1 symmetry modes of $LiNbO_3$ [70], the transverse mode frequencies are [70] 7.6 THz, 8.3 THz, 10.0 THz, and 19.1 THz, and the longitudinal mode frequencies are 8.2 THz, 10.0 THz, 12.8 THz, and 26.2 THz.

Electromagnetic waves in the crystal can couple with different transverse and longitudinal optical phonon modes depending on the propagation direction k, and the angle between k and the optic axis z is denoted as θ in this thesis. When $\theta = 0°$ or $k \parallel z$, the A_1 symmetry mode is longitudinal and the E symmetry mode is transverse,

and in the case of $\theta = 90°$ or $k \perp z$, the E symmetry mode is longitudinal and the A_1 symmetry mode is transverse. In the general propagation direction when $0° < \theta < 90°$, the wave is a mixed TO+LO type. It has been demonstrated experimentally that the electro-optic effect is due primarily to the contributions from the lowest A_1 transverse optical phonon mode [70] resonant at 7.6 THz in $LiNbO_3$, and that it has the largest nonlinear r_{33} number. When the wave-vector k is perpendicular to the optic axis z, all the longitudinal lattice vibrations are without dispersion, and the strong coupling between the lowest transverse optical (TO) phonon mode and electromagnetic waves exist in the form of phonon-polaritons that can be coherently generated and provide a source for THz radiation. The coupling of electromagnetic waves with other transverse optical phonon modes is very weak and can usually be neglected, which will become clear in the classical harmonic oscillator model that is introduced in the following sections.

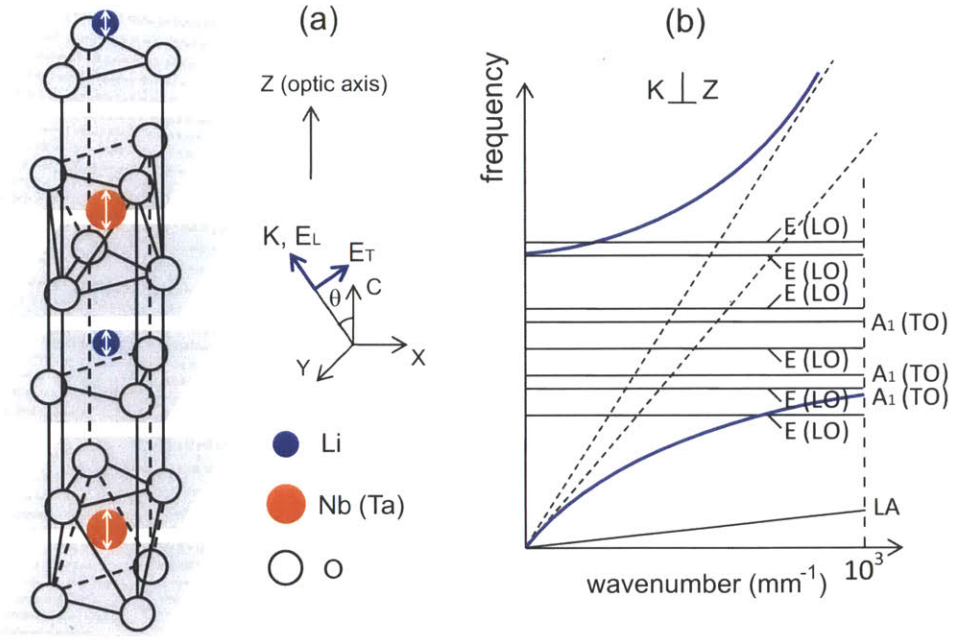

Figure 2-1: Illustration of (a) the uniaxial crystal structures of $LiNbO_3$ and $LiTaO_3$, and (b) the optical phonons and phonon-polariton dispersions when the wave vector is perpendicular to the optic axis. The longitudinal lattice vibrations (LO) are without dispersion, and there is strong interaction between the lowest A_1 transverse mode (TO) and the electromagnetic wave.

2.1.2 Classical model of phonon-polaritons

The classical model of phonon-polariton [65, 12] mainly contains the phonon part and photon part. The collective ionic motions in the form of phonons can be modeled as harmonic oscillators along the phonon normal mode coordinate $\vec{Q} = \sqrt{NM}\vec{\mathrm{w}}$, where M is the reduced mass of the unit cell, N is the oscillator density, and $\vec{\mathrm{w}}$ is the reduced mass displacement. Based on the dielectric polarization $\vec{P}$, macroscopic electric field $\vec{E}$, and b coefficients that are characteristic of the material and depend on the wave propagation direction relative to the optic axis of the uniaxial crystal,

$$b_{11} = -\omega_{\mathrm{TO}}^2 \tag{2.1}$$

$$b_{12} = b_{21} = \omega_{\mathrm{TO}}\sqrt{\epsilon_0(\varepsilon_0 - \varepsilon_\infty)} \tag{2.2}$$

$$b_{22} = \epsilon_0(\varepsilon_\infty - 1) \tag{2.3}$$

the phonon motion equations can be written as:

$$\ddot{\vec{Q}} = b_{11}\vec{Q} + b_{12}\vec{E} \tag{2.4}$$

$$\vec{P} = b_{21}\vec{Q} + b_{22}\vec{E} \tag{2.5}$$

To account for phonon-phonon interactions as well as other relaxation terms, a phenomenological damping term Γ is introduced, and the equation becomes:

$$\ddot{\vec{Q}} + \Gamma\dot{\vec{Q}} + \omega_{\mathrm{TO}}^2\vec{Q} = b_{12}\vec{E} \tag{2.6}$$

The photon component can be modeled by Maxwell's equations:

$$\nabla \times \vec{E} = -\frac{\partial \vec{B}}{\partial t} \tag{2.7}$$

$$\nabla \times \vec{H} = \frac{\partial \vec{D}}{\partial t} \tag{2.8}$$

$$\nabla \cdot \vec{B} = 0 \tag{2.9}$$

$$\nabla \cdot \vec{D} = 0 \tag{2.10}$$

which, when combined with vector and scalar potentials,

$$\vec{B} = \nabla \times \vec{A}, \quad \vec{E} = -\frac{\partial \vec{A}}{\partial t} - \nabla\phi \tag{2.11}$$

and polar phonon motions,

$$\vec{D} = \varepsilon_0 \vec{E} + \vec{P} = (\varepsilon_0 + b_{22})\vec{E} + b_{21}\vec{Q} \tag{2.12}$$

can lead to the coupled vector potential equation:

$$(\nabla^2 \vec{A} - \frac{1}{c_0^2/\varepsilon_\infty}\ddot{\vec{A}}) = -\mu_0 \omega_{\mathrm{TO}} \sqrt{\epsilon_0(\varepsilon_0 - \varepsilon_\infty)}\dot{\vec{Q}} \tag{2.13}$$

so the governing equations modeling the phonon-polaritons with both electromagnetic and vibrational dynamics are:

$$\begin{cases} \ddot{\vec{Q}} + \Gamma\dot{\vec{Q}} + \omega_{\mathrm{TO}}^2 \vec{Q} &= b_{12}\vec{E} \\ (\nabla^2 \vec{A} - \frac{1}{c_0^2/\varepsilon_\infty}\ddot{\vec{A}}) &= -\mu_0 \omega_{\mathrm{TO}} \sqrt{\epsilon_0(\varepsilon_0 - \varepsilon_\infty)}\dot{\vec{Q}} \end{cases} \tag{2.14}$$

2.1.3 Dielectric function and quantitative dispersion

With the constitutive relation $P(w) = \epsilon_0(\varepsilon_r(\omega) - 1)E(\omega)$, the dielectric function can be derived from equation (2.5), and the relative permittivity $\varepsilon_r(\omega)$ can be written as,

$$\varepsilon_r(\omega) = 1 + \frac{b_{22}}{\epsilon_0} + \frac{1}{\epsilon_0}\frac{b_{12}b_{21}}{\omega_{\mathrm{TO}}^2 - \omega^2 - i\omega\Gamma} \tag{2.15}$$

with the two off-resonance limits in the spectrum,

$$\varepsilon_\infty = 1 + \frac{b_{22}}{\epsilon_0}, \quad \varepsilon_0 = \varepsilon_\infty + \frac{b_{12}b_{21}}{\epsilon_0 \omega_{\mathrm{TO}}^2} \tag{2.16}$$

the dielectric function is

$$\varepsilon_r(\omega) = \varepsilon_\infty + \frac{\omega_{\mathrm{TO}}^2(\varepsilon_0 - \varepsilon_\infty)}{\omega_{\mathrm{TO}}^2 - \omega^2 - i\omega\Gamma} \tag{2.17}$$

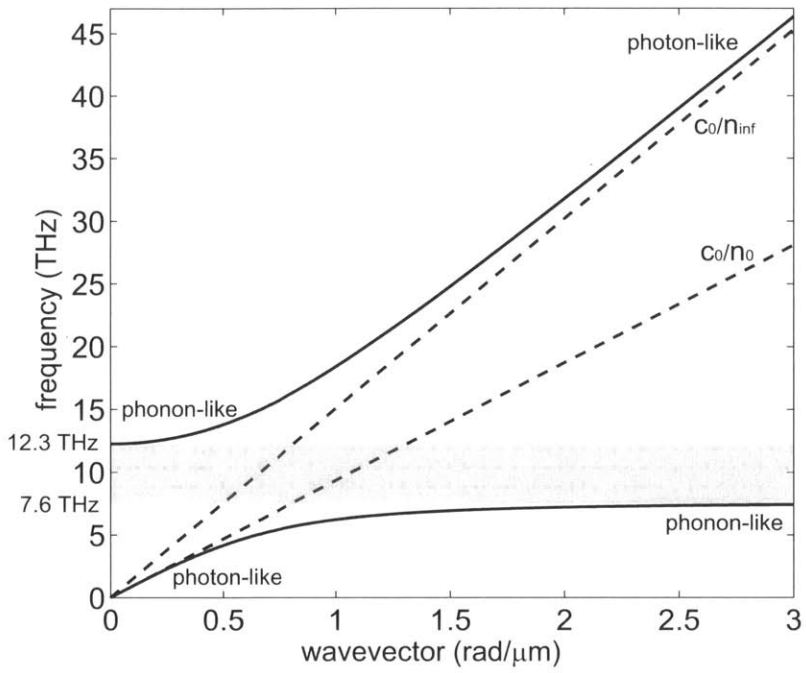

Figure 2-2: Calculated dispersion relation of phonon-polaritons in $LiNbO_3$ at room temperature where the lowest transverse optic phonon mode at 7.6 THz is taken into account.

and the dispersion relations are as follows,

$$\omega(k) = \sqrt{\frac{\omega_{\mathrm{TO}}^2\varepsilon_0 + c^2k^2}{2\varepsilon_\infty} \pm \frac{1}{2}\sqrt{(\frac{\omega_{\mathrm{TO}}^2\varepsilon_0 + c^2k^2}{\varepsilon_\infty})^2 - \frac{4\omega_{\mathrm{TO}}^2c^2k^2}{\varepsilon_\infty}}} \tag{2.18}$$

where the the positive and negative roots correspond to the upper and lower branches respectively, as shown in Figure 2-2.

The real and imaginary parts of the dielectric function and THz indices are shown in Figure 2-3. The real part of THz index corresponds to the phase velocity of the phonon-polariton wave at a specific frequency, and the imaginary part corresponds to the absorption due to the phonon resonance that couples with the electromagnetic wave in the phonon-polariton mode.

The dispersion relations are intrinsic properties of matter, and can be characterized by three parameters: the resonance frequency of the lowest transverse optic phonon mode ω_{TO}, and the dielectric constants in the low and high frequency limits ε_0 and ε_∞. The ω_{LO} in the dispersion diagram can be calculated by $\omega_{\mathrm{LO}} = \omega_{\mathrm{TO}}\sqrt{\varepsilon_0/\varepsilon_\infty}$.

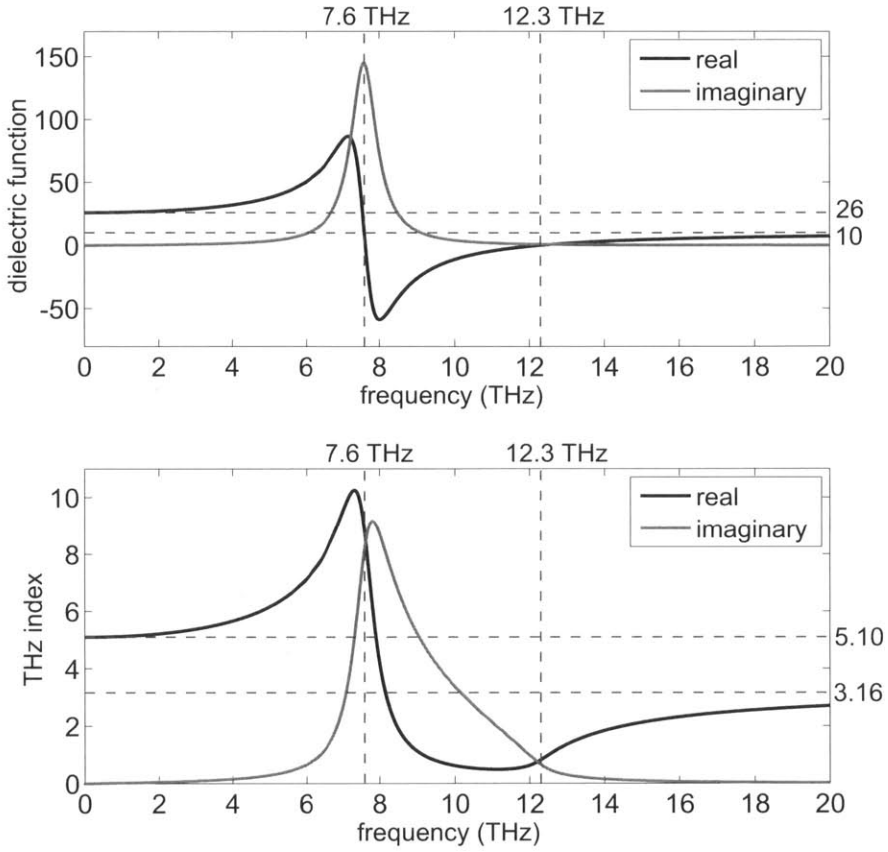

Figure 2-3: Calculated dielectric function and complex index of phonon-polaritons in $LiNbO_3$ at room temperature where the lowest transverse optic phonon mode at 7.6 THz is taken into account.

2.1.4 Anisotropic phonon-polaritons

It can be concluded that the derivations of these equations are in three dimensions, and the difference is set by the direction relative to the optic axis. This is a material-intrinsic property, and can be implemented through the direction-dependent physical constants. In uniaxial crystals, the characteristic dielectric tensors are $\epsilon_{xx}(\omega) = \epsilon_{yy}(\omega) = \epsilon_{\perp}(\omega)$ and $\epsilon_{zz}(\omega) = \epsilon_{\parallel}(\omega)$, where the $\perp$ and $\parallel$ represent whether the electric field in the polarization wave is perpendicular or parallel to the optic axis of the crystal. The dielectric function can be written as:

$$\varepsilon_{\parallel}(\omega) = \varepsilon_{\infty\parallel} + \frac{\omega_{\mathrm{TO}\parallel}^2(\varepsilon_{0\parallel} - \varepsilon_{\infty\parallel})}{\omega_{\mathrm{TO}\parallel}^2 - \omega^2 - i\omega\Gamma_{\parallel}} \tag{2.19}$$

$$\varepsilon_{\perp}(\omega) = \varepsilon_{\infty\perp} + \frac{\omega_{\mathrm{TO}\perp}^2(\varepsilon_{0\perp} - \varepsilon_{\infty\perp})}{\omega_{\mathrm{TO}\perp}^2 - \omega^2 - i\omega\Gamma_{\perp}} \tag{2.20}$$

which, when combined with the phonon-polariton motion equation, leads to the directional dispersion relation in the general case ($0 < \theta < 90°$) [85],

$$\varepsilon(\omega,\theta) = \frac{c^2k^2}{\omega^2} = \frac{\varepsilon_{\perp}(\omega)\varepsilon_{\parallel}(\omega)}{\varepsilon_{\perp}(\omega)\sin^2\theta + \varepsilon_{\parallel}(\omega)\cos^2\theta} \tag{2.21}$$

where θ denotes the angle between the electric field and the optic axis.

The direction-dependent versions of the phonon-polartion equations can therefore be written as:

$$\ddot{\vec{Q}}_{x,y} + \Gamma_{\perp}\dot{\vec{Q}}_{x,y} + \omega_{\mathrm{TO}\perp}^2\vec{Q}_{x,y} = \omega_{\mathrm{TO}\perp}\sqrt{\epsilon_0(\varepsilon_{0\perp} - \varepsilon_{\infty\perp})}\vec{E}_{x,y} \tag{2.22}$$

$$\ddot{\vec{Q}}_{z} + \Gamma_{\parallel}\dot{\vec{Q}}_{z} + \omega_{\mathrm{TO}\parallel}^2\vec{Q}_{z} = \omega_{\mathrm{TO}\parallel}\sqrt{\epsilon_0(\varepsilon_{0\parallel} - \varepsilon_{\infty\parallel})}\vec{E}_{z} \tag{2.23}$$

$$(\nabla^2\vec{A}_{x,y} - \frac{1}{c_0^2/\varepsilon_{\infty\perp}}\ddot{\vec{A}}_{x,y}) = -\mu_0\omega_{\mathrm{TO}\perp}\sqrt{\epsilon_0(\varepsilon_{0\perp} - \varepsilon_{\infty\perp})}\dot{\vec{Q}}_{x,y} \tag{2.24}$$

$$(\nabla^2\vec{A}_{z} - \frac{1}{c_0^2/\varepsilon_{\infty\parallel}}\ddot{\vec{A}}_{z}) = -\mu_0\omega_{\mathrm{TO}\parallel}\sqrt{\epsilon_0(\varepsilon_{0\parallel} - \varepsilon_{\infty\parallel})}\dot{\vec{Q}}_{z} \tag{2.25}$$

In $LiNbO_3$, these constants [6, 36] are summarized in the following table,

	$\omega_T/2\pi$ (THz)	$\Gamma/2\pi$ (THz)	ε_0	ε_∞
$\vec{k}\perp z, \theta = 90°$	$\omega_{T\parallel}/2\pi = 7.6$	$\Gamma_{\parallel}/2\pi = 0.63$	$\varepsilon_{0\parallel} = 26.0$	$\varepsilon_{\infty\parallel} = 10.0$
$\vec{k}\parallel z, \theta = 0°$	$\omega_{T\perp}/2\pi = 4.6$	$\Gamma_{\parallel}/2\pi = 0.42$	$\varepsilon_{0\perp} = 41.5$	$\varepsilon_{\infty\perp} = 19.5$

Table 2.1: Direction-dependent physical constants in $LiNbO_3$ at room temperature.

2.1.5 Phase and amplitude configuration

Assuming the solutions of the phonon-polariton motion equations can be written as the frequency-dependent form, $\vec{Q} = \vec{Q}_0 e^{i(kx-\omega t)}$, $\vec{E} = \vec{E}_0 e^{i(kx-\omega t-\phi)}$, since the electric (magnetic) field and lattice displacement oscillate with the same frequency and

wavevector but not exactly the same phase. Some of the following derivation can be found in [13]. In this section, the phase difference ϕ and damping are taken into account to characterize the near resonance feature and energy distribution. Equation (2.6) can be rewritten as:

$$\frac{E_0 e^{i\phi}}{Q_0} = \frac{\omega_{\mathrm{TO}}^2 - \omega^2 + i\omega\Gamma}{\omega_{\mathrm{TO}}\sqrt{\epsilon_0(\varepsilon_0 - \varepsilon_\infty)}} \tag{2.26}$$

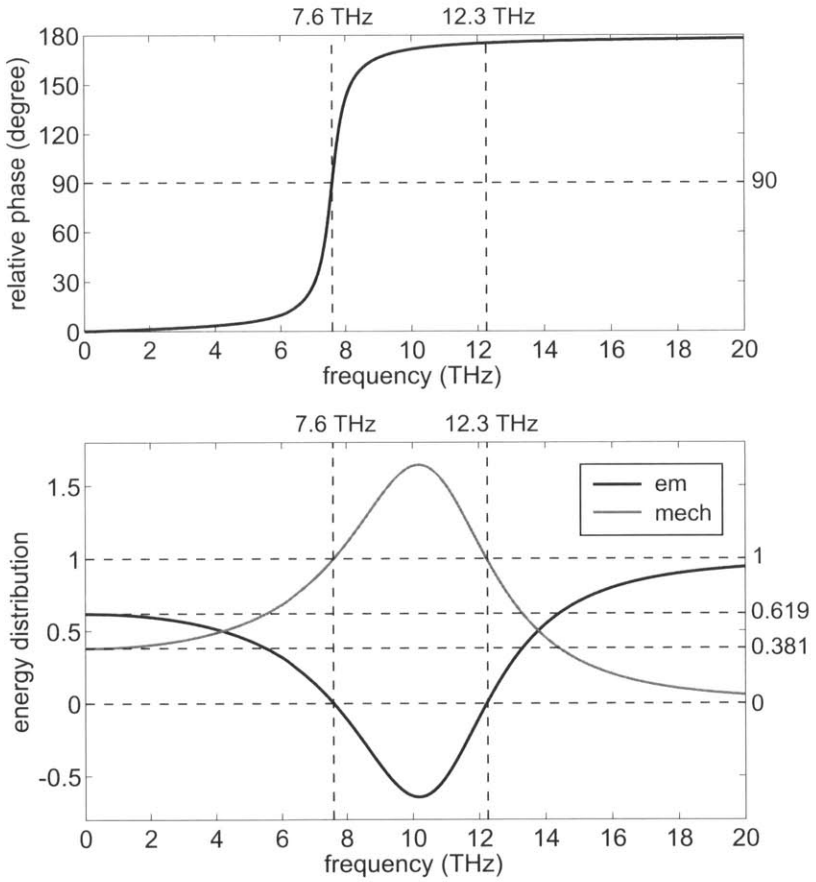

Figure 2-4: Relative phase and energy distributions between the electromagnetic photon part and the mechanical phonon part of the phonon-polaritons in $LiNbO_3$ with the lowest A_1 transverse optical phonon mode taken into account. There should be no mode in the polariton gap region between 7.6 THz and 12.3 THz.

The relative magnitude and phase between the electric field and lattice displace-

ment can be derived as

$$\left|\frac{E_0}{Q_0}\right| = \left(\frac{(\omega_{\mathrm{TO}}^2-\omega^2)^2+(\omega\Gamma)^2}{\omega_{\mathrm{TO}}^2\epsilon_0(\varepsilon_0-\varepsilon_\infty)}\right)^{\frac{1}{2}} \tag{2.27}$$

$$\phi = \arctan\frac{\omega\Gamma}{\omega_{\mathrm{TO}}^2-\omega^2} \tag{2.28}$$

The total energy of the phonon-polariton system can be written [65] as the sum of the electromagnetic photon part and the mechanical phonon part $U_{tot} = U_{mech} + U_{em}$, where U_{mech} and U_{em} are energies per unit volume or energy densities,

$$\begin{aligned}
\mathrm{U}_{em} &= \vec{D}\cdot\vec{E} = (b_{21}\vec{Q}+b_{22}\vec{E}+\epsilon_0\vec{E})\cdot\vec{E} \\
&= b_{21}|Q_0||E_0|\cos\phi + \epsilon_0\varepsilon_\infty|E_0|^2 \qquad (2.29)\\
&= Q_0^2\Bigg(b_{21}\cdot\frac{\sqrt{(\omega_{\mathrm{TO}}^2-\omega^2)^2+(\omega\Gamma)^2}}{b_{21}}\cdot\frac{(\omega_{\mathrm{TO}}^2-\omega^2)}{\sqrt{(\omega_{\mathrm{TO}}^2-\omega^2)^2+(\omega\Gamma)^2}} \\
&\quad + \epsilon_0\varepsilon_\infty\cdot\frac{(\omega_{\mathrm{TO}}^2-\omega^2)^2+(\omega\Gamma)^2}{\omega_{\mathrm{TO}}^2\epsilon_0(\varepsilon_0-\varepsilon_\infty)}\Bigg) \\
&= Q_0^2\left((\omega_{\mathrm{TO}}^2-\omega^2) + \varepsilon_\infty\cdot\frac{(\omega_{\mathrm{TO}}^2-\omega^2)^2+(\omega\Gamma)^2}{\omega_{\mathrm{TO}}^2(\varepsilon_0-\varepsilon_\infty)}\right) \qquad (2.30)
\end{aligned}$$

$$U_{mech} = \omega_{\mathrm{TO}}^2 Q_0^2 \tag{2.31}$$

where the electric energy density is equal to the magnetic energy density, so the total electromagnetic energy density is $\vec{D}\cdot\vec{E}$. Note that the electric field is the macroscopic field. The phase difference ϕ between E and Q is taken into account in their scalar product (2.29), and its frequency dependence is shown in Figure 2-4.

The ratio of the electromagnetic energy to total energy as a function of frequency can therefore be calculated as,

$$r_{em} = \frac{U_{em}}{U_{em}+U_{mech}}, \quad r_{mech} = \frac{U_{mech}}{U_{em}+U_{mech}} \tag{2.32}$$

where the damping effect is taken into account to characterize the near resonance region. At the resonance frequencies of 7.6 THz and 12.3 THz, the energies are

entirely in the mechanical phonon oscillations, and there should be no electromagnetic propagation in the polariton gap region between the resonance frequencies. In the frequencies of phonon-polaritons related to THz generation typically below 4 THz, the energy distribution between the electromagnetic and mechanical part is approximately 3:2, and the relative phase between the electric field and the lattice displacement is very small such that they are nearly in phase with each other.

2.2 Generation and control of phonon-polaritons with ultrashort lasers

The coherent excitation of phonon-polaritons in polar crystals with ultrashort laser pulses has been an area of considerable interest because of the potential for coupling the electromagnetic part into free space as a source of infrared radiation. This sections includes the general background of phonon-polariton excitation in ferroelectric crystals $LiNbO_3$ and $LiTaO_3$ through impulsive stimulated Raman scattering (ISRS) [126] with ultrashort pulses, phase matching considerations, and the control of frequency and wavevector contents by the optical spatiotemporal intensity profile.

2.2.1 Impulsive stimulated Raman scattering

The excitations of coherent phonons and phonon-polaritons were made possible by ultrashort laser pulses (with durations generally less than 100 fs) which, in the classical picture, corresponds to the sudden driving of the lattice along normal mode coordinates because the pulse duration is shorter than the oscillation period of typical optical phonon modes. Intense optical lasers can induce transient microscopic dynamics of both electrons and nuclei that contribute to the electro-optic process, and it usually comes with two types of interactions [70]: 1) change in the electronic polarizability with the applied field in the absence of lattice displacements, and 2) the excitation of lattice vibrations through stimulated Raman scattering that can induce a change in the refractive index. These driving forces can be introduced in

the phonon-polariton equation system as follows,

$$\begin{cases} \ddot{\vec{Q}} + \Gamma\dot{\vec{Q}} + \omega_{\mathrm{TO}}^2\vec{Q} &= b_{12}\vec{E} + F_{ISRS} \\ (\nabla^2\vec{A} - \frac{1}{c_0^2/\varepsilon_\infty}\ddot{\vec{A}}) &= -\mu_0\omega_{\mathrm{TO}}\sqrt{\epsilon_0(\varepsilon_0 - \varepsilon_\infty)}\dot{\vec{Q}} + F' \end{cases} \tag{2.33}$$

where F' is due to the direct electronic nonlinearity, and F_{ISRS} is the driving force on the phonon system during the stimulated Raman scattering process.

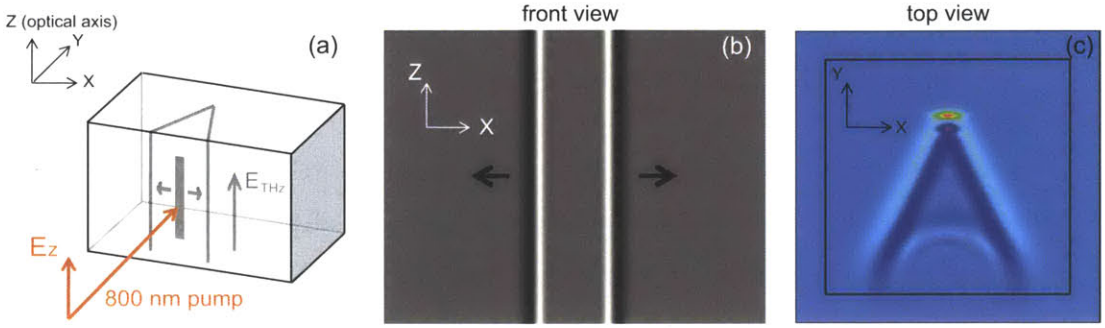

Figure 2-5: An illustration of non-resonant excitation of coherent phonon-polaritons in $LiNbO_3$ with a cylindrically focused laser pulse centered at 800 nm. (a) The polarizations of both the optical pulse and the phonon-polariton wave are along the optic axis of the crystal. (b) THz waves propagate laterally from the region that is irradiated by a cylindrically focused laser pulse. (c) THz waves propagate noncollinearly since the phase velocity of the THz wave is smaller than the group velocity of the optical pulse.

Many factors can contribute to the electro-optic process, including the scattering cross-section and polarizability, and the electronic and lattice contributions can vary by material. For ferroelectric crystals $LiNbO_3$ and $LiTaO_3$, the electro-optic effect is primarily due to the coupling with the lowest A_1 optical phonon mode with about 10% direct electronic contribution [70, 28]. The ISRS driving term [127, ?] with laser polarization parallel to the optic axis can be introduced into the phonon-polariton equations as follows

$$\begin{cases} \ddot{\vec{Q}} + \Gamma\dot{\vec{Q}} + \omega_{\mathrm{TO}}^2\vec{Q} &= b_{12}\vec{E} + \frac{1}{2}\epsilon_0\sqrt{\frac{N}{M}}(\frac{\partial\alpha}{\partial\vec{w}})I_{pump}(x,z,t) \\ (\nabla^2\vec{A} - \frac{1}{c_0^2/\varepsilon_\infty}\ddot{\vec{A}}) &= -\mu_0\omega_{\mathrm{TO}}\sqrt{\epsilon_0(\varepsilon_0 - \varepsilon_\infty)}\dot{\vec{Q}} \end{cases} \tag{2.34}$$

where the constants for $LiNbO_3$ are $N = 6.285 \times 10^{27}\ m^{-3}$, $M = 11.4\ amu$, $(\frac{\partial\alpha}{\partial\vec{w}})_{33} =$

$1.14 \times 10^{-18} m^2$, and the I_{pump} is the spatiotemporal intensity profile of the laser. The phonon-polariton equations are in three dimensions, and the laser polarization is usually along one of them.

Assuming the beam is propagating along the y axis as shown in Figure 2-5, the optical pump intensity can be written as,

$$I_{pump}(x,y,z,t) = I_0 e^{-(\frac{x-x_0}{\sigma_x})^2-(\frac{z-z_0}{\sigma_z})^2-(\frac{t-(y-y_0)\times n_{opt}/c}{\sigma_t})^2} \tag{2.35}$$

where σ_x, σ_z and σ_t can be expressed with experimental parameters,

$$\sigma_x = \frac{\text{spotsize}_x}{2\sqrt{\ln 2}} \tag{2.36}$$

$$\sigma_z = \frac{\text{spotsize}_z}{2\sqrt{\ln 2}} \tag{2.37}$$

$$\sigma_t = \frac{\text{duration}}{2\sqrt{\ln 2}} \tag{2.38}$$

where the spot size and duration are the full-width at half-maximum (FWHM) of the Gaussian intensity envelope.

With typical ultrashort laser pulse excitation in bulk uniaxial ferroelectric crystal $LiNbO_3$, the generation process and THz electric field pattern is illustrated in Figure 2-5. The polarization of both the optical pulse and the generated phonon-polariton waves are along the optic axis of the crystal, which is the Z axis in the figure. The phonon-polariton wave in the Z-X plane is similar to classical dipole radiation that propagates primarily in the lateral direction, which can be clearly seen with a cylindrically focused laser pulse. Note that this plane is anisotropic, so the wave propagates faster in the lateral direction with approximately 20% anisotropy in $LiNbO_3$. In the Y-X plane, the THz wave propagates noncollinearly with the laser since the phase velocity of the THz wave is smaller than the group velocity of the optical pulse. Phase-matching conditions and applications in THz generation are presented in the next section.

2.2.2 Phase-matching considerations

During the electro-optic generation process with ultrashort laser pulses, one of the critical factors is phase-matched amplification, which is traditionally achieved through collinear velocity matching geometry. When the peak of the optical intensity travels through the sample at a speed matching that of the THz phase velocity, the newly generated THz waves can add up coherently, and form an amplitude-enhanced near-single-cycle THz wave, as shown in Figure 2-6. Experimentally, collinear geometry can be achieved with 800 nm pump pulses in ZnTe [9], and 1035 nm pump pulses in GaP [59].

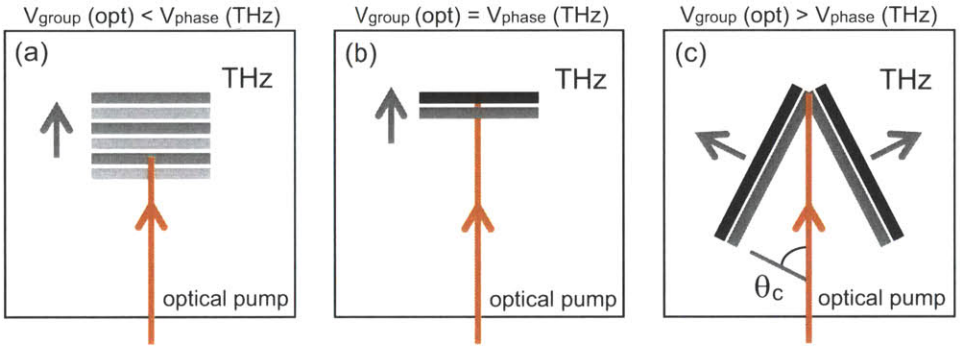

Figure 2-6: An illustration of generation of THz waves and phase-matching conditions in electro-optic materials where (a) the optical group velocity is smaller than the THz phase velocity, (b) the optical group velocity equals the THz phase velocity and the THz wave can be continuously amplified in a phase-matched manner, and (c) the optical group velocity is larger than the THz phase velocity, where the Cherenkov angle can be calculated as $\theta_c = \cos^{-1}(\nu_{\mathrm{THz}}^{\mathrm{ph}}/\nu_{\mathrm{vis}}^{\mathrm{gr}})$.

If the optical group velocity is smaller than the THz phase velocity, the newly generated THz wave will lag behind the previously generated single-cycle THz wave as well as the entire THz wave envelope. As the phase cycles keep growing into the trailing edge, a multicycle THz wave can be formed with increasing propagation distance. If the optical group velocity is larger than the THz phase velocity, the THz wave does not have phase-matched amplification, and instead forms the noncollinear radiation pattern while still taking on a single-cycle shape, primarily in the lateral direction. The Cherenkov angle can be calculated as $\theta_c = \cos^{-1}(\nu_{\mathrm{THz}}^{\mathrm{ph}}/\nu_{\mathrm{vis}}^{\mathrm{gr}})$, and it can become very large in some dielectric crystals with a high THz index. For example

in $LiNbO_3$, the optical group index at 800 nm is 2.25, and the THz index is 4.96, yielding a Cherenkov angle of 63°.

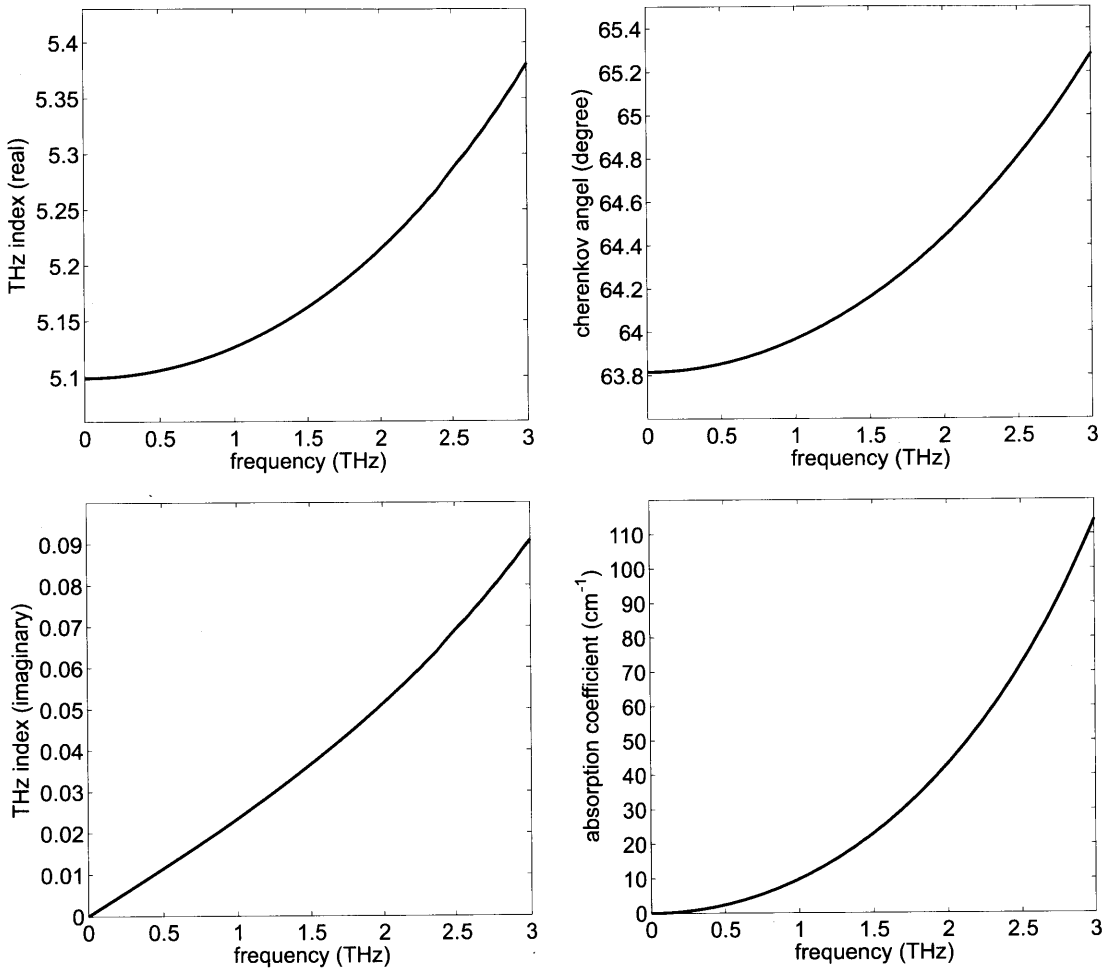

Figure 2-7: Calculated real and imaginary parts of the THz index in $LiNbO_3$ and the absorption coefficients. The experimental values, especially the absorption, can be somewhat different due to the influence of other phonon modes, free carrier absorption, material doping level and temperature.

The real and imaginary parts of the THz index and the absorption coefficients in $LiNbO_3$ are shown in Figure 2-7. This calculation takes into account the phonon resonance at 7.6 THz that determines the general trend of these parameters. The experimental values, especially the absorption, can be different due the influence of other phonon modes [70], free carrier absorption [59], material doping levels and temperature [88].

2.2.3 Spatiotemporal waveform control

Given the excitation with a transform-limited optical pulse, coherent control of the THz waveform, frequency, and wavevector components can be achieved through the spatiotemporal shaping of optical pulses, much like the engineering of complex waveforms in a fully coherent multidimensional manner, including the phase, amplitude, and wavevector [38, 112, 113]. Since the wavelength of the THz wave is much longer than that of the optical pulse, the specified THz far-field responses can be made through continuous and discrete optical pulse shaping in both the spatial and temporal domains [37].

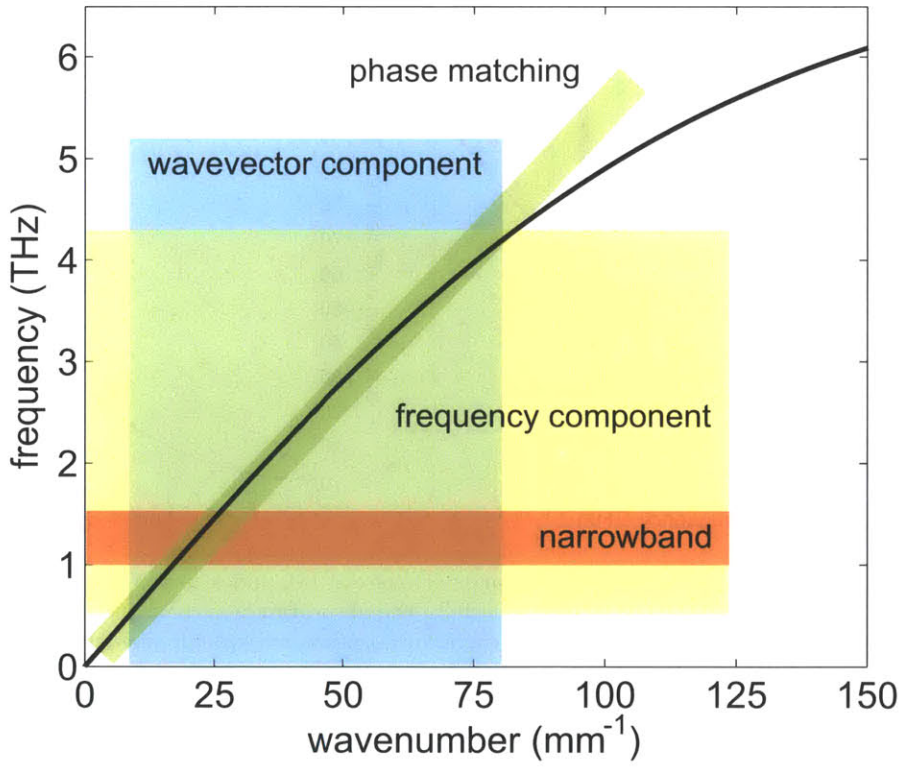

Figure 2-8: The phonon-polariton wavevector and frequency components are determined by the intersection of the corresponding wavevector and frequency regions tuned by the spatial and temporal intensity profile of the excitation laser. Further selection of a relatively narrow region of frequencies, wavevectors, or phase velocities can give rise to the generation of multicycle THz pulses.

The frequency and wavevector components of phonon-polaritons need to fit on the material dispersion diagram, and coherent generation through impulsive stimulated

Raman scattering usually covers part of the region, giving rise to the THz waveform. In the time domain, the Raman and Stokes frequency pairs are contained within the broad optical bandwidth of the laser spectrum, yielding different excitation efficiencies for different frequency components. The frequency content is inversely proportional to the duration of the pump pulse intensity envelope. In the spatial domain, the observed THz waveform resembles the spatial derivative [38] of the excitation beam intensity $I_{pump}(x)$:

$$E_{THz}(x \pm \frac{ct}{n}, t) \propto \partial_x I_{pump}(x) \tag{2.39}$$

and the wavevector components are determined by the spatial optical intensity profile which is also usually Gaussian. The THz waveform is therefore jointly controlled by these two dimensions and determined by the intersection of the tuning region, as shown in Figure 2-8.

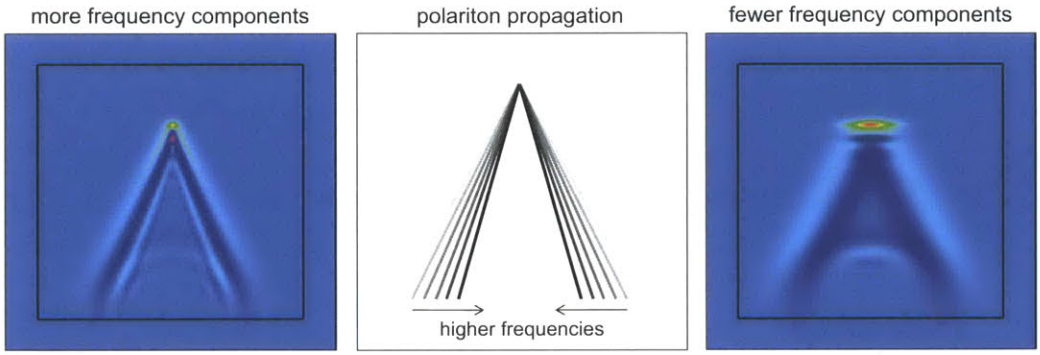

Figure 2-9: The frequency-dependent THz phonon-polariton propagation due to a small amount of group velocity dispersion. Lower frequency components have smaller THz index therefore propagate faster than higher frequency components.

For temporally impulsive femtosecond pulses, the frequency tuning capability can reach up to 10 THz, so the THz generation and its waveform are primarily determined by the spot size of the laser pulse, which can be focused down to the order of 50 μm, corresponding to the phonon-polariton center frequency of approximately 0.5 THz. Tighter focus can generate more higher frequency components which may have slightly different phase velocities and higher damping rates. The general form of the phonon-polariton center frequency [115] can be derived from a simple model of ordered plane

of dipoles:

$$f_{max} = \frac{c_0\sqrt{2\ln 2}}{\sqrt{\epsilon_0}\pi\sigma_x} = \frac{22\ \text{THz}\cdot\mu m}{\sigma_x} \tag{2.40}$$

The velocity-matching condition can be drawn as a line through the origin with its slope set as the optical group velocity. In the collinear velocity matching geometry, a broadband or near-single-cycle THz pulse can be generated with a wide range of frequency components whose phase velocities match the optical group velocity. The dispersion diagram can be modified with different material structures, such as a dielectric waveguide or a photonic crystal. Noncollinear velocity matching is also possible through spatially and temporally displaced optical pulses, or via a tilted intensity front to allow for continuous amplification in high-index ferroelectric materials. Pulse shaping by selecting a relatively narrow region of frequencies, wavevectors, or phase velocities can give rise to the generation of multicycle THz pulses. These techniques will be further explored in subsequent chapters.

2.3 Phonon-polariton properties in a slab ferroelectric waveguide

In a bulk electro-optic crystal, the characteristic field pattern generated by ultrashort laser pulses in the plane perpendicular to the crystal optic axis is usually a single-cycle THz wave in the case of velocity matching or a noncollinearly propagating wave if the optical group velocity is larger than the THz phase velocity. When the THz wave is spatially confined in one dimension within a thickness comparable to that of the THz wavelength, approximately 50 μm to 100 μm, the crystal transitions from bulk mode into the dielectric waveguide regime where the THz waves need to fit characteristic waveguide modes that are closely associated with the dimension of spatial confinement. The $LiNbO_3$ and $LiTaO_3$ waveguides have been an important platform for the observation of coherent lattice dynamics, including THz phonon-polariton generation, propagation, and coherent control through spatiotemporal shaping of optical

pulses [36, 37]. THz propagation can be measured quantitatively as real-space images with various probe pulse delays that can be viewed as movies[121]. Many classical wave-like properties such as diffraction, transmission and focusing can be directly visualized. In this section, dielectric waveguide multi-mode behavior, simulations of generation of THz waves with spatiotemporal shaping of optical pulses, and methods of THz wave amplitude enhancement are presented.

2.3.1 Multi-mode and dispersion diagram

The dielectric waveguide structure is formed by the dielectric core, $LiNbO_3$ or $LiTaO_3$, and the cladding material, air, in the THz polaritonic platform. While there are many different configurations, in the THz generation experiment spatial confinement is usually in the isotropic plane that is perpendicular to the optic axis. Since the polarizations of both the optical excitation pulse and the THz wave are along the optic axis Z, this configuration is a transverse electric dielectric waveguide, and the electric fields and their first derivatives are continuous across the boundary of $LiNbO_3$ and air. Solving the electromagnetic equations and boundary conditions can give rise to the normal mode field distribution patterns

$$E_z(y) = \begin{cases} E_0 \cos k_y y, & |y| < d/2, \text{ symmetric mode;} \\ E_0 \cos\left(k_y y - \frac{\pi}{2}\right), & |y| < d/2, \text{ antisymmetric mode;} \\ E_0 e^{\pm \gamma_y y}, & |y| > d/2. \end{cases} \tag{2.41}$$

where d is the waveguide thickness, and k_y and γ_y are real positive numbers that determine the harmonic behavior in the dielectric core and the decay rate of the evanescent field into the far field respectively. Qualitative illustrations of the field patterns for the first few modes in $LiNbO_3$ are shown in Figure 2-10.

The calculated dispersion diagrams of the first few modes in $LiNbO_3$ waveguides with different thicknesses, 10 μm, 30 μm, 50 μm, and 100 μm, are shown in Figure 2-11. All modes have cutoff frequencies except the first one that can cover frequency components until the DC limit, and all cutoff frequency points are on the line of the

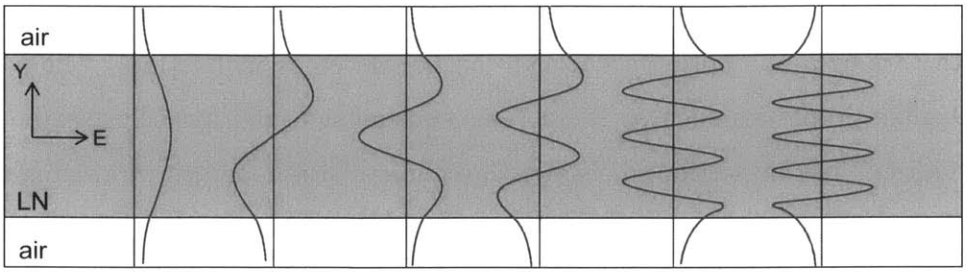

Figure 2-10: An illustration of the electric field distribution patterns for the first few modes in a $LiNbO_3$ waveguide. The field has harmonic behavior in the dielectric core, and an evanescent wave in the cladding air, which decays exponentially into the far field. There are symmetric and antisymmetric modes of the electric field, and the N_{th} mode has $N-1$ nodes along the dimension of spatial confinement.

speed of light in vacuum. As the thickness of the waveguide increases, these modes gradually move toward the bulk dispersion curve, and the gaps between them decrease until the bulk regime is reached.

2.3.2 Coherent excitation and evolution dynamics

Coherent THz waves in $LiNbO_3$ waveguides can be excited with ultrashort laser pulses in a manner similar to the bulk case. For an optical pump pulse with a temporal duration of about 100 fs or a spatial duration of about 15 μm in the crystal, the THz waves should initially show bulk-like behavior in a waveguide with the thickness larger than the optical spatial and temporal durations. The generated THz waves go through total internal reflections at the boundaries, and the interference between the waves propagating forward and bouncing back along the Y direction forms the characteristic modes that only propagate laterally along the waveguide.

Transition into the waveguide regime can be illustrated in various waveguides with spatial confinement around the polariton wavelength. Figure 2-12 shows the lateral propagation of THz phonon-polaritons at a certain time after the optical excitation along the waveguide geometrical center. The thinner the waveguide, the faster the propagation starts to follow the waveguide behavior after the optical excitation. The propagation speeds are decided by waveguide dispersion, and the first mode propagates longer and is also usually stronger due to higher excitation efficiency in the

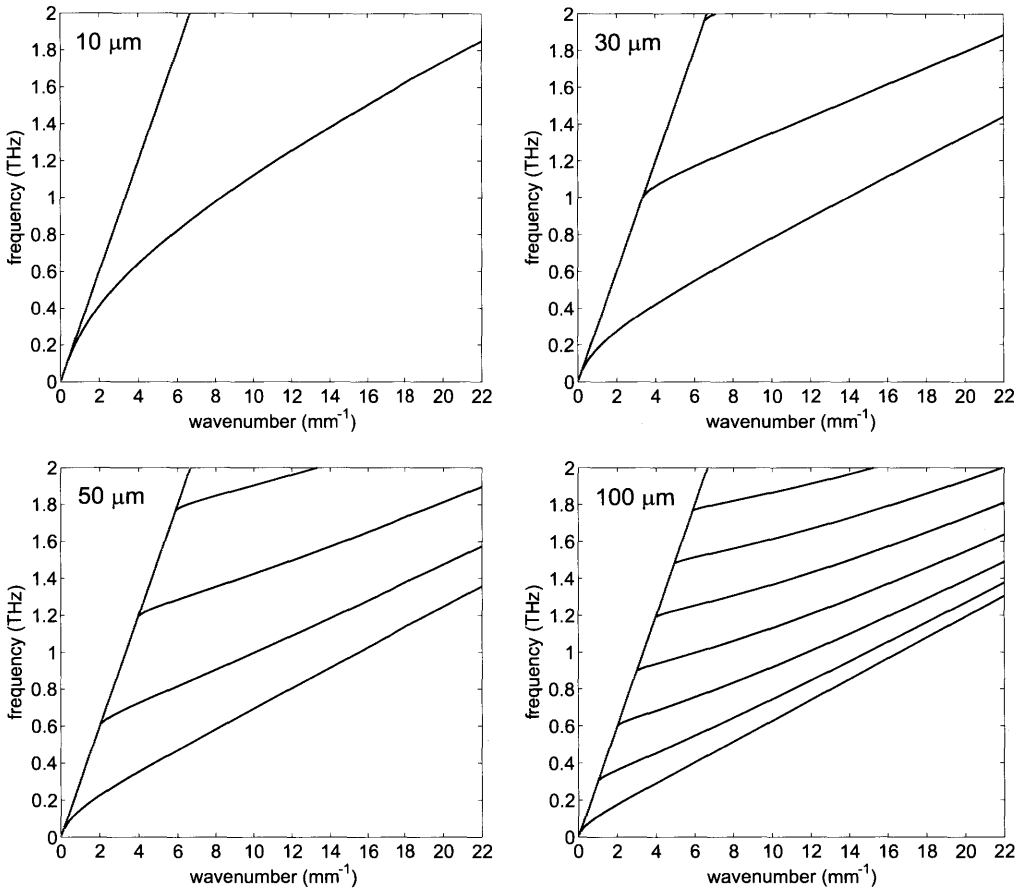

Figure 2-11: Dispersion diagrams of the first few modes in $LiNbO_3$ waveguides. As the waveguide thickness increases, these modes gradually move toward the bulk dispersion curve, and the gaps between them decrease until the bulk regime is reached.

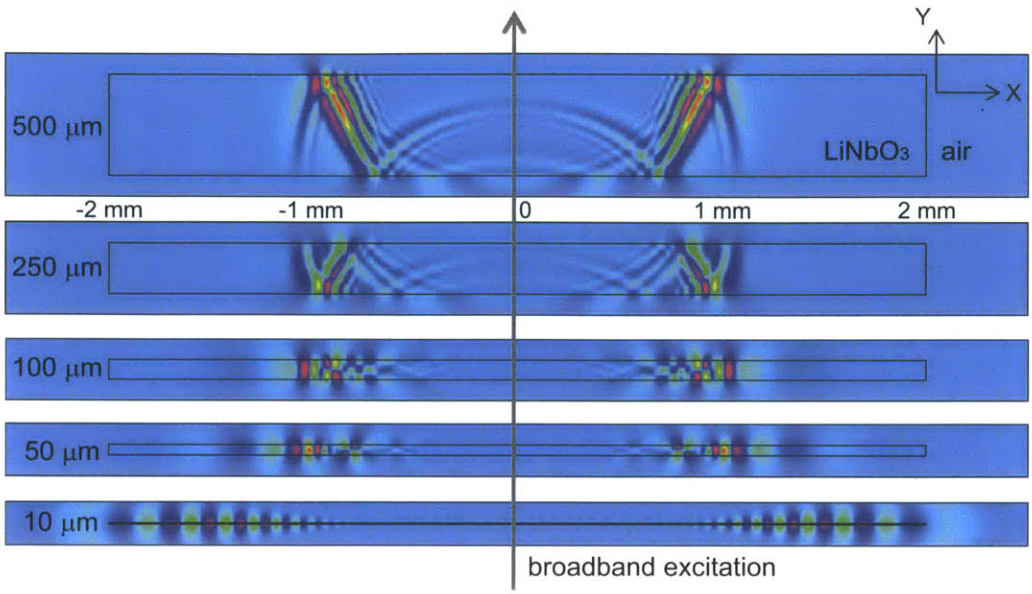

Figure 2-12: Lateral propagation of THz phonon-polaritons at a certain time after the optical excitation along the waveguide geometrical center. The multi-mode behavior begins to appear when the crystal is as thin as the polariton wavelength, and transitions into the waveguide regime.

waveguide regime.

From a dynamic point of view, significant inter-mode dispersions can be found especially when the waveguide regime is reached, since different modes are not continuous on the dispersion diagram. Given the concave shape of these modes, within the same mode higher frequencies of the electromagnetic field correspond to slower phase velocities due to the intra-mode group velocity dispersion. When a broadband THz wave is excited in the waveguide, wavepacket components belonging to different modes quickly spread, become distinct from each other, and show the characteristic waveguide multi-mode behavior, as illustrated in Figure 2-13. The intra-mode group velocity dispersion also appears, but the wavepacket belonging to the same mode is spatiotemporally continuous since these components are continuous on the same dispersion curve.

Fourier transform of THz wave propagation space-time plots yield the dispersion relations that fit well with the calculated dispersion diagrams, as shown in Figure 2-14. The wavevector and frequency components are controlled by the spatiotemporal intensity envelope of the optical pulse. Similar to the bulk crystal case, the

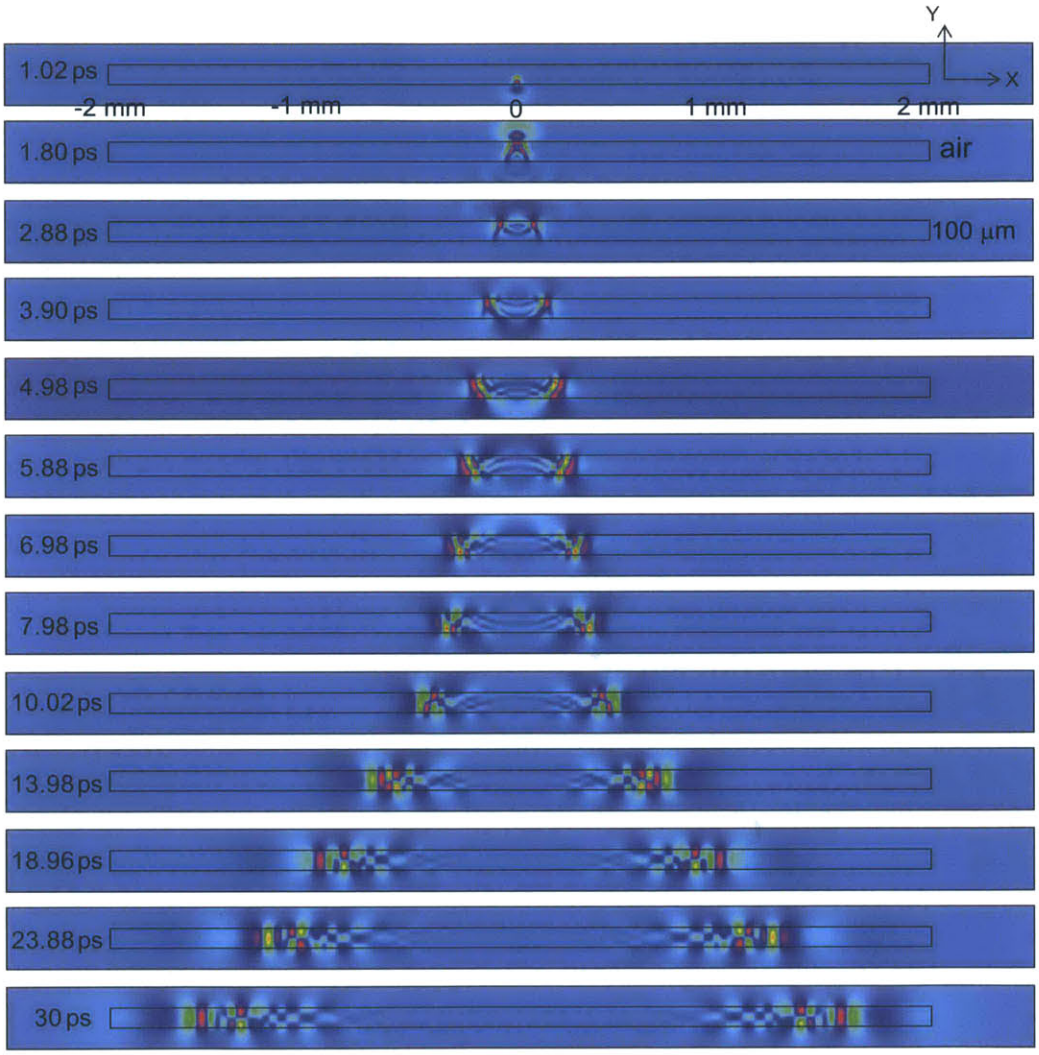

Figure 2-13: Characteristic multi-mode THz waves propagating laterally along the waveguide due to inter- and intra-mode dispersion. Wavepackets of different modes gradually become distinct, while wavepackets of the same mode spread out but remain spatiotemporally continuous.

tuning is more sensitive to the spot size with ultrashort pulse excitations, where laser beams that are focused more tightly into the waveguide can excite more wavevector components.

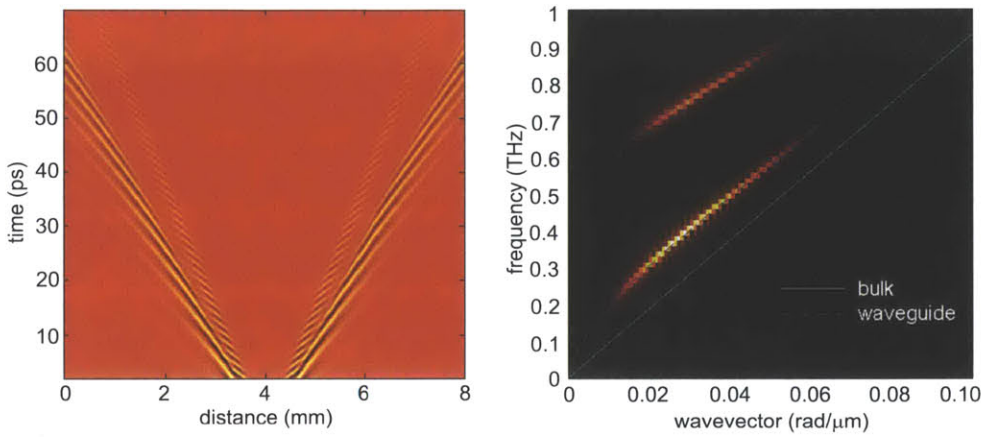

Figure 2-14: Space-time plots and dispersion curves of THz wave lateral propagation in a LiNbO3 waveguide. The THz wavevector and frequency components are controlled by the spatiotemporal intensity envelope of the optical pulse.

2.3.3 Phonon-polariton enhancement

Phonon-polariton focusing is a straightforward way of enhancing the electric field amplitude, and this has been spatiotemporally imaged with a laser-machined elliptical reflective geometry [36] in a waveguide. Full-circle and semicircular optical excitations [107, 108] have also been demonstrated and imaged in experiment with an axicon-lens combination. Phonon-polariton interactions with THz resonant antennas deposited on a waveguide surface can give about 40 fold field enhancement [123]. THz response with nanostructures can result in significantly higher field enhancement factors up to many thousands [84]. These methods are particularly interesting because the large amplitude motion can facilitate the nonlinear THz experiment and allow the observation of nonlinear response such as new frequency generation and phase modulation. Significant increase of generation efficiency for frequency doubled components has been confirmed [84]. As an illustration, Figure 2-15 shows the simulations of a phonon-polariton wave generated by a semielliptical optical pulse as it propagates

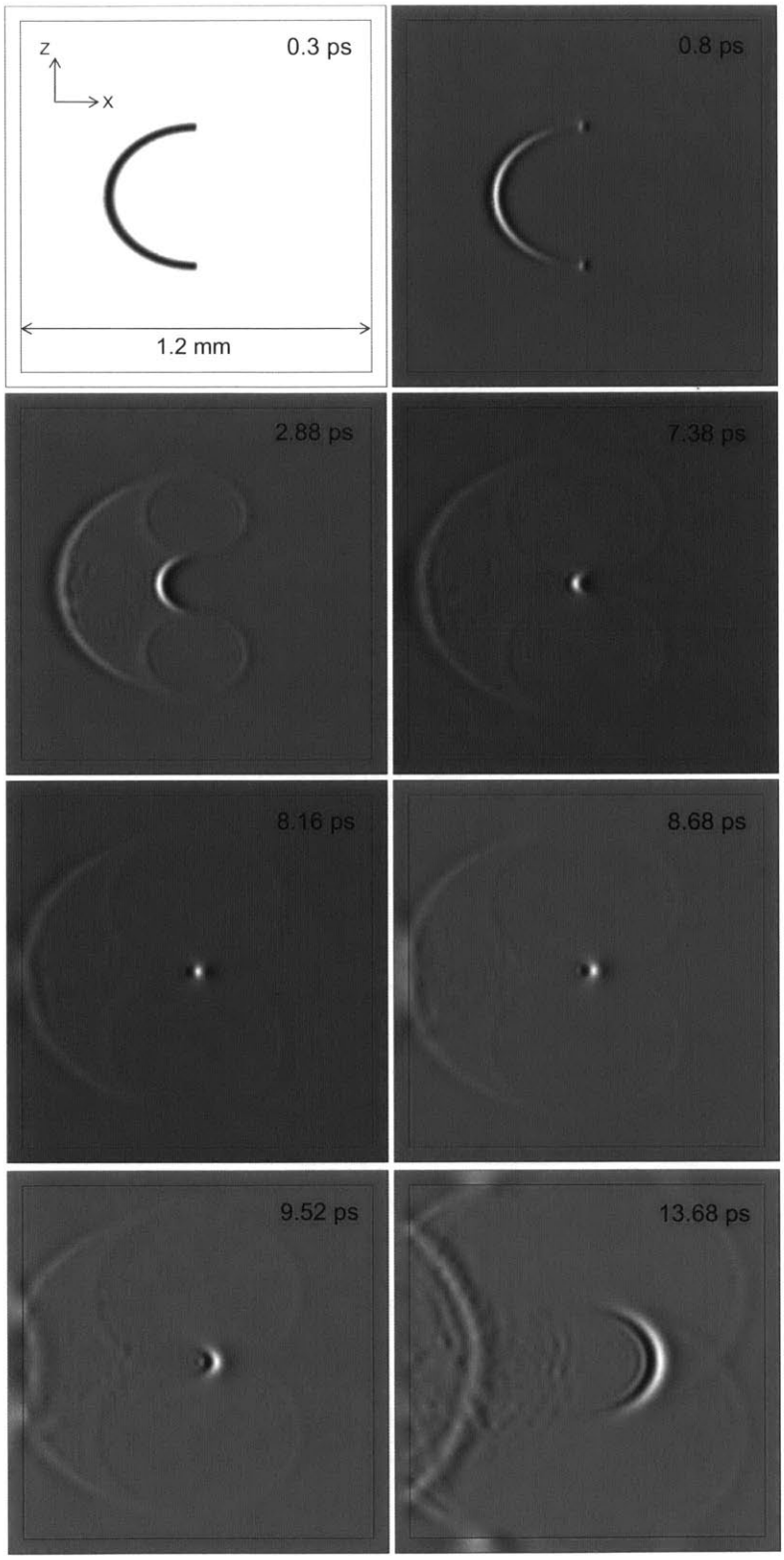

Figure 2-15: A phonon-polariton wave generated by a semielliptical optical pulse propagates and focuses at the center with enhanced amplitude.

and focuses at the center with enhanced amplitude.

Chapter 3

Experimental Methods and General Considerations

Coherent lattice vibrational waves are particularly interesting because a huge number of ions move in a cooperative phase-coherent manner on a macroscopic scale. Many classical wave behaviors such as superposition, diffraction, interference, and tunneling have been observed and directly visualized [36]. Nonlinear lattice dynamics and spectroscopy require large amplitude vibrational motions and the strongly correlated electric field in the case of phonon-polariton waves. Recent progress in this effort includes coherent amplification and focusing through patterned material structures [107, 108], spatiotemporal optical waveform control [37], resonance with antennas and metamaterials [123, 84] in a slab ferroelectric waveguide, and amplification with a tilted optical intensity front in a bulk crystal [55]. In this chapter, experimental methods and techniques of THz phonon-polariton generation and amplification are briefly introduced, with emphasis on how to generate and detect polariton waves propagating at light-like speed, how to collect data and improve signal with laser fluctuations, how to achieve the large intensity front tilt required for noncollinear velocity matching, and how to collect and focus THz pulses for experimental calibration and measurement. Some of contents and derivations are based on the work of group members and collaborators [122, 51, 136], and these experimental methods are presented here to provide general considerations and details on which experimental

results in this thesis were built.

3.1 Phonon-polariton generation and detection

The experimental setup for the generation and detection of THz phonon-polariton waves in a $LiNbO_3$ waveguide is illustrated in Figure 3-1. The 800 nm pump light, operating at a 1 kHz repetition rate, is focused onto the sample for phonon-polariton generation [36]. The probe pulse is transform-limited, frequency-doubled 400 nm light. The phonon-polariton waves introduce transient birefringence in the sample that is detected by the probe pulse passing through it. The static birefringence can be compensated by the same type of crystal with the optic axis perpendicular to the sample. The cross-polarizers ensure that the probe pulse is polarized at 45 degree relative to the optic axis of the crystal. The phase information can be converted to THz field amplitude with a quarter waveplate (QWP) in front of the polarizer. The variable ND filter can adjust the light intensity for balanced detection, and the pump can be modulated at 500 Hz for reference detection. The dichroic mirror reflects the 400 nm probe and allows the 800 nm pump to pass through, so that the phase and amplitude information of the probe beam are not affected by its transmission through the mirror. The filter reduces the pump light for accurate probe intensity detection by the photodiode.

The pump beam can be transform-limited or spatiotemporally shaped for phonon-polariton generation and control. The probe beam operates at 400 nm in a collinear geometry for the transmission, filtering, birefringence measurement, and compensation. A probe beam with a different wavelength is an alternative option that can be attained with an optical parametric amplifier (OPA). The probe beam can also be expanded to centimeter diameters through the sample to record time-resolved imaging of phonon-polariton generation and propagation in a waveguide structure.

THz phonon-polariton detection is based on the pump-induced change in the refractive index due to the electro-optic effect of the crystal [36], which is proportional

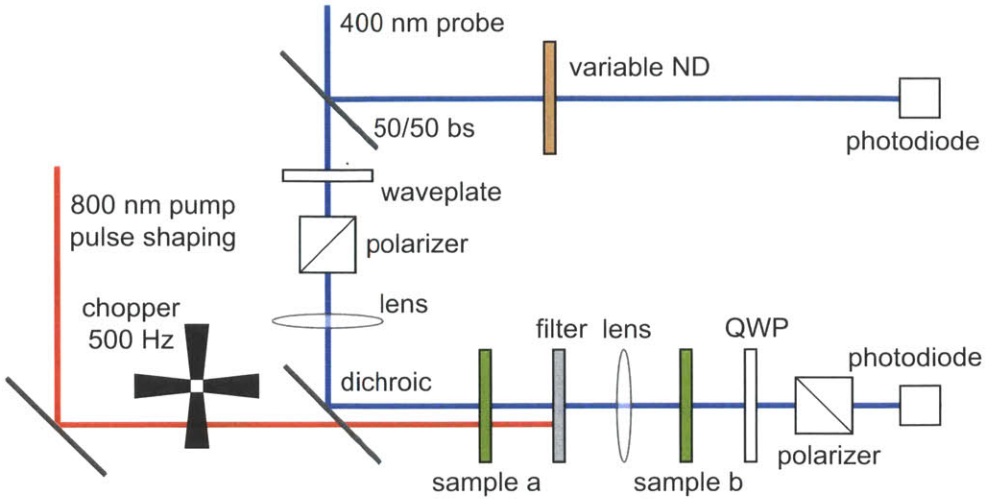

Figure 3-1: The experimental setup for the generation and detection of THz phonon-polariton waves in a $LiNbO_3$ waveguide. The phonon polariton waves introduce transient birefringence in the sample, which is detected by the probe pulse passing through it, and the static birefringence can be compensated by the same type of crystal with optic axis perpendicular to the sample. The cross polarizers are to make sure the probe pulse is polarized at 45 degree relative to the crystal optic axis, and the phase information can be converted to THz field amplitude with a quarter waveplate (QWP) in front of the polarizer. The variable ND filter can adjust the light intensity for balanced detection, and the pump can be modulated at 500 Hz for reference detection.

to the THz electric field as follows:

$$\frac{1}{n_i^2} = \frac{1}{n_i^2}\bigg|_{E=0} + \sum_i r_{ij} E_j \tag{3.1}$$

where r_{ij} is the electro-optic tensor. For THz generation in $LiTaO_3$ and $LiNbO_3$ with symmetry group 3m, the polarizations of the THz electric field and the probe light are along the crystal axis. The THz-induced phase difference between the vertical and horizontal polarization components [77] of the probe pulse is given by:

$$\Delta\phi = -2\pi \frac{l}{\lambda_{opt}} (\Delta n_{eo} - \Delta n_o) \tag{3.2}$$

$$= -2\pi \frac{l}{\lambda_{opt}} \frac{r_{33} n_{eo}^3 - r_{13} n_o^3}{2} E_{THz} \tag{3.3}$$

where l is the crystal thickness, λ_{opt} is the probe wavelength, and n_{eo} and n_o are the extraordinary and ordinary refractive indices respectively.

3.2 Laser fluctuation analysis and data acquisition

Assuming balanced detection with photodiodes in the probe path and chopping with a modulation frequency at half of the pump repetition rate, the probe beam that photodiodes can detect are pulse sequences that contain signal information with pump pulses on and off alternatively. The intensities can be expressed as follows,

$$S_1 = I_{s0}(1 + \delta_{s1} + M(I_{pump}(1 + \delta_{pump}))^n) \tag{3.4}$$

$$S_2 = I_{s0}(1 + \delta_{s2}) \tag{3.5}$$

$$R_1 = I_{r0}(1 + \delta_{r1}) \tag{3.6}$$

$$R_2 = I_{r0}(1 + \delta_{r2}) \tag{3.7}$$

where δ is the shot to shot laser fluctuation, I_{s0} and I_{r0} are the average signal and reference probe intensities at the photodiodes, I_p is the average pump intensity, M is the signal magnitude, and n represents pump-induced nonlinear orders.

The data acquisition and processing system in this experiment is based on photodiodes, a current amplifier, and a DAQ card, with the signal-noise level improved by balancing, chopping, and averaging techniques [122]. With the laser repetition rate at 1 kHz and chopping modulation at 500 Hz, the probe goes through the detection region of the sample with the pump alternating between on and off states. The photodiode intensities are S_1 when the pump is on and R_1 when the pump is off. The other photodiode for balanced detection has similar alternations with intensities S_2 and R_2 corresponding to on and off states respectively. The total signal modulation can be calculated by

$$\frac{\Delta I}{I_0} = \frac{S_1/R_1}{S_2/R_2} - 1 \tag{3.8}$$

One of the advantages of a DAQ card-based detection system is the rapid scanning technique. The delay stage is accelerated to a certain velocity, and data are recorded at this constant, fast speed until the acquisition stopped. The delay stage then returns to the starting point for the next round. The averaging time at each time delay is

very short, such that large signals above the noise level can be measured by a quick display of the temporal evolution of the signal and other relevant information such as Fourier spectra. With this technique, the dynamics in a 10 ps time window can be measured at a refresh rate of about 1 Hz, which gives real time feedback and can help improve the optical alignment and signal optimization.

3.3 Tilted intensity front technique

Upon transmission through [83] or diffraction off a grating [82], the intensity front of an incident optical pulse is tilted, and an angle ψ between the phase front and pulse front is formed. One of the major reasons is due to the different path length a beam with finite diameter has to travel, as shown in Figure 3-2. For gratings with groove spacing d, the diffraction can be written as:

$$\sin\alpha + \sin\beta = \frac{\lambda}{d} \tag{3.9}$$

where α is the incident angle, β is the diffraction angle, and λ is the wavelength of the incident beam or one of its frequency components.

Based on the path length difference, the equations among angles α, β, and the tilt γ can be written as

$$\tan\gamma = \frac{\sin\alpha + \sin\beta}{\cos\beta} \tag{3.10}$$

Taking the derivative of the equation 3.9 with respect to γ can give the angular dispersion for beams with multiple frequencies,

$$\frac{d\beta}{d\lambda} = \frac{1}{d \cdot \cos\beta} \tag{3.11}$$

which can further be written as

$$\tan\gamma = \lambda\frac{d\beta}{d\lambda} \tag{3.12}$$

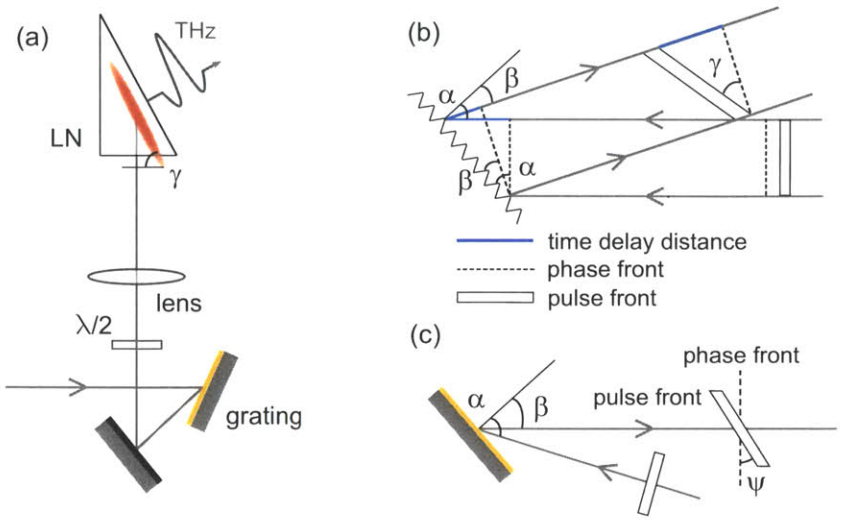

Figure 3-2: Illustrations of (a) an optical intensity front tilted by a diffraction grating [132], (b) the time delay distance that different parts of the pulse travel gives rise to the pulse front tilt [51], and (c) the angle ψ between the pulse front and the phase front for frequency components contained in the ultrashort laser pulse [82].

In a tilted intensity front experiment, the grating is typically around 2000 lines per mm, the pump central wavelength is at 800 nm, the spacing is 0.5 μm, and the incident angle α is about 61 degree [136]. The initial tilt γ in this configuration is therefore 65.9 degree.

The tilted intensity front is imaged through a one or two-lens imaging system, and between the grating and its image around the imaging place, the lateral dimension proportionally shrinks but the temporal dimension stays the same because the time delay is a constant. Upon entering the crystal, the lateral size of the beam is the same, and the temporal delay is also the same but the spatial span shrinks due to the optical index in the crystal. This can be written as

$$G2 = G1, \quad H2 = H1 \times M \tag{3.13}$$

$$H3 = H2, \quad G3 = \frac{G2}{n_{opt}} \tag{3.14}$$

so the tilt angles have the following equations

$$\tan\gamma_3 = \frac{\tan\gamma_2}{n_{opt}} = \frac{\tan\gamma_1}{n_{opt} \times M} \tag{3.15}$$

where M is the imaging ratio. In our experiments with near-infrared laser pulses, n_{opt} in $LiNbO_3$ is 2.25, M is 0.5 for 2:1 imaging , and this will give the required tilt in the crystal γ_3 around 63 degree. All the angles at various positions are between the tilted intensity front and the plane perpendicular to the wavevector direction.

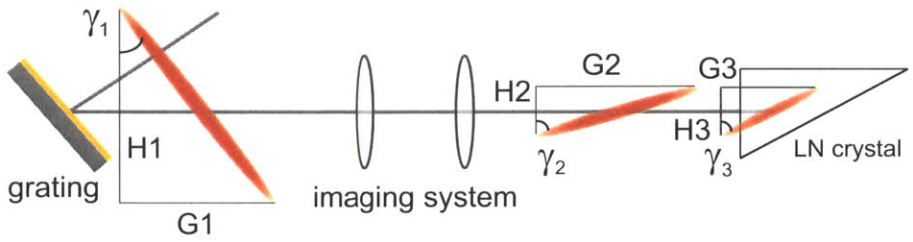

Figure 3-3: Illustration of the tilt angle change through the imaging system and the crystal index. The imaging system proportionally shrinks the lateral dimension H, which is perpendicular to the wavevector direction, and the crystal index mainly changes the temporal dimension G.

For ultrashort laser pulses with relatively broad bandwidths, the optical pulse can temporally spread and spatially diverge as it propagates in free space due to the large angular dispersion $d\beta/d\lambda$, especially with a high-density grating as the diffraction device. This effect can be analyzed in terms of the group velocity dispersion along the propagation direction and the spectral lateral walkoff perpendicular to the propagation direction. A dimensionless factor u has been calculated to characterize the spectral lateral walkoff [82] in the configuration with ultrashort laser pulses

$$u = (\frac{2\kappa_1\kappa_2 z}{\sigma\tau_0})^2 \tag{3.16}$$

where τ_0 is the original pulse duration, σ is the beam waist, z is the propagation distance, and κ_1 and κ_2 are

$$\kappa_1 = -\frac{\cos\alpha}{\cos\beta} \tag{3.17}$$

$$\kappa_2 = -\frac{m\lambda^2}{2\pi cd\cos\beta} \tag{3.18}$$

where m is the order of diffraction that is 1 in our experiment, c is the speed of light, d is the grating groove spacing, and λ is the central wavelength. The only changing

factor in u once the configuration is set is the propagation distance z.

The grating image in the crystal can be well approximated to be a replica of the grating through good imaging systems such as an achromatic lens, and the change in the process from the object to the image is basically geometrical tilt angle change. Further propagation in the crystal within a short distance from the grating image can also be analyzed as a replica of the original propagation right off the object grating in free space, and this is the aforementioned group velocity dispersion and spectral lateral walkoff. The dimensionless factor u is function of the propagation distance z off the grating, and the tilt angle ψ can be written as

$$\tan\psi = \frac{\tan\psi_0}{1+u} \tag{3.19}$$

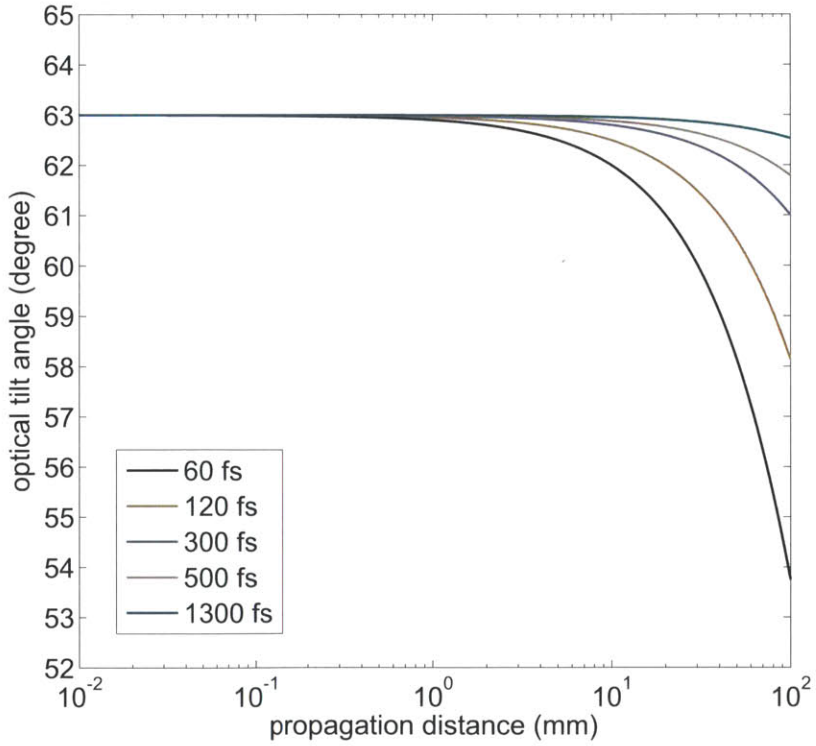

Figure 3-4: Calculated tilt angle change as a function of the propagation distance with several different durations. Since the evolution of interest is around the grating image in the generation crystal, the optical index is taken into account.

For the evolution of grating image in the crystal, the optical index needs to be

taken into account, which mainly affects the parameter κ_2. With the parameters in our experiment, $\kappa_1 = -\cos\alpha/\cos\beta$, $\kappa_2 = -(m\lambda^2)/(2\pi cd\cos\beta n_{opt})$ [82, 136], and the tilt angle evolution as a function of the propagation distance z for a beam with 2 mm diameter can be shown in Figure 3-4. Note that based on the results in [136], a few considerations about the incident and diffracted angles, and crystal index, are taken into account because the evolution of interest is around the grating image in the generation crystal. The smaller the beam waist and the shorter the pulse duration, the more significantly the tilt angle will change. The optical index of the crystal brings a factor of 2.25, and this reduces the spectral lateral walkoff effect.

3.4 THz focusing and detection

THz generation based on this method is intrinsically phase stable since the travel distance for THz amplification is set by the generation crystal. THz radiation is mainly in the form of a Gaussian beam, and can be well-collimated and focused to a spot with off-axis parabolic mirrors. The focal size of a Gaussian beam can be written as

$$2\omega_0 = \frac{4\lambda}{\pi}\frac{F}{D} = \frac{2\lambda}{\pi}\frac{1}{\Theta} \tag{3.20}$$

where λ is the wavelength of the focused light, F is the focal length of the focusing element, D is the diameter of the beam incident on the focusing element, and Θ is the total angular spread far from the waist.

The typical THz pulse is near-single-cycle temporally with a large transient peak and two small side lobes. The THz pulse energy can be measured through a pyroelectric detector with response resolution around 20 ms. In most spectroscopic experiments, the peak electric field is of considerable interest, which can be estimated as

$$E_{peak} = \sqrt{2\eta_0 \frac{W}{\tau_{\mathrm{FWHM}} A_{eff}}} \tag{3.21}$$

where W is the pulse energy, η_0 is the free-space impedance 377 Ω, τ_{FWHM} is the full width at half maximum (FWHM) of the ultrashort THz trace, and A_{eff} is the beam cross-section area at the focus. As an example, THz pulses with 2 μJ energy and duration about 1 ps can be focused down to the diffraction limit with spot size about 300 μm, so the peak electric field can be calculated to be 1.2 MV/cm, which shows good agreement with the reported electro-optic measurement [58].

Detection of the THz electric field trace can be conducted through electro-optic sampling in a nonlinear crystal such as ZnTe and GaP. The THz electric field induces transient birefringence, and the polarization of a variably delayed spatially overlapped optical probe pulse can be rotated based on the amplitude of the field. The rotation can be measured through the relative intensity of its polarization components, which can induce balanced photodetector signal $\Delta I/I$. The equation describing the electro-optic sampling measurement is

$$\sin^{-1}(\frac{\Delta I}{I}) = \frac{2\pi n_0^3 r_{41} t_{\text{EO}} E_{\text{THz}} R}{\lambda_0} \tag{3.22}$$

where n_0 is the refractive index, R is the crystal thickness, and r_{41} and t_{EO} are the nonlinear coefficient and transmission coefficient of the electro-optic crystal respectively.

3.5 Chirped pulse temporal shaping

The chirp-and-delay has been demonstrated as an effective temporal shaping method for multicycle THz generation, in which a quasi-sinusoidal optical intensity modulation with a specified frequency and number of cycles is formed in the time domain.

An optical pulse with center frequency ω_0 is chirped at rate β. If two equivalent parts are recombined interferometrically with a relative time delay τ, the instantaneous frequencies $\omega = \omega_0 + \beta t$ and $\omega = \omega_0 + \beta(t - \tau)$ are swept linearly across the pulse duration. If the time delay is relatively small compared to the stretched pulse duration, the interference between two pulses leads to a quasi-sinusoidal intensity

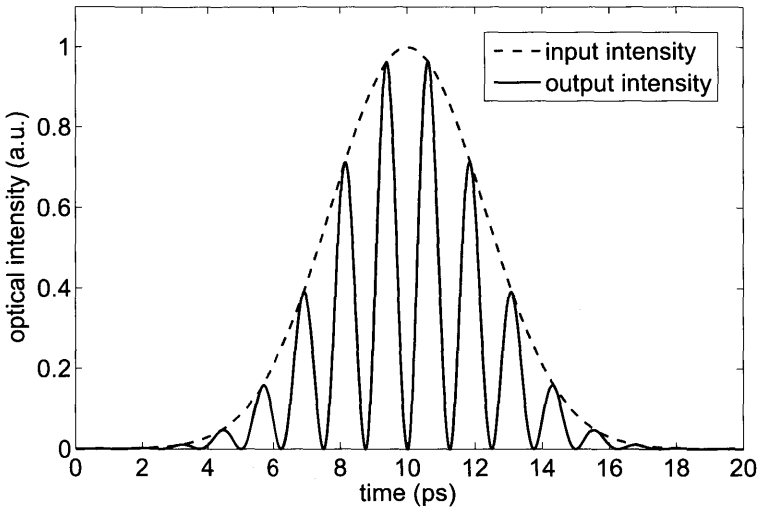

Figure 3-5: An illustration of the Gaussian intensity envelope of input chirped pulses and the modulated intensity of the output.

modulation at the constant difference frequency $\Omega = \beta\tau = 2\tau/T_0T_1$, where T_0 is the transform-limited $1/e$ field half-width, and T_1 is the stretched pulse $1/e$ field half-width [120]. The amplitude envelope of the transform-limited optical pulse and its Fourier amplitude can be expressed as:

$$E(t) = E_0 e^{-\frac{t^2}{T_0^2}}, \quad E(f) = E_0' e^{-\pi^2 T_0^2 f^2} \tag{3.23}$$

the intensity version is

$$I(t) = I_0 e^{-\frac{2t^2}{T_0^2}}, \quad S(f) = S_0 e^{-2\pi^2 T_0^2 f^2} \tag{3.24}$$

and the duration and bandwidth are

$$I_{FWHM} = 2\sqrt{\ln 2}\frac{T_0}{\sqrt{2}}, \quad S_{FWHM} = 2\sqrt{\ln 2}\frac{1}{\sqrt{2}\pi T_0} \tag{3.25}$$

so the number of cycles within the full width at half maximum (FWHM) of the intensity envelope (Gaussian in profile if the transform-limited pulse was) can therefore

be written as

$$N = f_{beat} \times I_{FWHM} = \frac{\tau}{\pi T_0 T_1} \times 2\sqrt{\ln 2}\frac{T_1}{\sqrt{2}} = \frac{\tau\sqrt{2}\sqrt{\ln 2}}{\pi T_0} = \sigma\tau \tag{3.26}$$

where σ is the optical pulse bandwidth. Therefore the modulation frequency can be continuously tuned by varying the chirp and/or the delay, while the number of cycles can be independently controlled by varying only the delay.

3.6 Etalon interferometer

One of the experimental methods to realize the temporal overlap and delay of chirped pulses was through a Michelson interferometer, in which two optical arms are recombined with one of them variable delayed. Although a fraction of the pump energy will not appear in the detection arm, since the interference is in the time domain instead of the usual spatial configuration where the energy from one arm can be redistributed into the constructive detection arm, the total interference has good quality in terms of the optical modulation depth and can be monitored with a spectrometer through spectral interference at 800 nm.

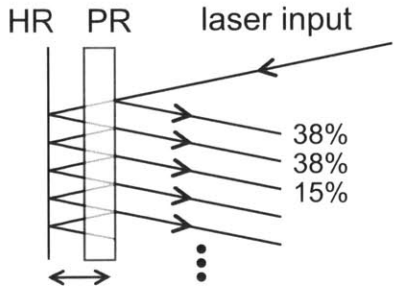

Figure 3-6: Illustration of the etalon interferometer made by a high reflector (HR) and partial reflector (PR) at 800 nm. Each of the first and second reflections has 38% of the incident light and each higher reflection has 38% of the previous one. The gap between the HR and PR can be tuned to introduce variable time delay.

A homemade Gires-Tournois etalon made by a partial reflector (38% reflection efficiency) and a high reflector can introduce the variable time delay between chirped

pulses, as shown in Figure 3-6. Each of the first and second reflections has 38% of the incident light, which is the primary contribution to the intensity modulation. Each higher reflection has 38% of the previous one among the rest of the pulses with total 24% of the incident light. The advantages of this arrangement are common path optics for interferometric stability of the superposed chirp-and-delayed pulses and negligible pump power loss since multiple reflections all propagate collinearly. The peak intensity of the modulated optical output is twice as high as the incident one, which can contribute to experiments where high optical intensity is preferred, such as nonlinear frequency mixing or phase modulations.

Chapter 4

Generation of High Power Single-cycle and Multi-cycle Terahertz Pulses

This work is in collaboration with Dr. Xibin Zhou, Dr. Christopher A. Werley, and Dr. Harold Y. Hwang of the Massachusetts Institute of Technology.

The recently available tabletop generation of intense single-cycle THz pulses with microjoule energies [132] has become an essential experimental method in the emerging field of nonlinear THz optics and spectroscopy [55, 60, 61]. The generation process is based on the optical excitation of coherent phonon-polaritons through impulsive stimulated Raman scattering [124, 23, 36] in a ferroelectric crystal lithium niobate ($LiNbO_3$), and the coherent amplification is achieved through noncollinear velocity matching geometry by tilting the intensity front of optical pump pulses. Recent experiments have demonstrated 125 μJ THz pulse energy [42] with optical pulses of 1.3 ps duration, and a THz electric field amplitude exceeding 1.2 MV/cm [69] with THz pulses focused down to the diffraction limit. This ultrashort THz pulse with subpicosecond duration can be implemented as a transient electric field or magnetic field that is shorter than many dynamics in condensed phase materials and strong enough to induce many high-field phenomena. For many applications, frequency-tunable

multicycle THz pulses would be preferable to typical broadband single-cycle pulses. For example, multicycle pulses can excite a selected resonance without influencing neighboring modes or can simplify the identification of new frequency components generated in nonlinear THz processes. In time-resolved spectroscopy experiments, short multicycle pulses with well-defined, tunable frequencies can enhance the resonance feature while maintaining time resolution that is short enough to allow the observation of relaxation dynamics following pump pulse excitation. In this chapter, we present general background and experimental results of generation of ultrashort single-cycle and frequency-tunable multicycle THz pulses pumped with optical pulses at 1 kHz and 10 Hz repetition rates [137, 19]. Single-cycle THz pulses with more than 50 μJ pulse energy and multicycle THz pulses with more than 10 μJ pulse energy are achieved respectively.

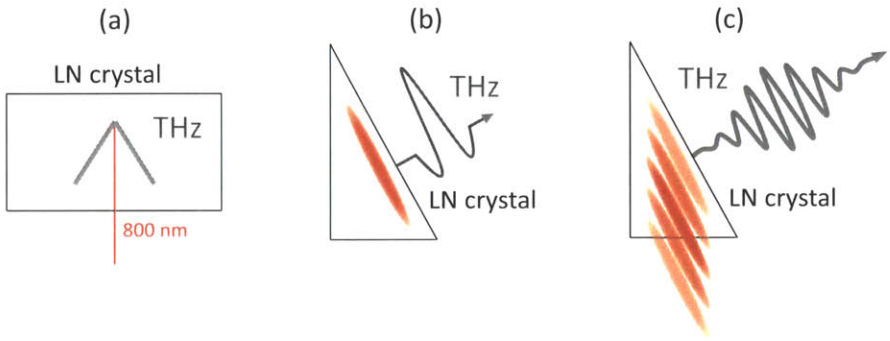

Figure 4-1: An illustration of generation of (a) a THz phonon-polariton wave pumped by a cylindrically focused optical pulse, (b) a high power single-cycle THz pulse by tilting the intensity front of a transform-limited optical pulse, and (c) a high power multicycle THz pulse by tilting the intensity front of a quasi-sinusoidal intensity-modulated optical waveform.

4.1 Noncollinear velocity matching configuration

In collinear velocity matching geometry with ultrashort laser pulses traveling through electro-optic materials, the newly generated THz waves can coherently add up with existing, previously generated THz waves, if the optical group velocity equals the THz phase velocity. This usually results in amplified generation of single-cycle THz waves in crystals such as ZnTe [9, 79] and GaP [59]. In some ferroelectric crystals with

higher nonlinear coefficients, conventional collinear velocity matching is not straightforward because of the high dielectric constant and refractive index in the THz region. Noncollinear velocity matching is possible by implementing sequences of spatially and temporally displaced optical pulses [134], or a tilted intensity front of a single pump laser pulse [52, 53], as shown in Figure 4-2. Since THz wave has a long wavelength on the order of 50 μm, the generated THz pulses should be continuous in either case after a short propagation distance, especially in the case of the far-field response [37].

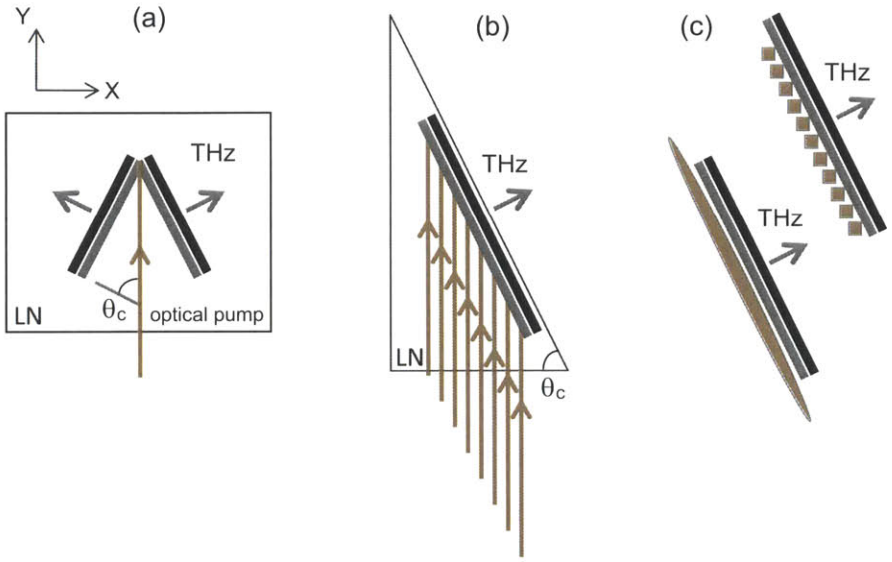

Figure 4-2: An illustration of noncollinear velocity matching geometry in a bulk $LiNbO_3$ crystal. (a) THz phonon-polariton waves pumped by a cylindrically focused optical pump pulse, (b) a discrete tilted intensity front realized through sequences of temporally and spatially displaced optical pulses, and (c) a continuous tilted intensity front visualized through imaging of a diffraction grating. The crystal optic axis is along the direction perpendicular to the plane of the figure.

In ferroelectric crystals, the THz frequency components that can be typically excited through the Raman and Stokes pairs contained within the optical bandwidth of the ultrashort laser pulse have approximately the same phase velocity and relatively long coherence length. This wide region of frequency components give rise to the near-single-cycle THz waveform. As shown in Figure 4-3, the longest enhancement and propagation length in the generation path is denoted as R, and this length should be long enough for the maximized amplification but shorter than the limit at which the group velocity dispersion begins to stretch the pulse and increase the phase cycles

under the envelope.

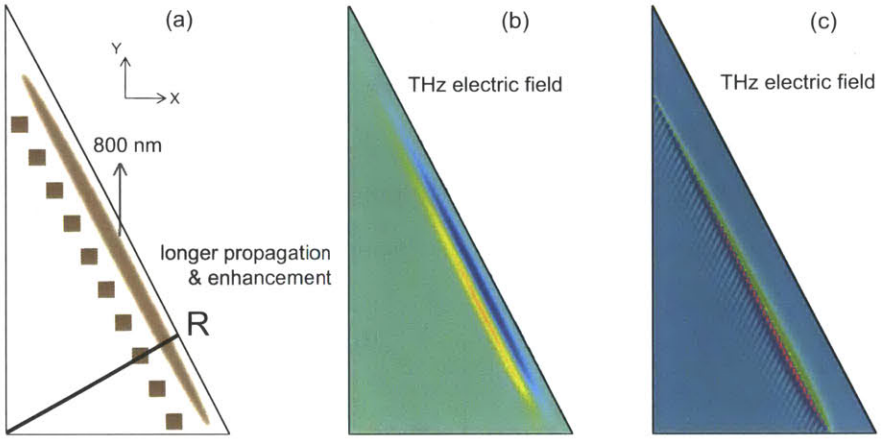

Figure 4-3: An illustration of (a) THz generation and propagation in a $LiNbO_3$ crystal. The peak of the tilted intensity front, discrete or continuous, was assumed to propagate vertically through the geometrical center of the crystal, and the peak of the THz electric field is approximately along path R where the most coherent enhancement is as well as the largest group velocity dispersion, (b) the single-cycle THz electric field pattern generated by an optical pulse with continuous tilted intensity front, and (c) the single-cycle THz electric field pattern generated by a sequence of temporally and spatially displaced optical pulses that form a discrete tilted intensity front.

One of the advantages of generation with sequence of temporally and spatially displaced optical pulses is that the wavevector is always along the forward propagation direction. For an individual optical pulse, the temporal duration is very short that enables the frequency tuning region up to 10 THz. The results from the generation process are primarily due to the wavevector tuning region, which is set by the individual pulse spatial width in the crystal. Some calculated results for THz generation based on spatiotemporally displaced pulse sequences are shown in Figure 4-4 and Figure 4-5. The individual pulse spatial width is inversely proportional to the size of the region in the wavevector domain as well as the size in the frequency domain that the pulses can cover.

THz pulse energy generated by the noncollinear velocity matching method based on pulse sequences or tilted intensity front can be scaled by increasing the size of pump areas and generation crystals. Since the THz radiation from the crystal surface is approximately round and the THz beam approximates a Gaussian beam, the pulse can be collimated and focused down to a small size so that the transient electric field

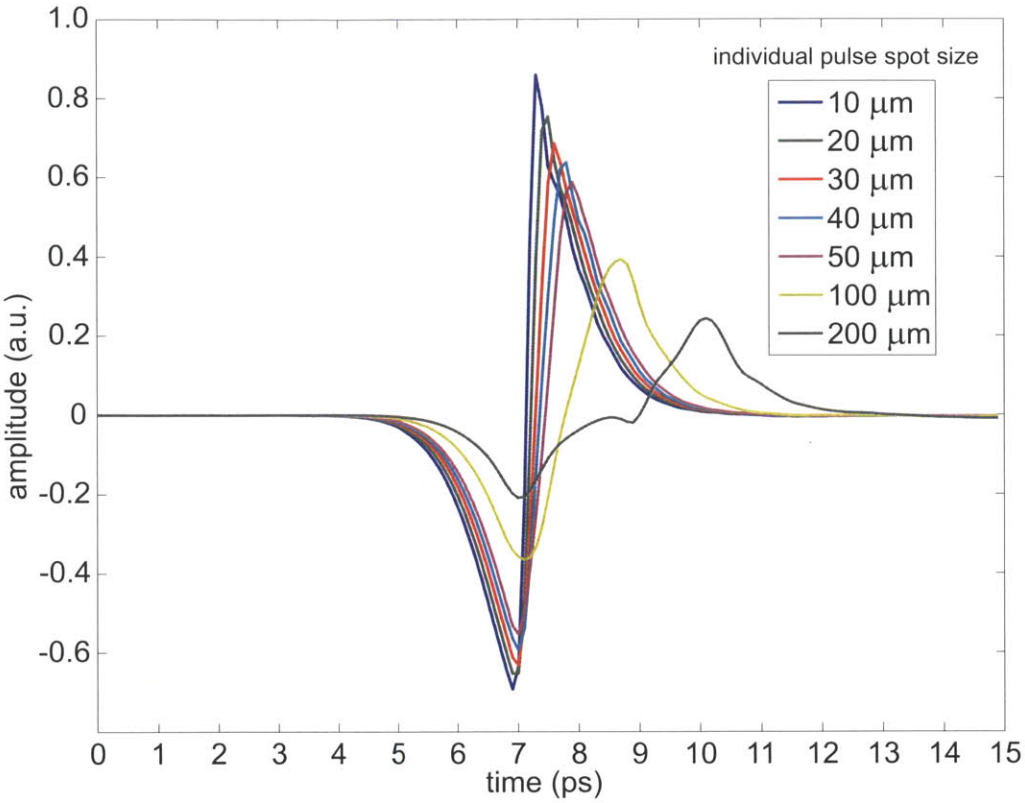

Figure 4-4: Calculated electric field traces of THz waves based on sequences of spatially and temporally displaced cylindrically focused optical pulses. These pulses are very short temporally, and THz waveforms are primarily influenced by the individual optical pulse spatial width.

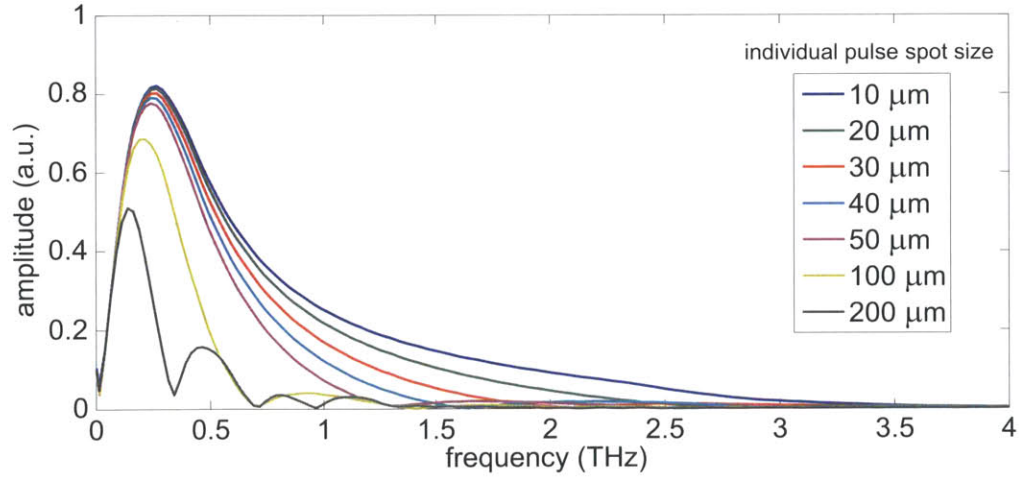

Figure 4-5: Fourier spectra of calculated THz field traces that were generated by sequences of spatially and temporally displaced cylindrically focused optical pulses. The individual pulse spatial width is inversely proportional to the size of the region in the wavevector domain as well as the size in the frequency domain that the pulses can cover.

can be large enough for nonlinear spectroscopic applications.

4.2 Calibration of the pyroelectric detector

THz pulse energy is measured by a pyroelectric detector with a thin $LiTaO_3$ crystal as the sensor. The crystal generates heat when the light is on, and the slight change in spontaneous polarization and temperature generate the signal voltage. The crystal cools down when the light is off, and the electric voltage across the crystal gradually decreases until the next light is on. The detector is designed to measure electromagnetic radiation in the spectral region from 0 to about 3 THz, and only pulsed or modulated radiation can be measured.

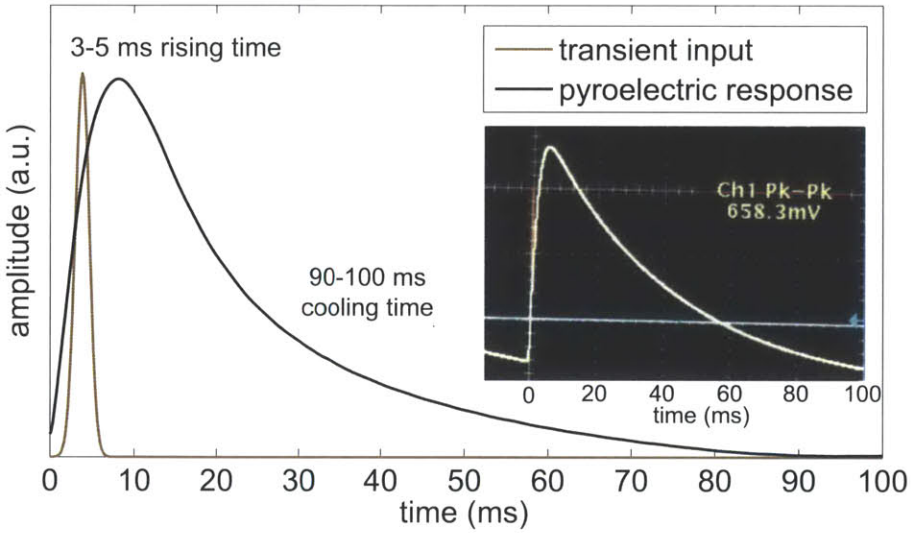

Figure 4-6: An illustration of, and the experimental signal from, the detector's response to an incident THz pulse with picosecond duration and microjoule-level pulse energies. The typical rising time is approximately 3 to 5 ms, and the cooling time for the crystal allowing the signal voltage to return to its original level is about 90 to 100 ms based on the RC configuration in the experiment.

For the pyroelectric detector in the THz generation experiment, the typical rising time is approximately 3 to 5 ms with single pulsed incident light, and the cooling time for the crystal allowing the signal voltage to return to the original level is about 90 to 100 ms based on the RC configuration in the experiment. Figure 4-6 shows an illustration of, and experimental signals from, the detector's response to an incident

THz pulse with picosecond duration and microjoule level pulse energies. For lasers with a repetition rate of 10 Hz or less, each pulse gives one peak signal voltage, so the pulse energies can be measured in a straightforward manner. For lasers with 1 kHz repetition rate, the 1 ms time interval between pulses is much shorter than the signal rising time so that the laser can be considered to be a continuous source, and the pulse energies can be measured at certain modulation frequencies.

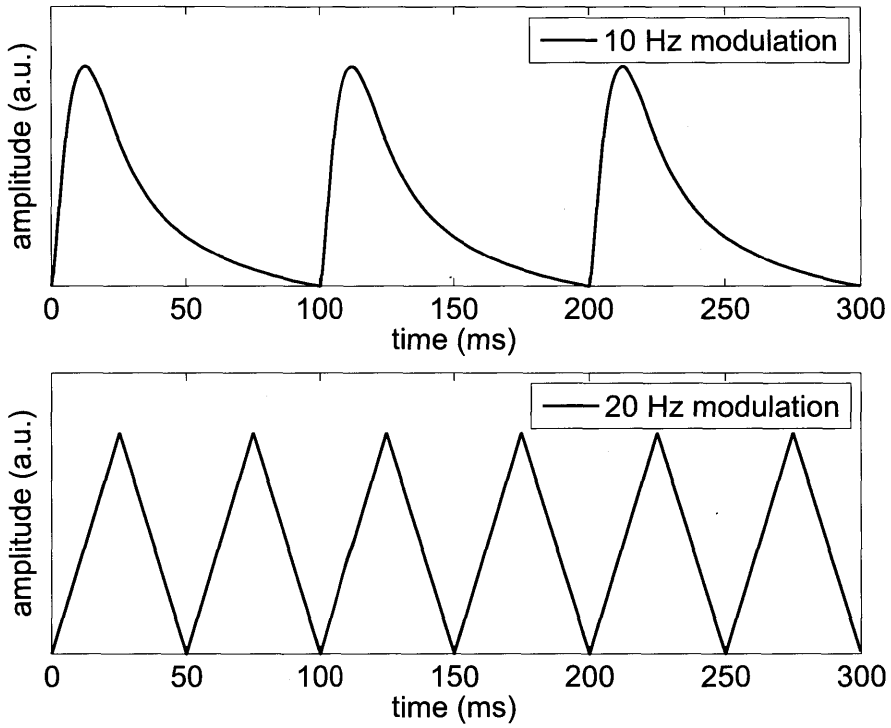

Figure 4-7: An illustration of the typical detector response to incident THz pulses with picosecond duration and microjoule-level pulse energies at 1 kHz repetition rate shows the rising/decaying features with modulations at 10 Hz and 20 Hz. The peak to peak voltage is proportional to the THz average power and light intensity.

As illustrated in Figure 4-7, the typical detector response to incident THz pulses with picosecond durations and microjoule level pulse energies at 1 kHz repetition rate shows rising/decaying features with square wave modulations at 10 Hz, and sawtooth signal voltage with square wave modulations at 20 Hz. This is due to the time intervals for the crystal to cool down when the light is off. The signal peak to peak voltage is proportional to the THz average power and light intensity.

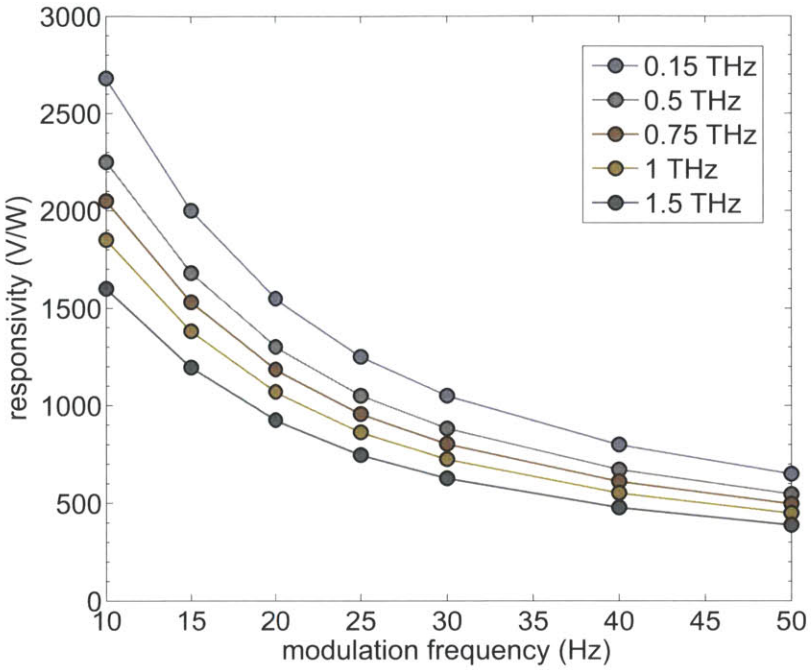

Figure 4-8: The responsivity of the pyroelectric detector as a function of the modulation frequency at multiple signal frequencies. The data points are based on the calibration data and instructions from the manufacturer.

4.3 Generation of near-single-cycle THz pulses

Generation of ultrashort single-cycle THz pulses through the tilted intensity front technique was conducted with a near-infrared laser at 1 kHz and 10 Hz repetition rates. The optical pump pulse energy was approximately 6 mJ at 1 kHz repetition rate from a two-stage commercial Ti:sapphire amplifier system, and can be amplified up to 35 mJ at 10 Hz repetition rate with a third amplifier stage. The updated 10 Hz system shows good spatial mode quality, optimized laser bandwidth, and a pulse-to-pulse energy stability at about 3.5 percent [137].

The experimental setup has been previously described in THz generation experiments with tilted intensity front technique [62, 132, 58]. The intensity front was generated by diffraction off a high-density grating and imaged onto the crystal through a single lens. The $LiNbO_3$ crystal is cut into a crystal so that the THz waves are at an incidence normal to the output surface. The optical pulse should be close to transform-limited while passing through the generation crystal such that some initial

chirp was introduced in the amplifier to compensate for dispersion before reaching the crystal. A typical THz field trace measured by electro-optic sampling in ZnTe and its corresponding Fourier spectrum are shown in Figure 4-9.

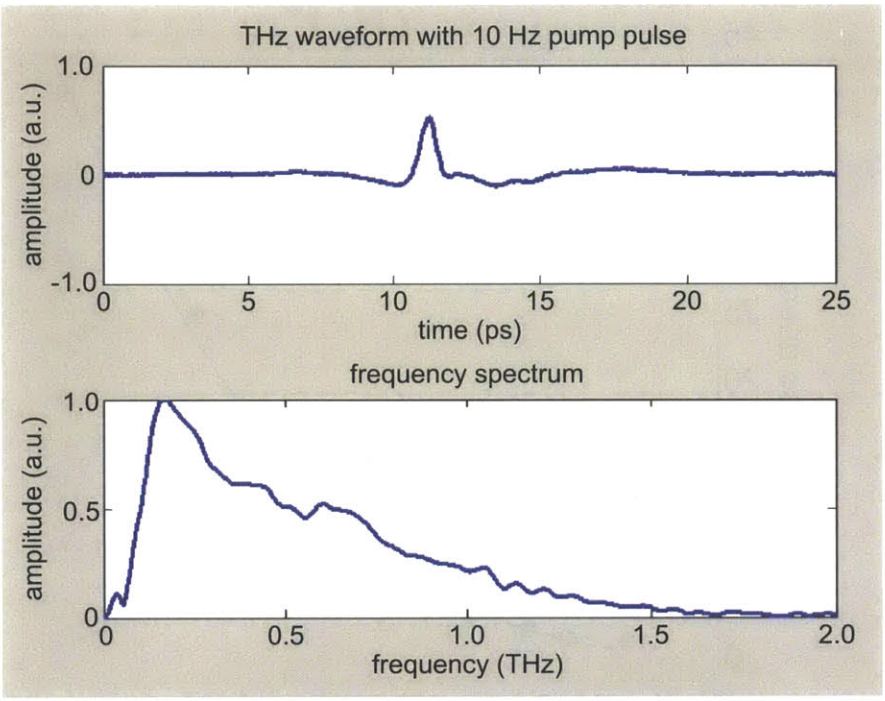

Figure 4-9: Experimental single-cycle THz field trace and the Fourier spectrum generated by the tilted intensity front technique in a $LiNbO_3$ crystal, pumped with a 25 mJ optical pulse at 10 Hz repetition rate.

THz pulse energies were measured with a calibrated Microtech pyroelectric detector that was mounted parallel to the output surface of the LN crystal. The visible and scattered second harmonic pump pulses were filtered by two layers of low-density polyethylene film in front of the detector. The signal voltage response as a function of modulation frequencies were measured with incident THz pulses at 1 kHz repetition rate and various modulations from 10 to 50 Hz, as shown in Figure ??. The experimental data are in agreement with the detector calibration data, especially at lower modulation frequencies where the laser input is closer to the continuous source. The average power and pulse energies therefore can be calculated. For example, with the signal peak-to-peak voltage at 1000 mV, 1 kHz repetition rate, and 20 Hz modulation

frequency, the corresponding average power is 1/1219 W = 0.82 mW, and the pulse energy is 0.82 μJ. Note that the calibration data need to be measured based on the radiation center frequencies.

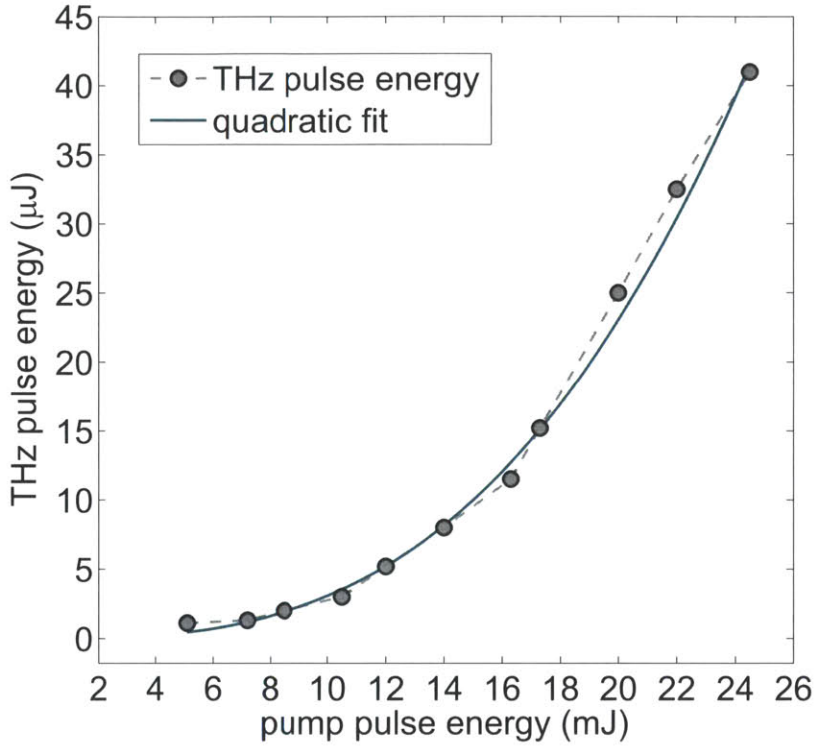

Figure 4-10: Experimental results from THz pulse energies as a function of optical pump pulse energies measured before the generation crystal by the tilted intensity front method and the quadratic dependence fit. The optical pulses were at 10 Hz repetition rate. The THz pulse energies in the high optical pump intensity region shows quadratic dependence due to the good spatial mode quality and optimized laser bandwidth in the updated laser system.

In ultrashort THz generation experiments with 35 mJ near-infrared optical pulses, detector saturation was observed in the high-intensity region where the transient signal voltage maximum appeared then quickly decayed in a few seconds. This may be due to saturation of the pyroelectric crystal or the amplifier capacitor which converts crystal voltage into detectable signals. The THz pulse energies were estimated to be more than 50 μJ at 10 Hz repetition rate.

THz pulse energies as a function of optical pump pulse energies was shown in Figure 4-10, where the optical pulses were at 10 Hz repetition rate. Previous studies

[54] have confirmed that, if the THz generation process is primarily a $\chi^{(2)}$ process, THz pulse energy should be proportional to the square of the optical pulse energy. The experimental data shows good agreement with a quadratic dependence on the optical pump pulse energy in this region. This is due to the good spatial mode quality, optimized laser bandwidth, and pulse-to-pulse energy stability in the updated 10 Hz laser system. With further optimized focusing, higher THz pulse energies should be possible based on previously reported work with lasers at kHz repetition rate.

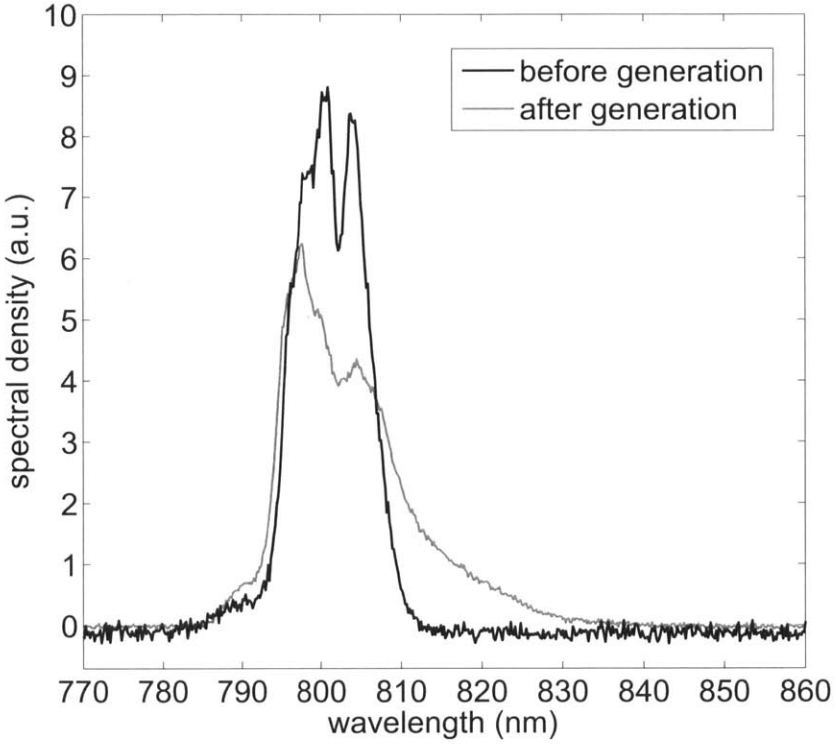

Figure 4-11: Optical spectrum measured before and after the generation crystal pumped with 20 mJ optical pulse. The spectral change can be observed through the large lobes in the long wavelength region from 800 to 850 nm due to high-energy THz generation.

The THz intensity as a function of horizontal position or the beam divergence was measured with optical pulses of both 1 kHz and 10 Hz repetition rates at 10 and 20 cm after the generation crystal, as shown in Figure 4-12. The spatial profile shows Gaussian shape which agrees well with the optimal THz generation. Also observed is that the THz beam divergence is larger for 10 Hz optical pulses, which may be due

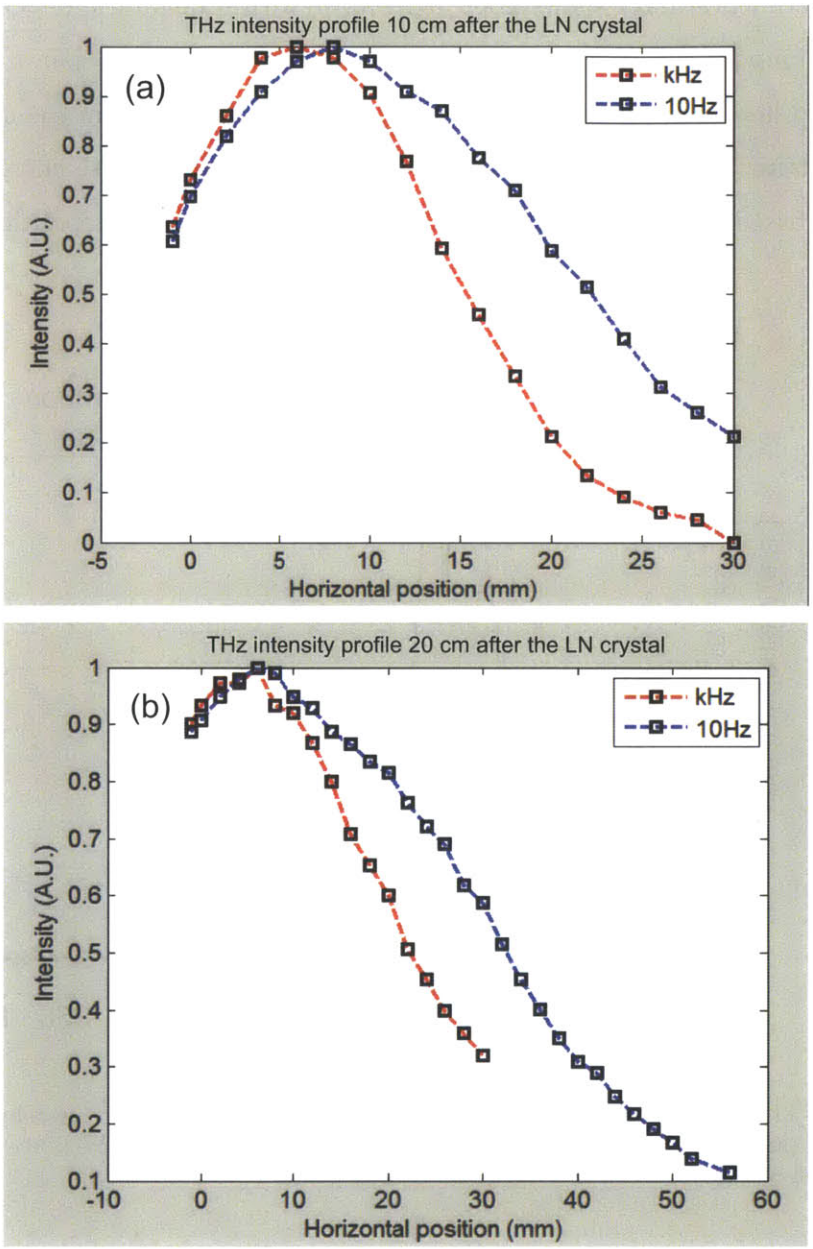

Figure 4-12: Experimental measurement of THz intensity as a function of horizontal position or beam divergence with optical pulses of both 1 kHz and 10 Hz repetition rates at 10 and 20 cm after the generation crystal. The spatial profile shows good agreement with a Gaussian beam, and the divergence is larger with higher optical pulse energies.

to the strong nonlinear processes with higher optical pulse energies in the generation crystal. The high-energy THz pulses can be collimated with off-axis parabolic mirrors, and imaged onto a sample for spectroscopic applications at high field strength.

The optical spectrum was also measured before and after the generation crystal as shown in Figure 4-11. The spectral change can be observed through the large lobes in the long wavelength region from 800 to 850 nm due to high-energy THz generation. These new frequency components that cover a broad frequency region show the high optical-to-THz conversion efficiency.

4.4 Optical temporal pulse modulation

Generation of high power multiple-cycle THz pulses is achieved through temporal modulation of near-infrared optical pulses as inputs. In this experiment, the Gires-Tournois etalon is made by a partial reflector (38% reflection efficiency) and a high reflector to introduce the variable time delay between chirped pulses at 800 nm, as shown in Figure 4-13. The diameter of the high and partial reflector is one inch, and the gap can be continuously tuned from approximately 50 μm to 100 μm, introducing a time delay of 0.3 ps to 0.8 ps.

With a linearly chirped pulse input centered around 800 nm, the etalon output does not show interference features in the 800 nm spectrum, as shown in Figure 4-15, although the selected oscillation frequency can be clearly seen in the time domain along with some harmonics due to higher-order reflections.

Experiments were conducted to characterize the etalon output, specifically interference stability and modulation quality, through autocorrelation and cross-correlation, as shown in Figure 4-14. In the second harmonic generation (SHG) frequency-resolved optical gating (FROG) experiment, the etalon interference output was sent to have an autocorrelation with itself or a cross-correlation with a transform-limited optical pulse through a second harmonic generation crystal barium borate (BBO). The SHG FROG pattern is a graph of intensity with frequency or wavelength and time as the dimensional parameters, and has the formula: $I_{SHG\ FROG}(\omega, \tau) = |\int_{-\infty}^{\infty} E(t)g(t -$

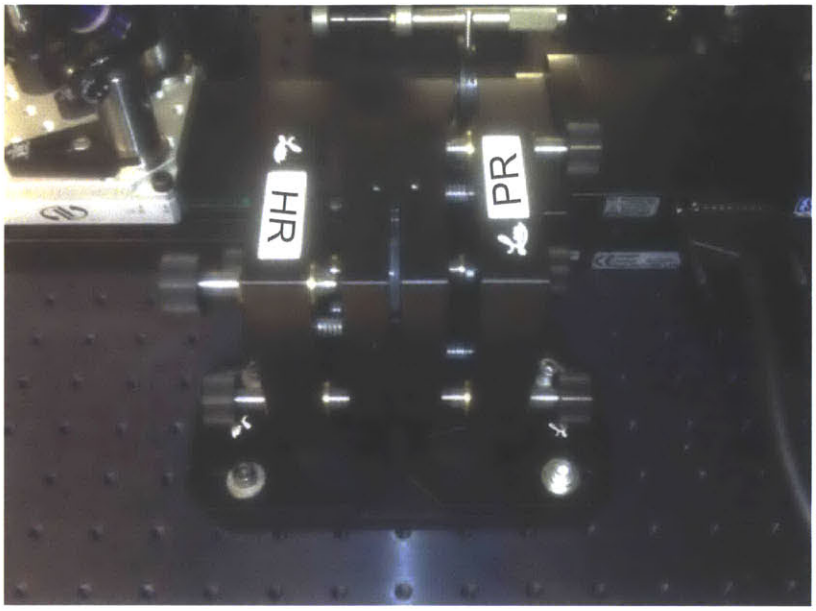

Figure 4-13: An etalon interferometer made by a high reflector (HR) and a partial reflector (PR) at 800 nm. The gap between the HR and PR can be continuously tuned approximately from 50 μm to 100 μm that introduces time delay of 0.3 ps to 0.8 ps.

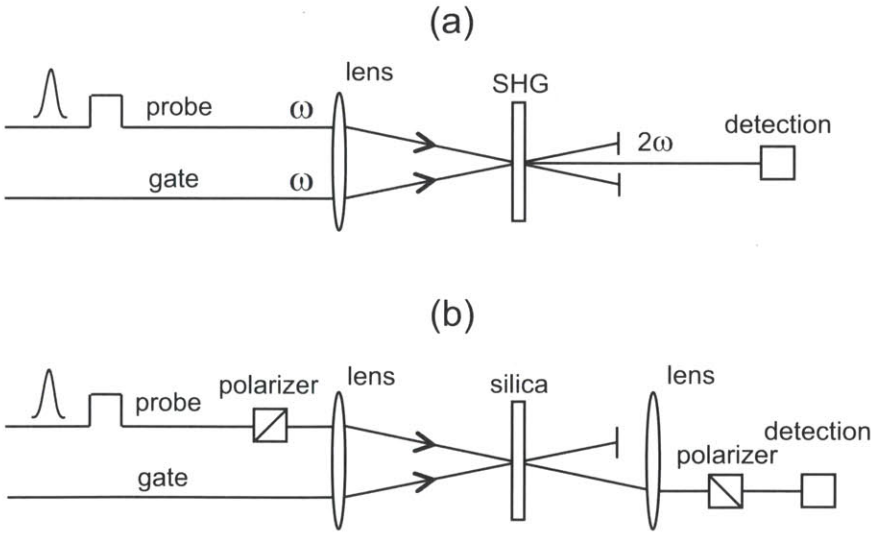

Figure 4-14: An illustration of pulse characterization experiments for (a) SHG measurement in which the detector can be a spectrometer for frequency-resolved optical gating measurement, and (b) polarization gating (PG) cross-correlation measurement where balanced detection can be integrated.

$\tau)e^{-i\omega t}\,\mathrm{d}t|^2$, where $g(t-\tau)$ is the gate pulse temporal profile [111]. The calculated SHG FROG autocorrelation pattern of the chirp-and-delay optical modulation can be found in Figure 4-15, where there is the integrated intensity along time, frequency, or wavelength. Note that the intensity modulation depth is approximately 70% in SHG autocorrelations.

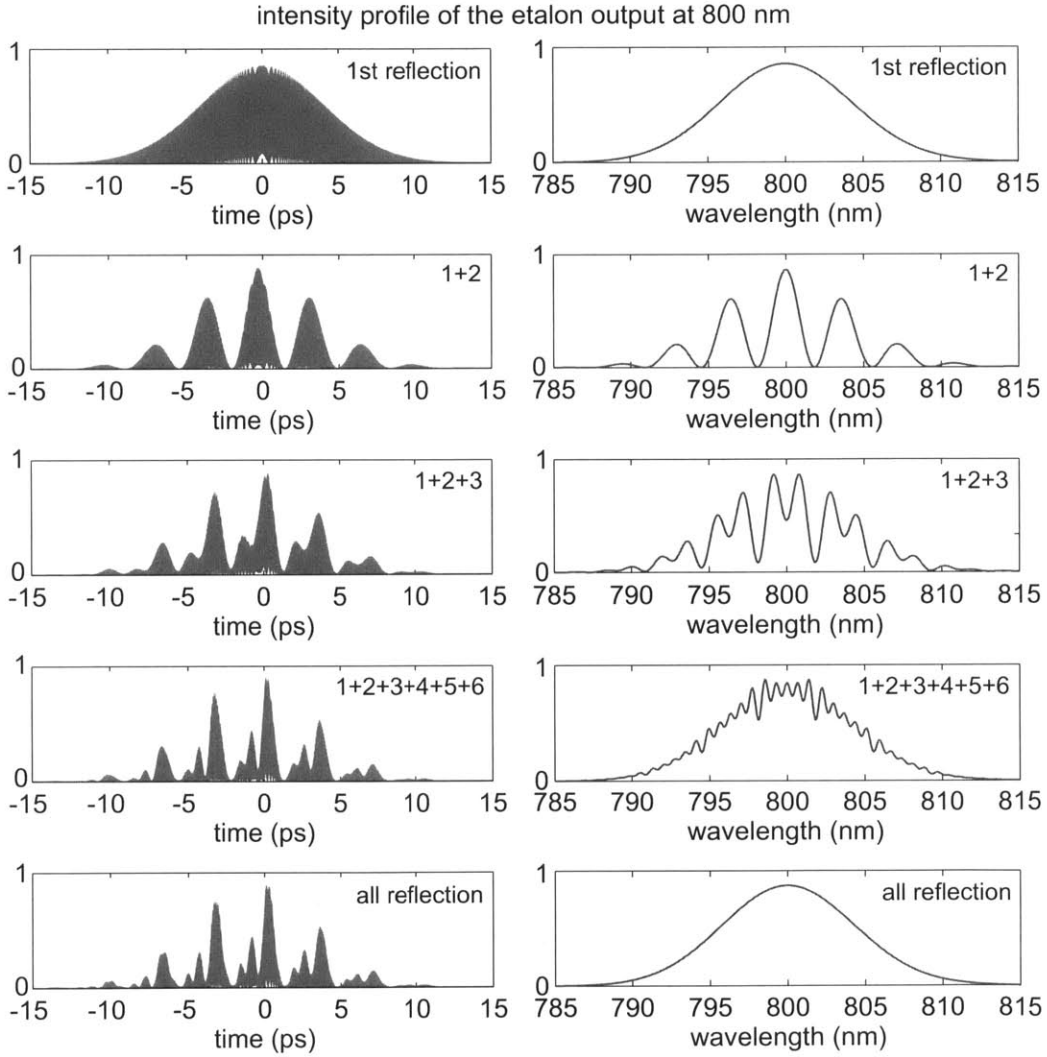

Figure 4-15: Calculated etalon interference intensity profiles with linearly chirped pulses at 800 nm as the input and additions from higher reflection orders. This confirms that the total output does not show interference features in the 800 nm spectrum and the time domain has clear selected oscillation frequency features as well as some harmonics due to superpositions of multiple reflections from the etalon.

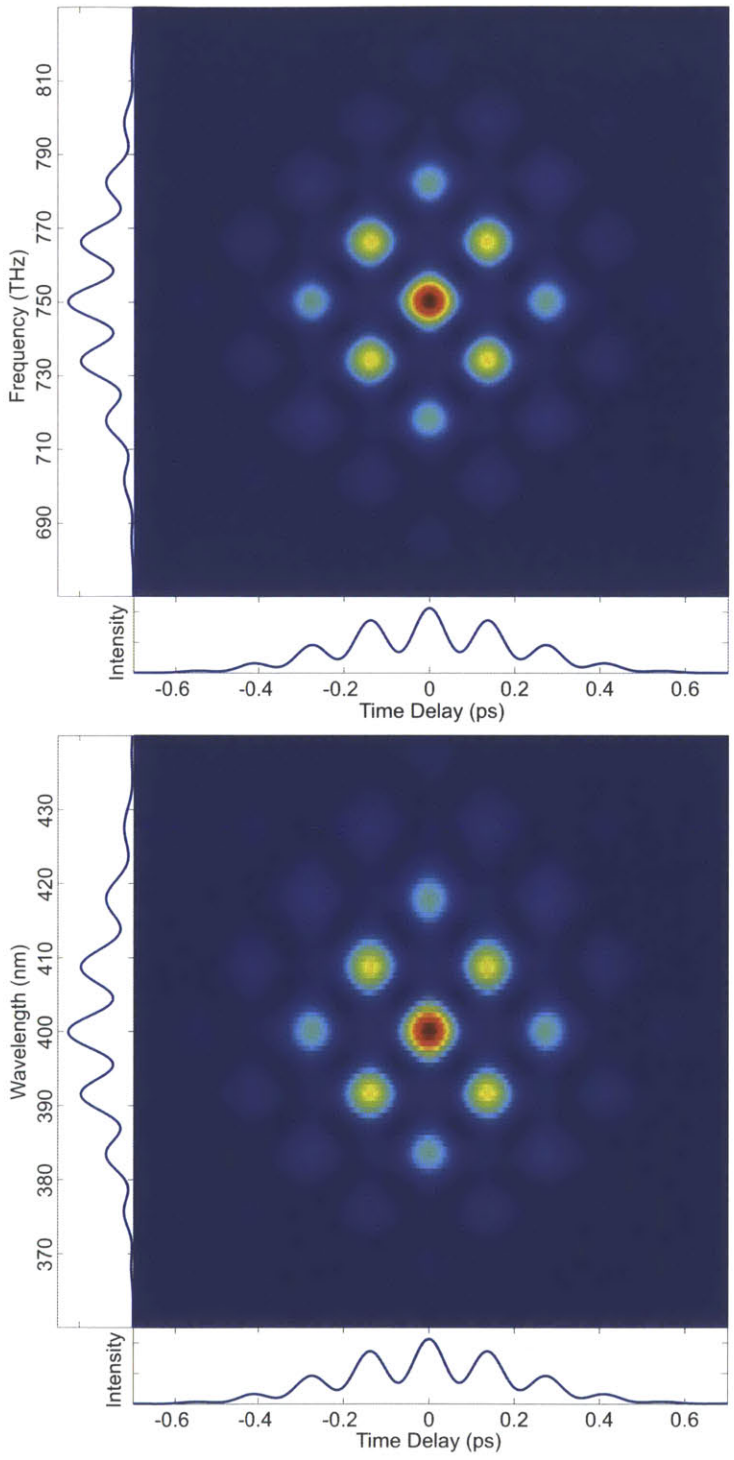

Figure 4-16: Calculated SHG FROG pattern of typical chirp-and-delay optical modulation, and the integrated intensity along time, frequency, or wavelength. Note that the intensity modulation depth is theoretically about 70% in SHG autocorrelations.

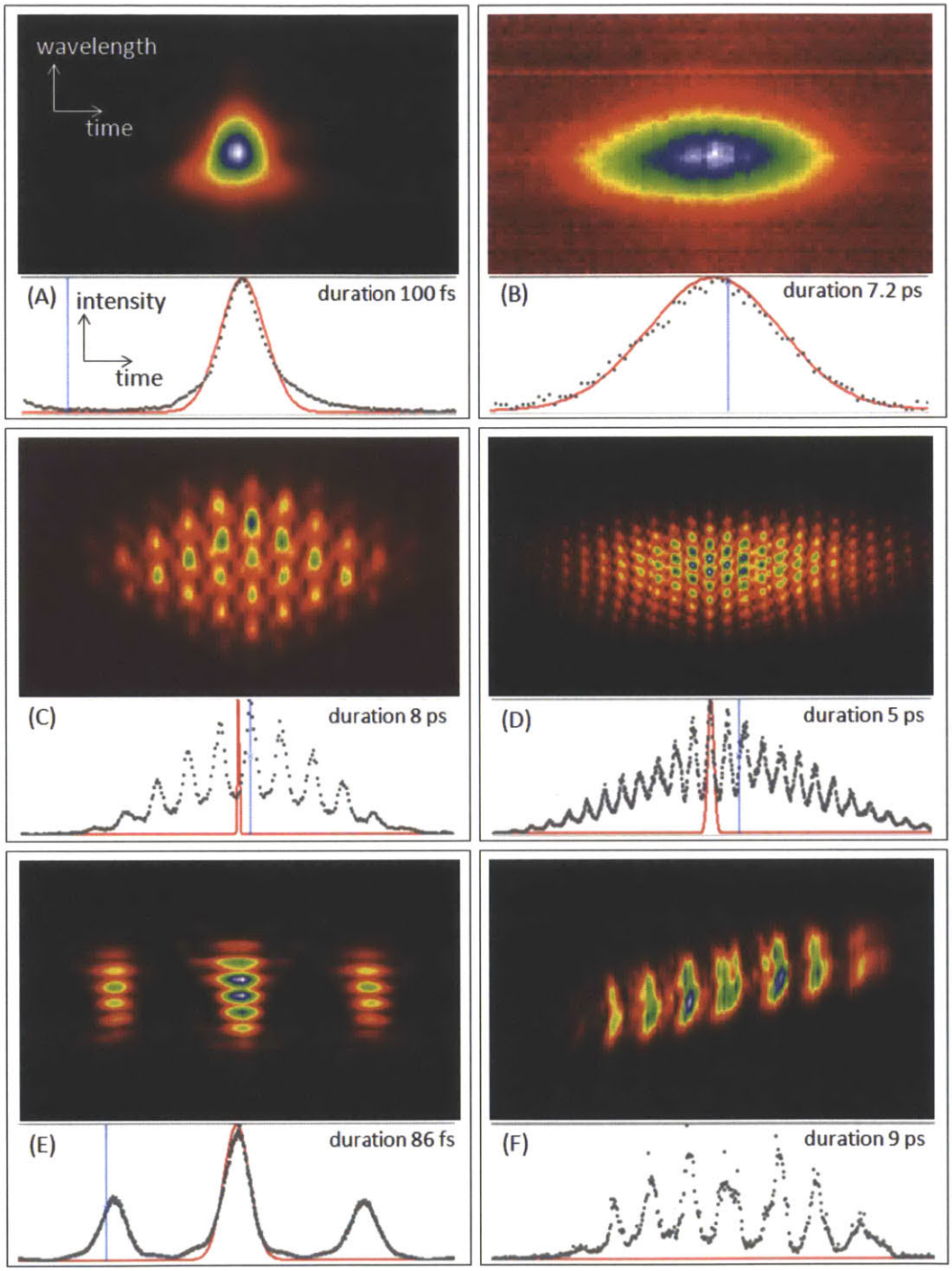

Figure 4-17: Experimental SHG FROG pattern of (a) a transform-limited optical pulse with a duration of 100 fs, (b) a linearly chirped optical pulse with a duration of 7.2 ps, (c) a typical etalon interference with a center frequency at approximately 0.5 THz, (d) a typical etalon interference with a center frequency at approximately 1.5 THz, and (e) the etalon output with transform-limited optical pulse as the input. In (f), the etalon interference was sent to have a SHG cross-correlation with a transform-limited optical pulse. The temporal optical modulation and linear frequency sweep can be clearly seen.

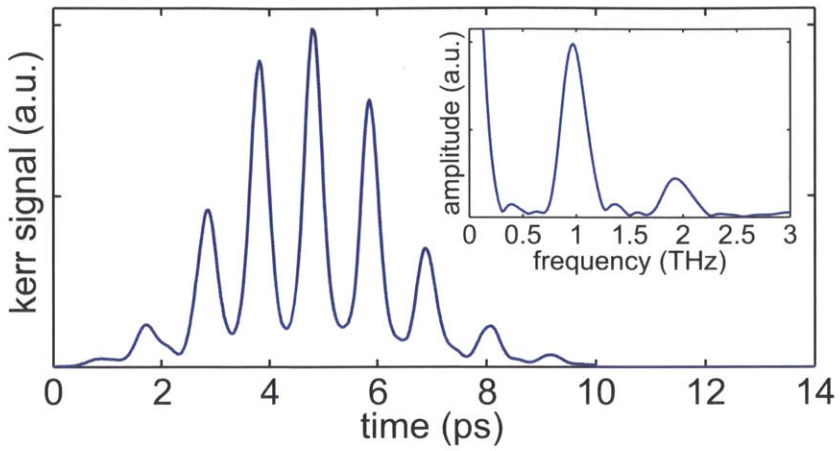

Figure 4-18: A third-order cross-correlation measurement between the chirp-and-delay etalon output and a transform-limited readout pulse through the optical Kerr effect in silica glass. The Fourier spectrum of the intensity modulations is shown in the inset.

Figure 4-17 shows the experimental SHG FROG patterns of transform-limited optical pulses, linearly chirped optical pulses, typical etalon interferences with center frequencies at about 0.5 THz and 1.5 THz, and typical etalon responses with transform-limited optical pulses as the input. The etalon interference was also sent to an SHG cross-correlation with a transform-limited optical pulse, and the temporal optical modulation and linear frequency sweep can be clearly seen.

A third-order polarization gating cross-correlation between the chirp-and-delayed output and a transform-limited readout pulse was also conducted in silica glass. The probe pulse was polarized at 45^0 and spatially overlapped with the chirp-and-delay shaped pulse that induces a transient birefringence through a fast electronic Kerr effect. The polarization of the probe pulse can be rotated by the induced birefringence, which is in phase with the intensity modulation of the pump pulse, and the rotation can be detected by balanced photodiodes. The Kerr signal can be expressed as $S_{PG}(\omega,\tau) = |\int_{-\infty}^{\infty} E(t)|\, g(t-\tau)|^{\,2} e^{-i\omega t}\, \mathrm{d}t|^2$, where $g(g-\tau)$ is the gate pulse temporal profile [111]. One of the measured traces is shown in Figure 4-18, and the Fourier transform (Figure 4-18 inset) reveals some second harmonic of the selected difference frequency due to the superposition of multiple reflections in the etalon.

4.5 Generation of tunable multicycle THz pulses

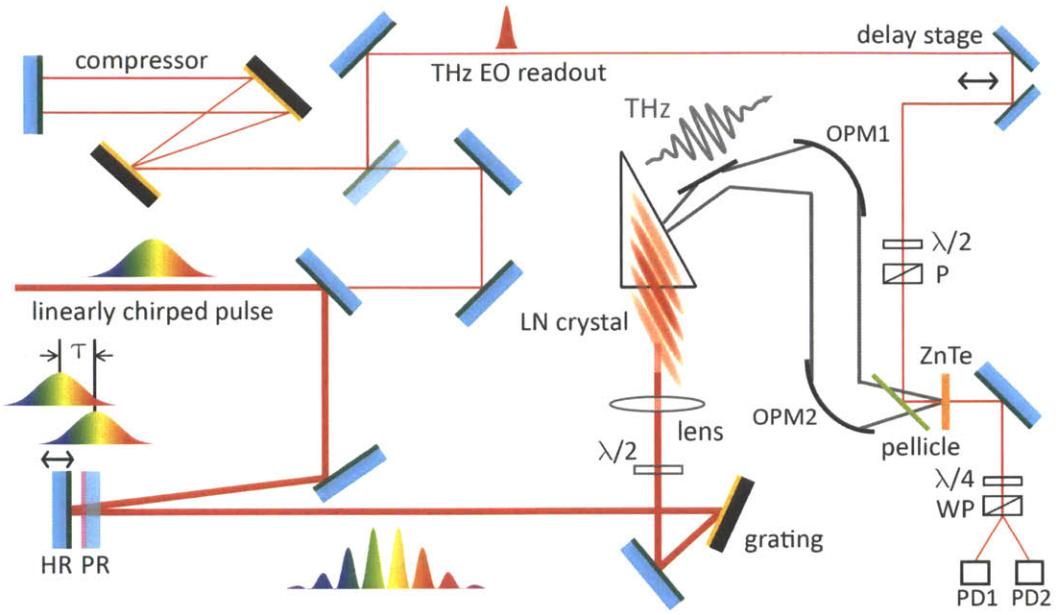

Figure 4-19: Illustration of the experimental setup for generation of high-energy multiple-cycle THz pulses. Linearly chirped pulses were spatially overlapped with a varied time delay τ through a Gires-Tournois etalon, and the intensity front was tilted through a grating-lens combination. A transform-limited readout pulse was used to measure the THz field profile through electro-optic sampling and also to measure the chirp-and-delay optical waveform through cross-correlation. $\lambda/2$, half waveplate; $\lambda/4$, quarter waveplate; P, polarizer; OPM, off-axis parabolic mirror; PD, photodiode; WP, Wollaston prism.

Well-defined multicycle terahertz pulses can be excited inside ferroelectric crystals by optical waveforms that are shaped spatially [38], temporally [116], or both [73, 37]. Optical pulse shaping with a programmable liquid crystal modulator (LCM) has been demonstrated to produce shaped THz pulses in conjunction with difference-frequency generation in ZnTe, including chirped pulses, zero-area pulses, and pulse sequences that are tunable up to 2.0 THz [2]. Tilted intensity front technique has also been implemented to select the THz phase velocity in a narrow frequency region in a bulk $LiNbO_3$ crystal [53] and in a waveguide geometry [77]. Temporal pulse shaping combined with spatiotemporally shaping with a tilted intensity front has been demonstrated to generate a multiple-pulse optical waveform [133]. Although the temporal shaping was not very versatile, this approach should allow for generation of high-energy multiple-cycle THz pulses for certain configurations.

In these approaches each cycle of the multiple-cycle THz field is not continually pumped by the optical pulse or pulse sequences, so the generation process is not optimized for high-energy THz pulses. Noncollinear velocity matching was made possible through the tilted intensity front technique, where THz waves are continuously amplified while traveling with the optical pump pulses in a crystal with large nonlinear coefficients. The THz waveform was near-single-cycle because many frequency components were phase matched together as set by the angle of the intensity front tilt. As shown qualitatively in Figure 4-1, generation of high-energy multiple-cycle terahertz pulses can be realized along with the temporal shaping method presented in the previous section.

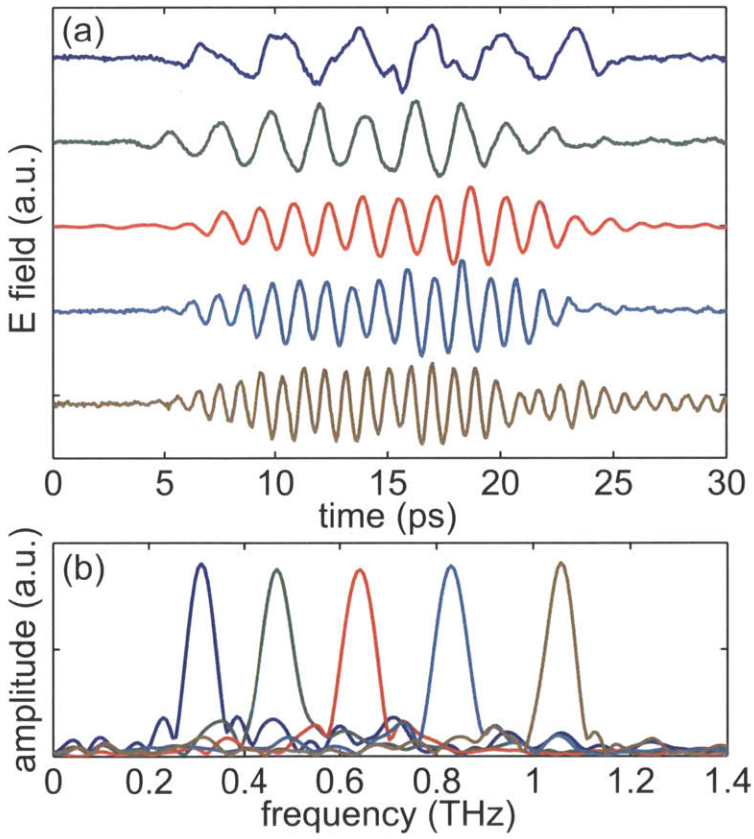

Figure 4-20: Experimental results of (a) THz field traces and (b) normalized Fourier spectra, generated with a 6 mJ near-infrared chirp-and-delay tilted intensity front waveform at 1 kHz repetition rate.

The experimental setup is illustrated in Figure 4-19. Near-infrared optical pulses

with 6 mJ energy at 1 kHz repetition rate were produced from a commercial Ti:sapphire amplifier system, and the compressor grating spacing was reduced to generate positively chirped pulses with durations around 10 ps. A 1% beam splitter was used to split off the THz readout pulse which was subsequently recompressed to the transform-limit by a separate compressor. The Gires-Tournois etalon made by a partial reflector (38% reflection efficiency) and a high reflector was used to introduce the variable time delay between chirped pulses.

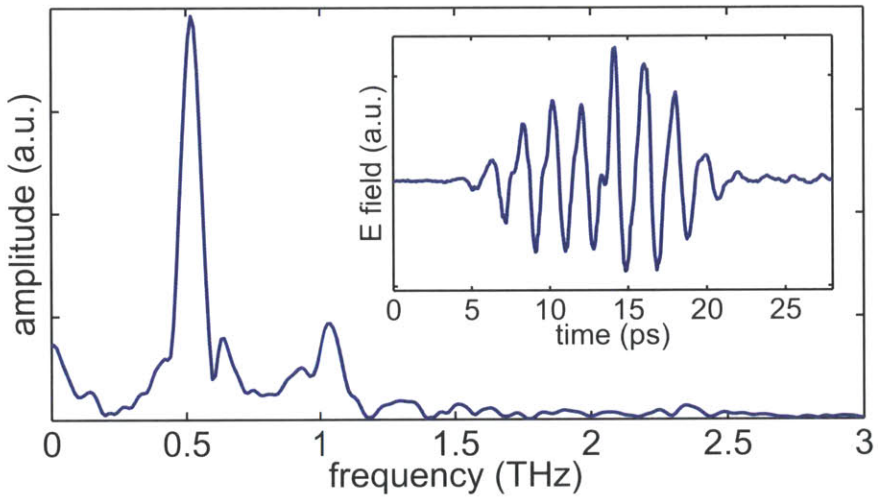

Figure 4-21: A THz field trace measured by electro-optic sampling and the normalized Fourier spectrum, generated with a 35 mJ near-infrared chirp-and-delay tilted intensity front waveform at 10 Hz repetition rate.

The chirp-and-delayed waveform was sent to a similar tilted intensity front setup as previously described [132]. A 2000 line/mm grating was used to achieve the appropriate intensity front tilt in the -1 diffraction order, and a single 80 mm focal length spherical lens was used to image the grating surface onto the LN crystal. The beam was about 10 mm in diameter at the grating and 5 mm in diameter at the LN surface. Approximately 2/3 of the optical pulse energy reached the LN crystal. The input surface of the LN crystal was AR coated for 800 nm, and the crystal was specially shaped in order to couple the THz phonon-polariton wave at a normal incidence into air. THz radiation was directed and focused by two off-axis parabolic mirrors

into a ZnTe crystal for electro-optic sampling measurement, or into a Microtech pyroelectric detector for pulse energy measurement.

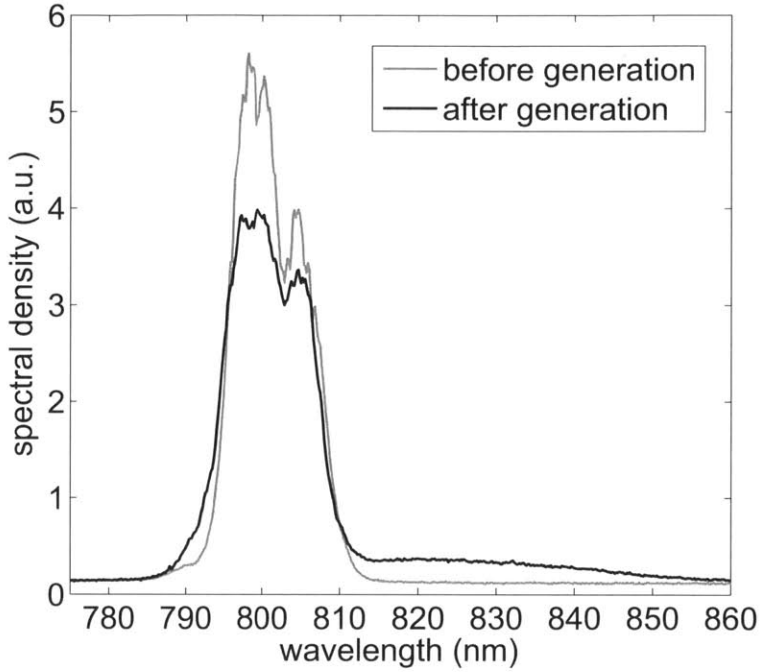

Figure 4-22: Optical spectra before and after LN crystal in multicycle THz generation pumped with 35 mJ intensity-front-tilted quasi-sinusoidal optical waveform. The lobes on the long wavelength part from 810 to 860 nm after LN crystal indicates high optical-to-THz conversion efficiency due to high-energy THz generation.

With 6 mJ near-infrared optical pulses at 1 kHz repetition rate, multicycle THz pulses were generated with energies up to 1.5 μJ. The THz center frequencies were tuned through adjustment of the etalon mirror separation, and at each separation, the THz output was optimized through adjustment of the intensity front tilt angle to optimize velocity matching for the selected THz frequency. The adjustments were small because the phonon-polariton dispersion curve in this frequency range is nearly linear in LN. The THz frequency tuning range was between 0.3 and 1.3 THz, and the bandwidth of the pulses were generally less than 0.1 THz. Figure 4-20 shows THz waveforms throughout this tuning range. A comparison between the optical intensity modulation frequencies measured through cross-correlation as in Figure 4-18 and the THz frequencies measured through electro-optic sampling as in Figure 4-20 showed

good agreement.

Some experiments were conducted with a 10 Hz, 35 mJ optical pump pulse through the same chirp-and-delay and tilted intensity front setup for the generation of high-energy multiple-cycle THz pulses. Figure 4-21 shows the resulting waveform and Fourier spectrum of a multiple-cycle THz pulse centered at 0.50 THz. The THz output had over 10 μJ energy. The phase change in the field trace and the dip in the corresponding Fourier spectrum around 0.56 THz are due to the absorption of water vapor. Optical spectra of pump pulses were also measured before and after the LN crystal, as shown in Figure 4-22, and the lobes on the long wavelength part from 810 to 860 nm after LN crystal indicates a high optical-to-THz conversion efficiency due to high-energy THz generation.

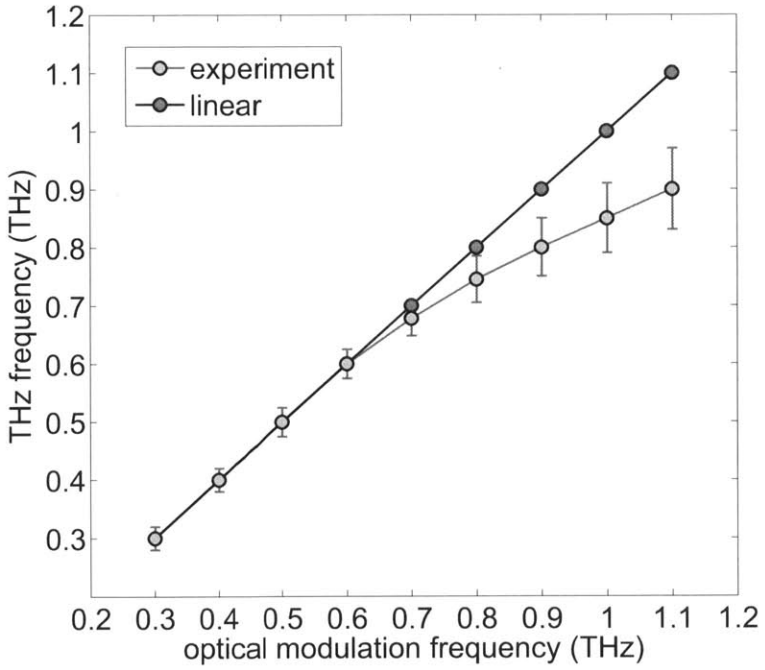

Figure 4-23: An illustration of the correspondence between the optical modulation frequency and the THz center frequency at 1 kHz repetition rate. In the relatively high frequency region from 0.9 to 1.3 THz, up to 20% difference can be observed. This may be due to a small but significant amount of chirp among the diffracted frequency components near the image plane.

These results represent an extension of spatiotemporal shaping of the optical field from a particularly simple form (a single pulse that undergoes a linear spatial and

temporal sweep at a speed set by the tilted intensity front) to a form that is still relatively simple (a temporally intensity-modulated waveform that undergoes a linear spatial and temporal sweep) and that is well adapted for generation of an important class of THz waveforms - short multiple-cycle pulses with well defined, tunable frequencies - with the high pulse energies and field amplitudes that noncollinear velocity matching in LN can provide. Completely reconfigurable spatiotemporal shaping of the optical field can be employed for generation of arbitrary THz waveforms in LN [36], but the present approach is simpler and supports higher optical pulse energies for generation of intense frequency-tunable THz pulses.

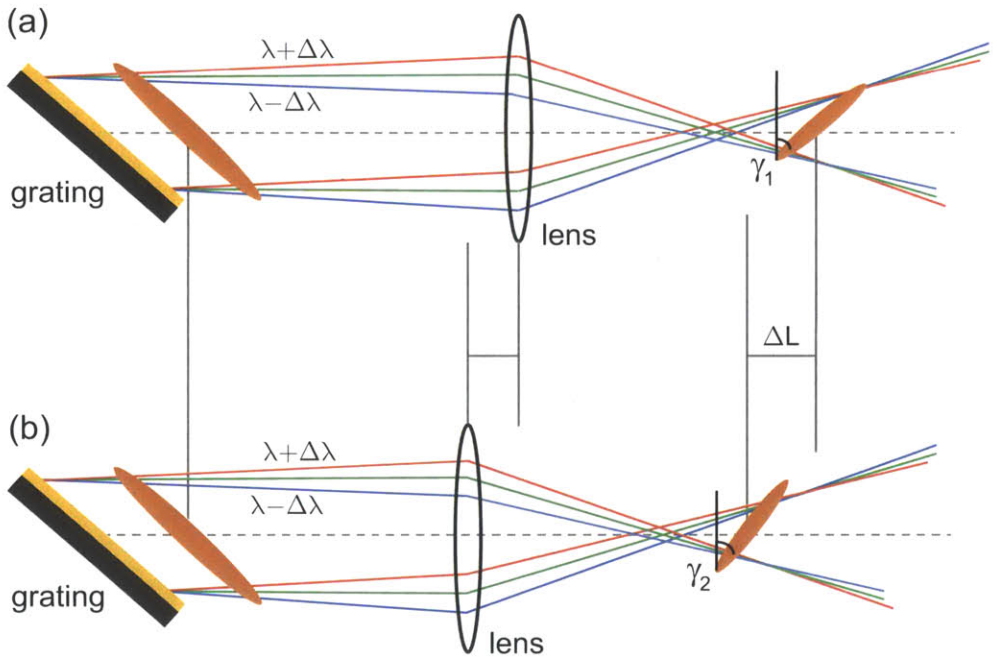

Figure 4-24: The image ratio change for the optimization of (A) lower frequencies and (B) higher frequencies. ΔL was about 10 mm in this experiment, corresponding to a tilt angle change of about 1.8 degree. The imaging ratio in (b) was larger and the tilt angle was smaller.

We believe higher THz pulse energies are possible. The horizontal spot sizes of the tilted intensity front waveforms should be optimized with respect to THz attenuation in LN, which is frequency-dependent. In our measurements the spot size was kept constant. Cooling of the LN to reduce attenuation can also be beneficial [53]. Finally, the frequency range can be extended through improved optical modulation depth and

through cooling of the LN crystal.

The experimental correspondence was measured between the center frequencies of multiple-cycle THz pulses and the quasi-sinusoidal optical intensity modulation before its intensity front was tilted by the grating-lens system. The center frequency of the optical intensity modulation can be measured by the previously detailed method of auto-correlation or cross-correlation in a nonlinear second- or third-order process, while the center frequency of the multiple-cycle THz pulses can be measured by electro-optic sampling. As illustrated in Figure 4-23, general consistency was found over the entire frequency tuning range, confirming that THz oscillations originate from the optical intensity modulation.

For energy optimization of lower and higher THz center frequencies, the imaging ratio of the single-lens imaging system needs to be changed until the tilt angle is larger in the higher frequency case to match the smaller THz phase velocity. The ΔL in our experiment was about 10 mm, corresponding to a tilt angle change of about 1.8 degree as illustrated in Figure 4-24. The tilt angle is very sensitive to the imaging ratio change, for example in part (b) of the Figure 4-24, the imaging ratio was larger (about 0.55), and the tilt angle was smaller (about 61.2 degrees).

We note that for each chirp-and-delay setting of the optical modulation frequency, adjustment of the imaging system to optimize the THz output energy caused a significant change in the THz frequency, up to 20% at frequency range 0.9 - 1.3 THz. From the optimization geometry, it can be concluded that this effect is not due to the small Cherenkov angle change for different frequencies because the angle for higher frequencies is larger. However in this experiment, the angle for the optimization of higher frequencies is actually smaller. We believe that this may be due to a small but significant amount of chirp among the diffracted frequency components in the tilted intensity front near the image plane, as has been previously reported [56, 83]. As illustrated in Figure 4-25, this would effectively change the chirp-and-delay parameters and therefore the optical modulation frequency to a somewhat different value and the THz center frequencies. Further experiments can be performed by measuring the change in frequency with variable input pump pulse energies.

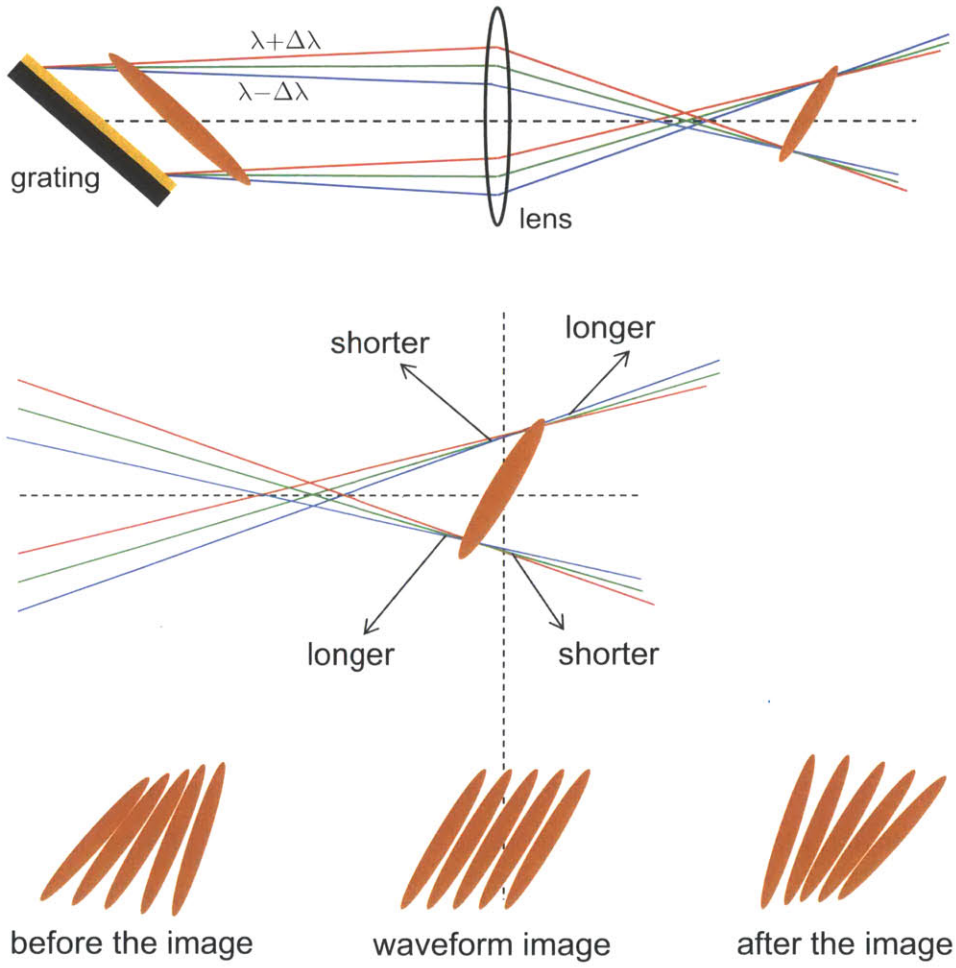

Figure 4-25: An image of the moving grating pattern through a single-lens system and the influence of chirp sign change on the pulse duration of the quasi-sinusoidal intensity-modulated optical waveform.

4.6 Spatiotemporal optical pulse sequences

In the case of generation of high-power near-single-cycle THz pulses, velocity matching can be implemented through a continuous tilted optical intensity front with either a diffraction grating or spatiotemporally displaced pulse sequences [134] with a stack of glass pieces that introduce time delays at variable spatial locations, as illustrated in Figure 4-26. One of the advantages of this process is that the amount of optical dispersion in the generation crystal is very small and arises from the lens imaging system, and it can be further improved upon with various methods. A few calculated results of generated multicycle THz pulses, electric field traces, and their corresponding Fourier spectra are shown in Figures 4-26, 4-27 and 4-28. Here the individual pulse spot size is fixed, center frequencies are tuned through temporal shaping, and optical pump pulses have the same pulse energies. The THz frequency components set by individual pulse spot size in the lateral direction can be seen through the THz single-cycle Fourier spectrum in Figure 4-28. This determines the tuning region and general trend of spectral amplitudes of the frequency-tunable multicycle THz pulses generated by temporal shaping.

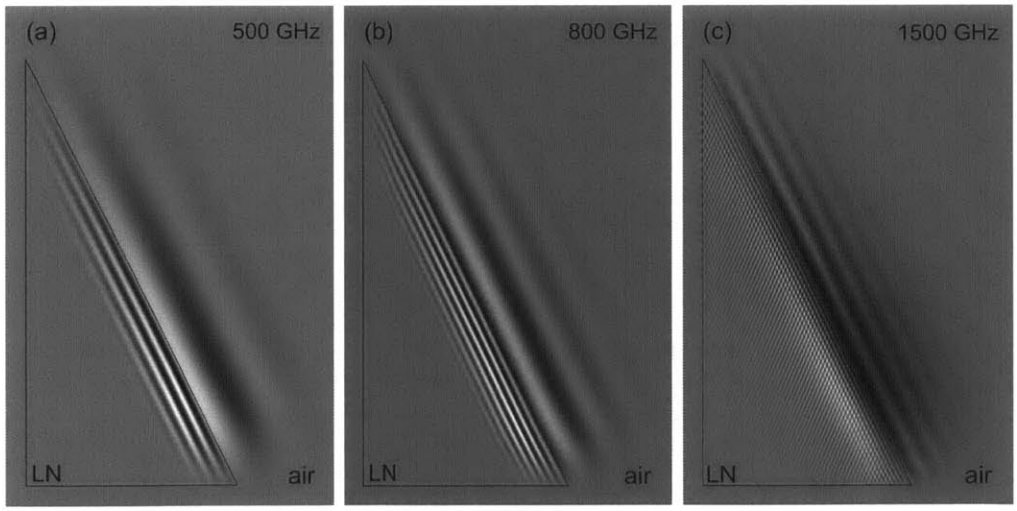

Figure 4-26: Generation of multicycle terahertz pulses in a $LiNbO_3$ crystal by spatiotemporally displaced pulse sequences where the individual pulse spot size is fixed and the center frequencies are tuned through temporal shaping. The electric field patterns with center frequencies at 500 GHz, 800 GHz, and 1500 GHz are illustrated respectively.

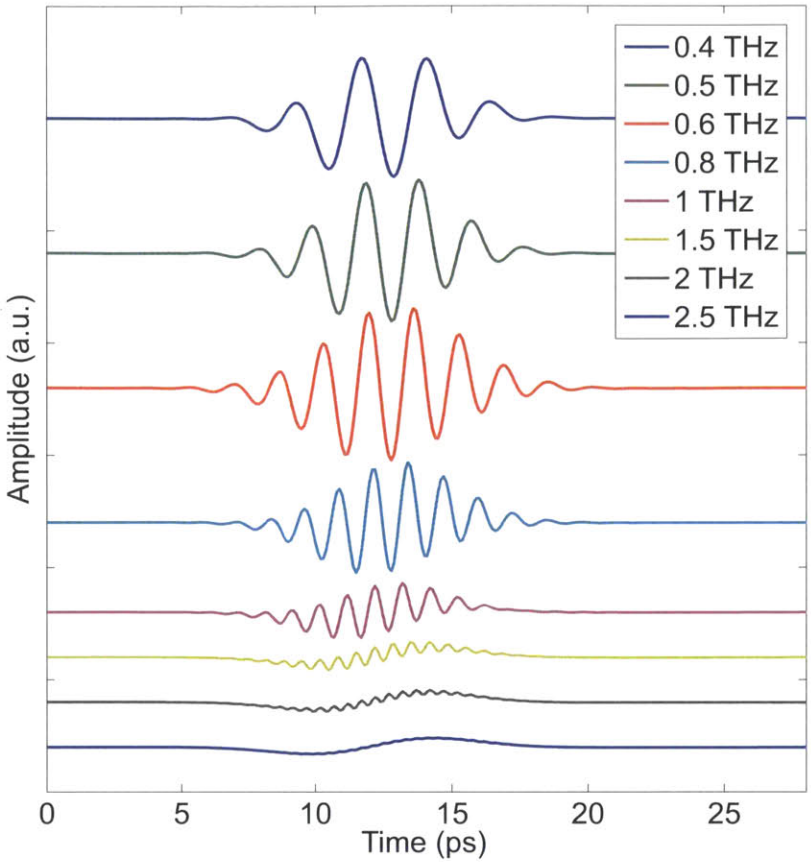

Figure 4-27: THz electric field traces of multicycle THz pulses generated with spatiotemporally displaced optical pulse sequences. The frequency components are set by the individual pulse spot size, and the center frequencies are tuned through temporal shaping.

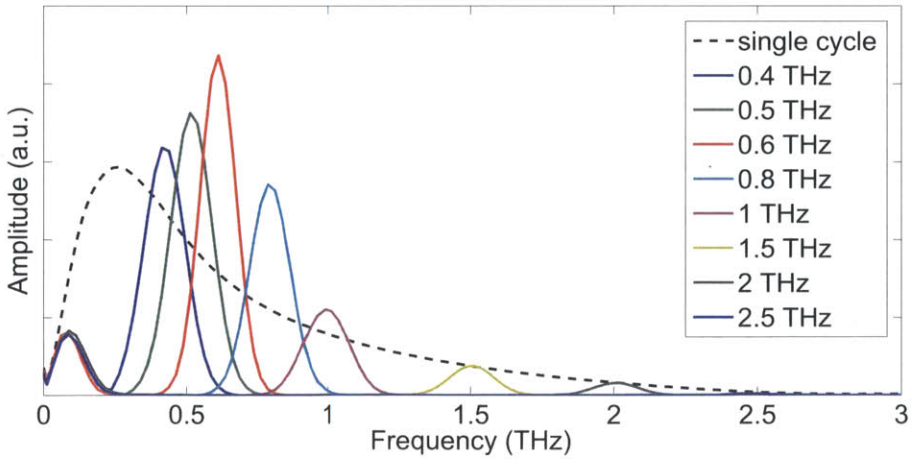

Figure 4-28: The corresponding Fourier spectra of multicycle terahertz pulses generated with spatiotemporally displaced optical pulse sequences. The frequency components are set by the individual pulse spot size, and the center frequencies are tuned through temporal shaping.

Chapter 5

Nonlinear Terahertz Phenomena in a Ferroelectric Crystal

This work is in collaboration with Dr. Xibin Zhou, Dr. Christopher A. Werley, and Dr. Harold Y. Hwang of the Massachusetts Institute of Technology.

Nonlinear phenomena in optical frequencies have been studied for many years and have important scientific and technological applications, including frequency mixing, parametric amplification, and the electro-optic effect where the response function is primarily given by electronic processes. In the far-infrared region where many phonon resonances and electron-phonon coupling exist, ionic motions contribute both linearly and nonlinearly to the dielectric function. The frequency region of terahertz (THz) phonon-polaritons is below the lowest transverse optic phonon mode, and THz generation and propagation are strongly coupled with lattice vibrations. Nonlinear phenomena relevant to sufficiently high-intensity THz waves would be interesting because the processes involve ionic motions that are intrinsically linked to properties of physical materials. More generally, the generation and application of high-power THz pulses [62, 132] has facilitated the observation of many nonlinear THz phenomena in solids, liquids, and gases [60, 39, 72]. In this chapter, general considerations of nonlinear optics in the far-infrared region are briefly introduced, followed by the nonlinear phenomena through THz generation in bulk ferroelectric crystals $LiTaO_3$

and $LiNbO_3$. Simulations of THz electric fields and lattice vibrations as well as some experimental results are also presented.

5.1 Nonlinear optics in the THz region

Nonlinear optics is generally related to phenomena resulting from the modification of optical properties in the presence of a strong electric field. The system response depends on the field strength, and the coefficients that determine how strongly the system responds are intrinsic properties of the material. For example, in condensed phase systems a nonlinear electronic response is usually very fast since its characteristic time is a few femtoseconds. A nuclear response in these systems is relatively slower, on the order of $0.1 - 10$ picoseconds for optical phonon modes.

Nonlinear phenomena can be described in the time domain by response functions and in the frequency domain by susceptibilities. The constitutive relations are in tensor form and can be written as,

$$D(\omega) = \epsilon_0 E(\omega) + P(\omega) = \epsilon_0 E(\omega) + \epsilon_0 \chi^{(1)}(\omega) E(\omega) + P_{NL}(\omega) \tag{5.1}$$

where ϵ_0 is the permittivity in vacuum. The nonlinear polarization P_{NL} is given by:

$$P_{NL}(\omega) = \epsilon_0 (\chi^{(2)}(\omega) E(\omega)^2 + \chi^{(3)}(\omega) E(\omega)^3 + \cdots + \chi^{(n)}(\omega) E(\omega)^n + \cdots) \tag{5.2}$$

where $\chi^{(i)}(\omega)$ are the nonlinear susceptibilities. $\chi^{(1)}(\omega)$ is the linear susceptibility, and its real and imaginary part are frequency-dependent, and relevant to the material's index of refraction and absorption.

In the far-infrared region that is close to ionic resonances, both the electronic and lattice system contribute to polarizations. Similar to the optical frequency region, nonlinear susceptibilities are closely related to linear susceptibilities [81] when perturbations of the electronic oscillator are considered. The ionic contributions can be

included by the equation:

$$\chi^{(n)}(\omega) = \chi^{(n)}_{electronic}(\omega) + \chi^{(n)}_{ionic}(\omega) \tag{5.3}$$

where the nonresonant electronic or high-frequency part is closely related to polarizability. This part can be treated as either a constant or a function of nuclear displacement, depending on the specific process. The ionic part can be modeled as either driven single or multiple Lorentz oscillators. In a typical process of the far-infrared region such as the phonon-polariton mode, susceptibilities can be expressed as,

$$\varepsilon_r(\omega) = \varepsilon_\infty + \frac{\omega_{\mathrm{TO}}^2(\varepsilon_0 - \varepsilon_\infty)}{\omega_{\mathrm{TO}}^2 - \omega^2 - i\omega\Gamma} = 1 + \chi^{(1)} \tag{5.4}$$

$$\chi^{(1)}_{electronic} = \varepsilon_\infty - 1, \quad \chi^{(1)}_{ionic} = \frac{\omega_{\mathrm{TO}}^2(\varepsilon_0 - \varepsilon_\infty)}{\omega_{\mathrm{TO}}^2 - \omega^2 - i\omega\Gamma} \tag{5.5}$$

where ω_{TO} is the resonance frequency, and Γ is the phenomenological damping term. As an example, the second-order nonlinear susceptibilities have been found to have the following form

$$\chi^{(2)}_{jkl}(\omega_3, \omega_2, \omega_1) = \chi^{(2)}_E \Bigg[1 + C_1\left(\frac{1}{D(\omega_1)} + \frac{1}{D(\omega_2)} + \frac{1}{D(\omega_3)}\right) + C_2\left(\frac{1}{D(\omega_1)D(\omega_2)} + \frac{1}{D(\omega_1)D(\omega_3)} + \frac{1}{D(\omega_2)D(\omega_3)}\right) + C_3\frac{1}{D(\omega_1)D(\omega_2)D(\omega_3)}\Bigg] \tag{5.6}$$

where $D(\omega_i)$ is the linear susceptibility given by

$$D(\omega_i) = 1 - (\omega_i/\omega_{TO})^2 + i\omega_i\Gamma/\omega_{TO}^2 \tag{5.7}$$

$\chi^{(2)}_E$ is the second-order pure electronic nonlinear susceptibility, and the parameters C_1, C_2, and C_3 can be calculated or experimentally measured.

With relatively large vibrational amplitudes of ionic motions, perturbations beyond the harmonic approximation can be included similar to the electronic system

in the optical frequency region. THz phonon-polariton generation and propagation have provided a platform to study coherent lattice waves, which are related to vibrations along the potential energy surface as a function of the normal mode coordinate. Ferroelectric crystals typically have double-well potentials along the soft mode coordinate, and properties of the well shape are presented briefly in the following section with $LiTaO_3$ and $LiNbO_3$ as examples.

5.2 Soft mode potential energy surface

The potential energy surface can be expressed as a function of the net ionic displacement along the ferroelectric soft mode of $LiTaO_3$ and $LiNbO_3$ by the following [67, 97]:

$$V(Q) = -\frac{1}{4}m\omega_{TO}^2 Q^2 + \frac{1}{64|V(Q_0)|}m^2\omega_{TO}^4 Q^4 \tag{5.8}$$

where the displacement can be related to the normal mode coordinate Q_n through the reduced mass M and the oscillator density N as $Q_n = \sqrt{N\sum_i m_i r_i^2} = \sqrt{NM}Q$. With the local potential minima as the origin, the potential surface can be expressed with quadratic, cubic, and quartic terms of the vibrational amplitude

$$V(Q) = V(Q_0) + \frac{1}{2}m\omega_{TO}^2 Q^2 + \gamma Q^3 + \lambda Q^4 \tag{5.9}$$

and the coefficients γ and λ are given by:

$$\gamma = \left(\frac{m^3\omega_{TO}^6}{32|V(Q_0)|}\right)^{1/2}, \quad \lambda = \frac{m^2\omega_{TO}^4}{64|V(Q_0)|} \tag{5.10}$$

Therefore the oscillator restoring force can be expressed in terms of the normal mode coordinate:

$$f = \omega_{TO}^2 Q + aQ^2 + bQ^3 \tag{5.11}$$

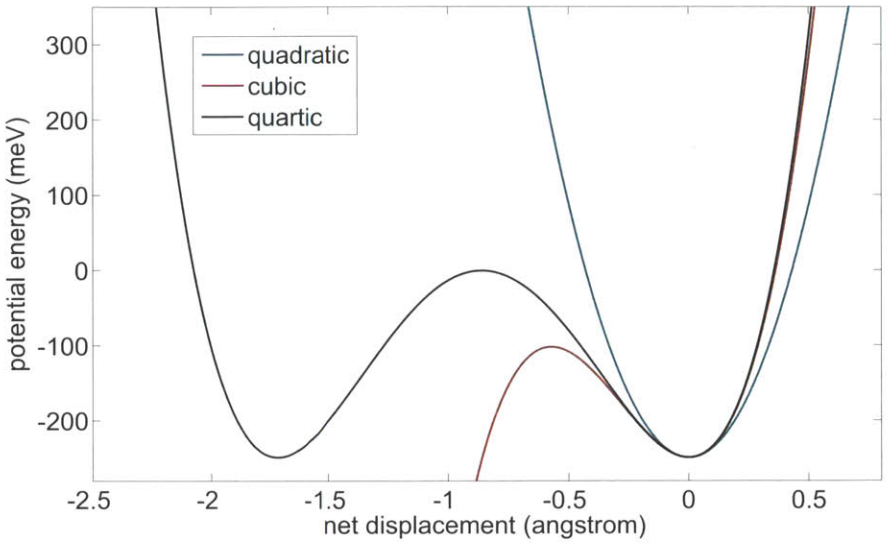

Figure 5-1: The potential energy surface along the ferroelectric soft mode of $LiNbO_3$ where the origin has been set at one of the equilibrium points. The quadratic, cubic, and quartic approximations of small vibrational amplitudes around the origin have been included.

and the coefficients a and b are

$$a = \frac{3\ \omega_{TO}^3 \sqrt{M}}{4\sqrt{2|V(Q_0)|}}, \qquad b = \frac{m\ \omega_{TO}^4}{16|V(Q_0)|} \tag{5.12}$$

The potential energy surface of the ground electronic state along the ferroelectric soft mode of $LiNbO_3$ is shown in Figure 5-1 and Figure 5-2, along with quadratic, cubic, and quartic approximations of small vibrational amplitudes. The resulting oscillator restoring force is shown in Figure 5-3. The potential wells of $LiNbO_3$ and $LiTaO_3$ primarily come from joint displacements of oxygen and lithium ions, and the well depths at room temperature are 248.88 meV (2858 K) and 235.28 meV (2739 K) respectively [67], which are very deep and correspond to the spontaneous polarization. Harmonic approximations work well for small vibrational amplitudes, and the cubic term can be a good approximation for a relatively wide region around the equilibrium point.

The potential well shapes and depths can be different across many types of ferroelectric crystals. The transition temperature T_c from paraelectric to ferroelectric phase varies, and there are order-disorder, displacive, or mixed transitions types. Even

in the ferroelectric phase, well shape and depth change as a function of temperature, a result of the softening or hardening of the transverse optical phonon resonance ω_{TO}.

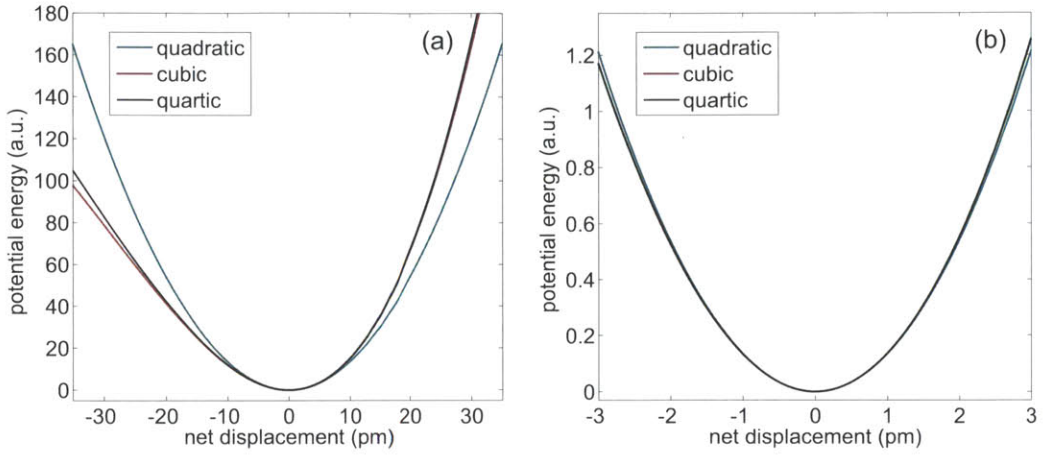

Figure 5-2: The potential energy surface along the ferroelectric soft mode of $LiNbO_3$ for small vibrations around the equilibrium point. The quadratic, cubic, and quartic approximations have been included.

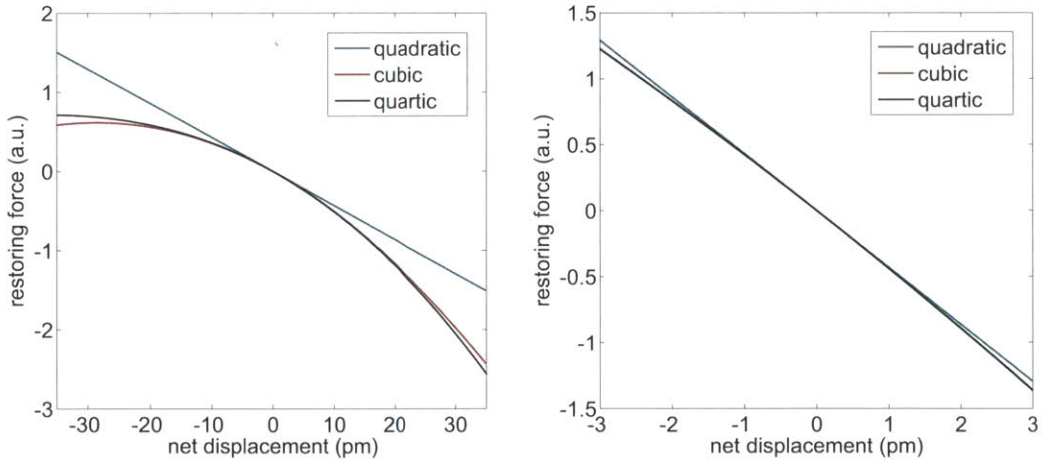

Figure 5-3: The lattice oscillator restoring force along the ferroelectric soft mode of $LiNbO_3$ for small vibrations around the equilibrium point. The quadratic, cubic, and quartic approximations have been included.

For lattice vibrations at low temperature, the phenomenological damping term Γ usually decreases significantly, giving a narrower and stronger absorption peak of the dielectric function. The dielectric function in the low-frequency limit ε_0 also changes with temperature. Although not directly related to the potential well surface, these

parameters can influence lattice vibrations, linear and nonlinear susceptibilities of the crystal, and the index of refraction.

5.3 Sources of nonlinearity in THz generation

In the far-infrared regions of ferroelectric systems, the electronic and ionic parts contribute to the polarization response as follows

$$\ddot{\vec{Q}} = b_{11}\vec{Q} + b_{12}\vec{E} \tag{5.13}$$

$$\vec{P} = b_{21}\vec{Q} + b_{22}\vec{E} \tag{5.14}$$

where b_{11} and $b_{21} = b_{12} = \omega_{\mathrm{TO}}\sqrt{\epsilon_0(\varepsilon_0 - \varepsilon_\infty)}$ are related to the contribution of ionic vibrations, and $b_{22} = \epsilon_0(\varepsilon_\infty - 1)$ is mostly an electronic contribution that is closely related to polarizability.

Generation of THz phonon-polaritons through nonresonant impulsive stimulated Raman scattering process is modeled with the anharmonic potential surface approximated by the cubic and quartic term as in Equation (5.11), resulting in the following,

$$\begin{cases} \ddot{\vec{Q}} + \Gamma(\vec{Q})\cdot\dot{\vec{Q}} + \omega_{\mathrm{TO}}^2\cdot\vec{Q} + a\cdot\vec{Q}^2 + b\cdot\vec{Q}^3 = b_{12}\vec{E} + \frac{1}{2}\epsilon_0\sqrt{\frac{N}{M}}(\frac{\partial\alpha}{\partial\vec{w}})I_{pump} \\ (\nabla^2\vec{A} - \varepsilon_\infty(\vec{Q})\cdot\ddot{\vec{A}}/c_0^2) = -\mu_0\omega_{\mathrm{TO}}\sqrt{\epsilon_0(\varepsilon_0 - \varepsilon_\infty)}\dot{\vec{Q}} \end{cases} \tag{5.15}$$

There are many types of nonlinearity in this process, among which the nonlinearity of the restoring force, the differential polarizability, and the damping term are three major contributors as in the following expressions:

$$b_{11}(Q) = b^{(0)} + b^{(1)}(Q_1 + Q_2 + Q_3 + \cdots) + b^{(2)}(Q_1 + Q_2 + Q_3 + \cdots)^2 + \cdots \tag{5.16}$$

$$\varepsilon_\infty(Q) = \varepsilon^{(0)} + \varepsilon^{(1)}(Q_1 + Q_2 + Q_3 + \cdots) + \varepsilon^{(2)}(Q_1 + Q_2 + Q_3 + \cdots)^2 + \cdots \tag{5.17}$$

$$\Gamma(Q) = \Gamma^{(0)} + \Gamma^{(1)}(Q_1 + Q_2 + Q_3 + \cdots) + \Gamma^{(2)}(Q_1 + Q_2 + Q_3 + \cdots)^2 + \cdots \tag{5.18}$$

where some terms vanish in certain types of crystals due to symmetry considerations, and $Q_n = Q^{(n)}e^{in(kx-wt)}$ represent the n_{th} order expansion of lattice displacement har-

monics, also termed the wavevector and frequency overtones in previous observations of lattice anharmonicity.

In the sources of nonlinearity, every wavevector or frequency overtone of the lattice displacements Q_n can probe a contribution arising from the same order of nonlinear anharmonic part, either from the restoring force, the differential polarizability, or the damping term. Any one type of the anharmonic order can give rise to multiple harmonic components of lattice vibrations and electric fields [97]. This may result in several questions such as where the coherent nonlinearity comes from, how it is generated, and how far it can propagate.

For lattice dynamics in ferroelectric systems generated through nonresonant excitation with near-infrared ultrashort laser pulses, the three aforementioned types of nonlinearity can be set forth in parallel in the generation process. The propagation of nonlinearities needs to follow the dispersion relations of the phonon-polarition modes of the crystal, so specific experimental conditions can facilitate the identification of the sources of observable nonlinearities.

5.4 Nonlinearity in the damping term

The nonlinear damping term may need to be accounted for in the large vibrational amplitudes of ionic oscillators, where coupling betweens different phonon modes becomes dependent on the amplitudes:

$$\Gamma(Q) = \Gamma_0 + \alpha Q + \beta Q^2 \tag{5.19}$$

where the coefficient α may vanish for crystals with inversion symmetry.

THz generation based on the nonlinearity of the damping term was simulated in a polar ferroelectric crystal $LiNbO_3$, and the intensity-dependent electric fields and corresponding Fourier spectrum are shown in Figure 5-4 and Figure 5-5. The vibrational amplitudes were in a region where the first order α term can provide a good approximation. The THz electric fields have been normalized with linear

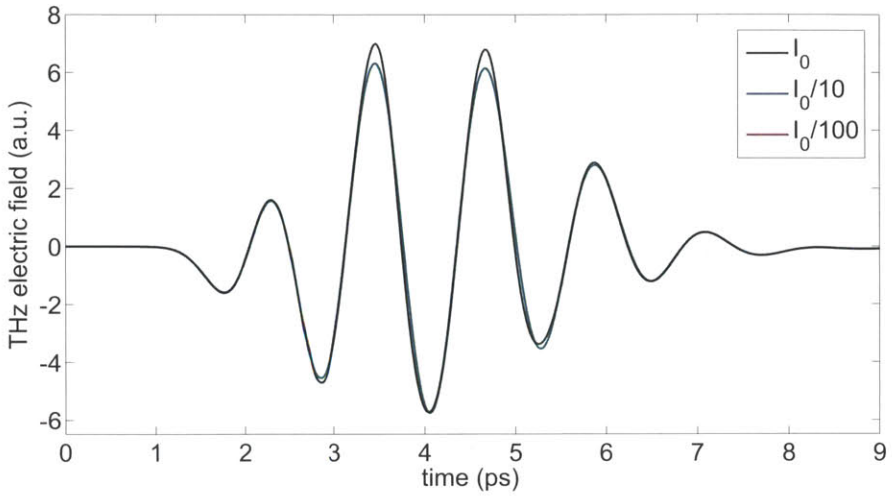

Figure 5-4: The intensity-dependent THz electric fields due to the nonlinearity of the damping term. The amplitudes have been normalized with linear optical intensity dependence.

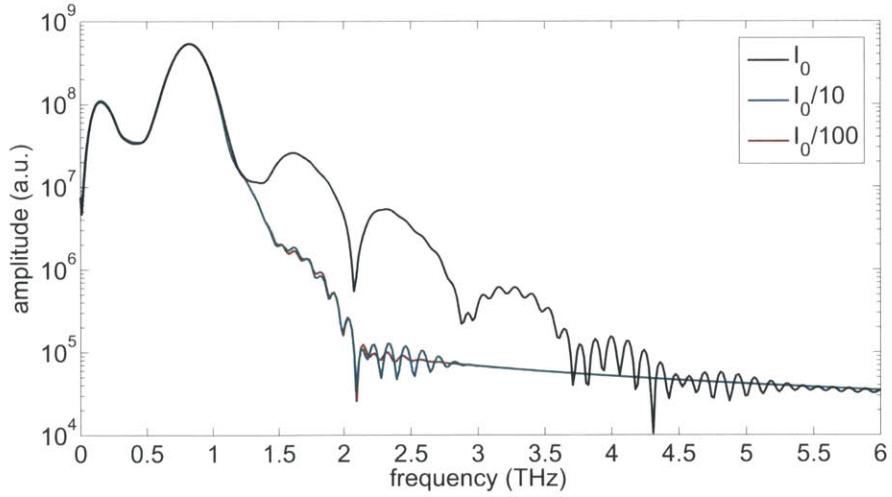

Figure 5-5: The intensity-dependent amplitudes of the THz fundamental and harmonics due to the nonlinearity of the damping term.

optical intensity dependence. As can be seen, several THz harmonics were generated from the nonlinear coefficient. Also, since the nonlinear term does not have inversion symmetry, it can have different effects if the crystal has a different type of spontaneous polarization for large vibrational motions. This is illustrated later in the section on potential surface nonlinearity.

5.5 Nonlinearity in the differential polarizability

The differential polarizability is an essential term in THz generation through the Raman scattering process because the coupling coefficient in the driving force is directly related to it,

$$F_{ISRS} = \frac{1}{2}\epsilon_0\sqrt{\frac{N}{M}}(\frac{\partial\alpha}{\partial\vec{\mathrm{w}}})I_{pump}(x,z,t) \tag{5.20}$$

where $\frac{\partial\alpha}{\partial\vec{\mathrm{w}}}$ is the first-order differential polarizability, and the high-frequency dielectric function $\varepsilon_\infty(Q)$ and b_{22} are functions of ionic displacement Q,

$$\varepsilon_\infty(Q) = N\alpha(Q) = N\left(\alpha_0 + \frac{\partial\alpha}{\partial Q}\bigg|_{Q=0} Q + \frac{1}{2}\frac{\partial^2\alpha}{\partial Q^2}\bigg|_{Q=0} Q^2 + \cdots\right) \tag{5.21}$$

$$b_{22}(Q) = \epsilon_0(\varepsilon_\infty + \lambda_1 Q + \lambda_2 Q^2 - 1) \tag{5.22}$$

and the net displacement $\vec{\mathrm{w}}$ is proportional to the normal mode coordinate.

The nonlinearity of differential polarizability is an electronic effect, and it may create some confusion [14] since the nonlinearity of lattice vibrations and differential polarizability may have similar effects during the generation process. Here, THz generation based on nonlinearity of the differential polarizability was simulated in a polar ferroelectric crystal, $LiNbO_3$, and the intensity-dependent electric fields and corresponding Fourier spectrum are shown in Figure 5-6 and Figure 5-7. The THz electric fields have been normalized with linear optical intensity dependence. As can be seen, several THz harmonics were generated from the nonlinear coefficient.

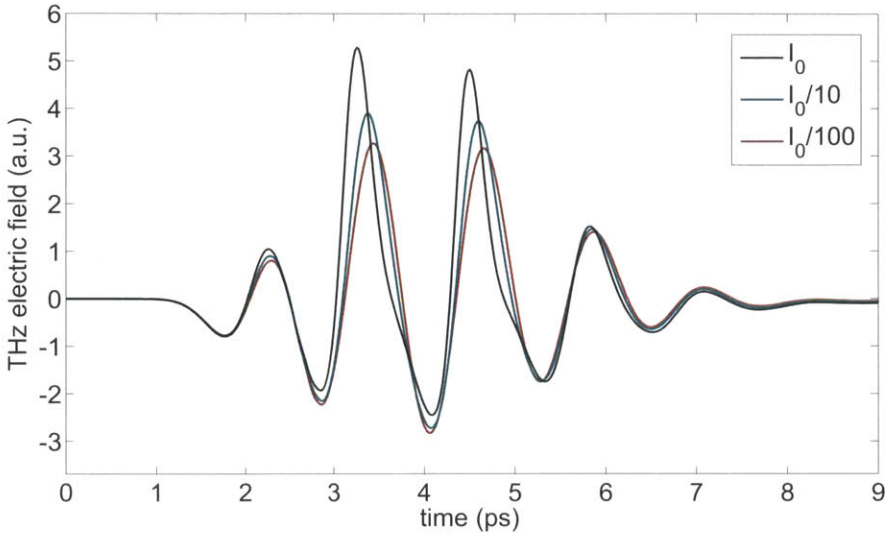

Figure 5-6: The intensity-dependent THz electric fields due to nonlinearity of the differential polarizability. The amplitudes have been normalized with linear optical intensity dependence.

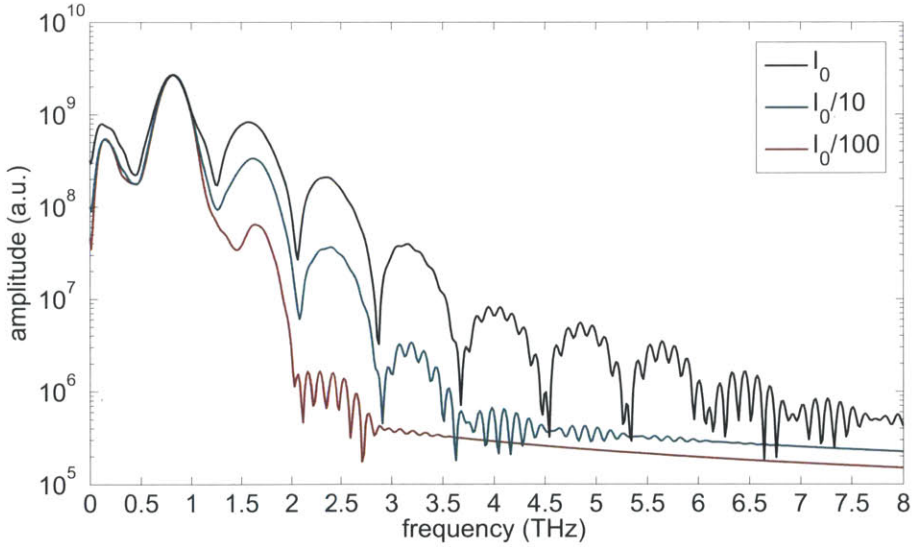

Figure 5-7: The intensity-dependent amplitudes of the THz fundamental and harmonics due to the nonlinearity of the differential polarizability.

5.6 Multiple harmonic generation I

Nonlinearity in the potential energy surface comes with large coherent vibrational amplitudes beyond the harmonic region. The characterization of the potential wells can be realized through the nonlinear phenomena intrinsically linked to the lattice anharmonicity. The potential energy surface along the ferroelectric soft mode coordinate has the double-well shape, and the vibrations around the two equilibrium points may show distinct nonlinear effects due to the intrinsic cubic and quartic anharmonicities. In this section, nonlinear phenomena associated with the vibrations around one of the equilibrium points, or type I spontaneous polarization, are presented with emphasis on the optical intensity dependence and E-Q relations in the large vibrational amplitude region.

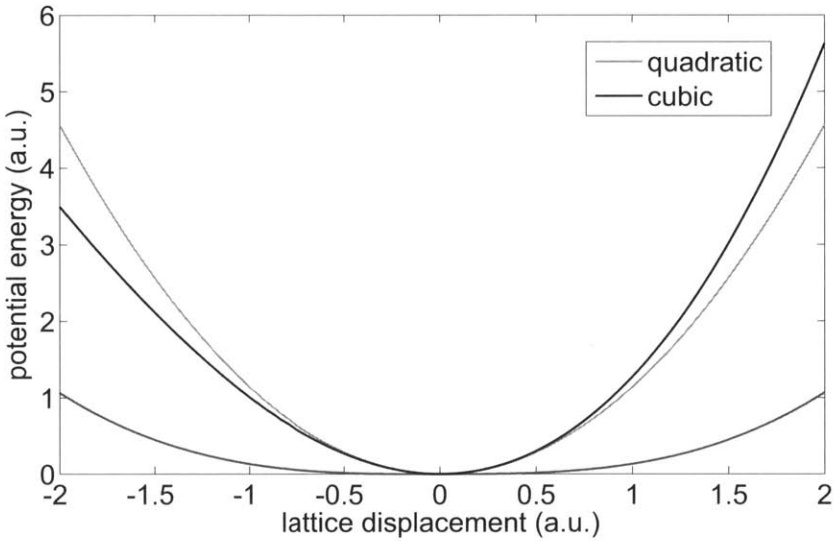

Figure 5-8: The potential energy surface along the ferroelectric soft mode of $LiNbO_3$, and the quadratic and cubic approximations around the local equilibrium point.

The potential energy surface with the quadratic and cubic approximations around the local equilibrium point in the spontaneous polarization type I is shown in Figure 5-8. For a relatively wide region of lattice vibrations in $LiNbO_3$, the quartic term does not show a significant effect. Therefore, the cubic term is also taken into account for simplicity, and the vibrations should be well approximated for the region of multiple

harmonic generation and E-Q relation analysis.

The quadratic and cubic term is $\omega_{TO}^2 Q + aQ^2$ in this case with the coefficient a being a positive number. From the phonon vibration driving equation:

$$\ddot{\vec{Q}} + \Gamma\dot{\vec{Q}} + \omega_{\mathrm{TO}}^2\vec{Q} + a\vec{Q}^2 \;=\; b_{12}\vec{E} + F_{ISRS} \tag{5.23}$$

it can be seen that the initial vibrational direction and amplitude are set forth by the driving force, and the electric field scales approximately with both the quadratic and cubic terms as $E \sim \omega_{TO}^2 Q + aQ^2$. The THz electric field is therefore is enhanced when Q is positive and suppressed when Q is negative due to contributions of the cubic term, and the larger the vibrational amplitude, the larger this anharmonic effect is. This effect has been simulated in THz generation as shown in Figure 5-9 and Figure 5-10, with the amplitudes of the electric field and lattice displacement, and the corresponding Fourier spectra.

The intensity-dependent THz electric field and the corresponding Fourier spectra are shown in Figure 5-11 and Figure 5-12. The electric fields have been normalized based on the linear dependence of the optical intensity, and it can be seen that the electric field with large vibrational amplitude is less than the normalized proportionality because the initial lattice movement is driven into the negative direction where the electric field is slightly suppressed by the lattice cubic anharmonicity.

In the THz electric field spectrum, the THz fundamental and multiple harmonics can be clearly observed in the high-intensity region. The amplitudes of the second, third, and higher-order harmonics as functions of the amplitude of the THz fundamental are shown in Figure 5-13 and Figure 5-14.

5.7 Multiple harmonic generation II

In this section, nonlinear phenomena associated with the vibrations around the other equilibrium point, or type II spontaneous polarization, are presented with optical intensity dependence and E-Q relations in the large vibrational amplitude region due

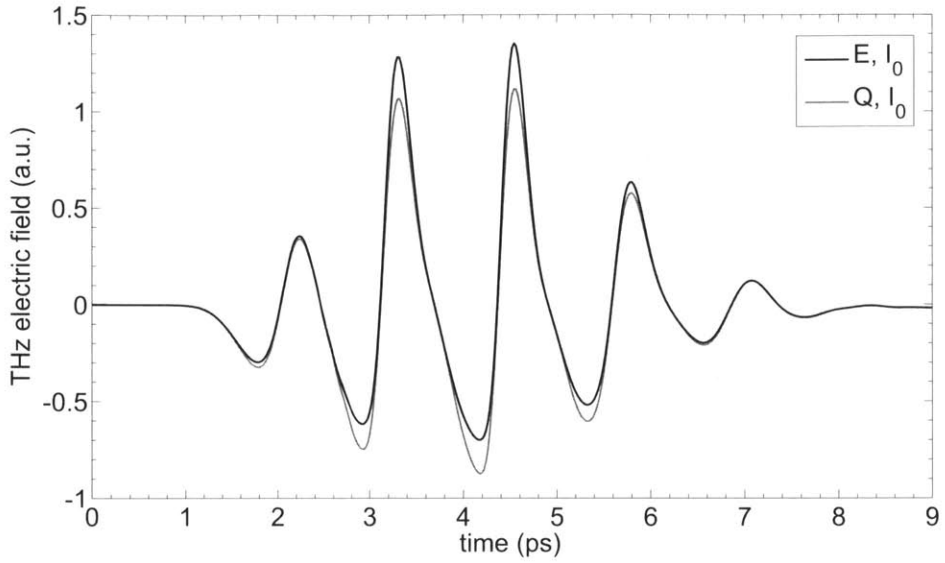

Figure 5-9: The amplitudes of the electric field and lattice displacement with high intensity excitation, where the electric field is enhanced when Q is positive and suppressed when Q is negative due to the lattice anharmonicity.

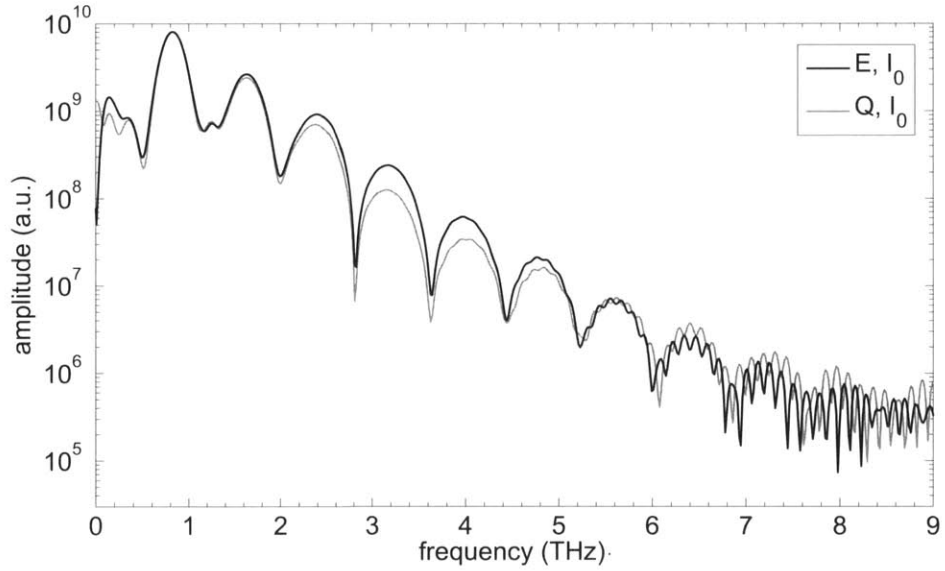

Figure 5-10: The corresponding Fourier spectra of the electric field and lattice displacement with high-intensity excitation and large vibrational amplitudes.

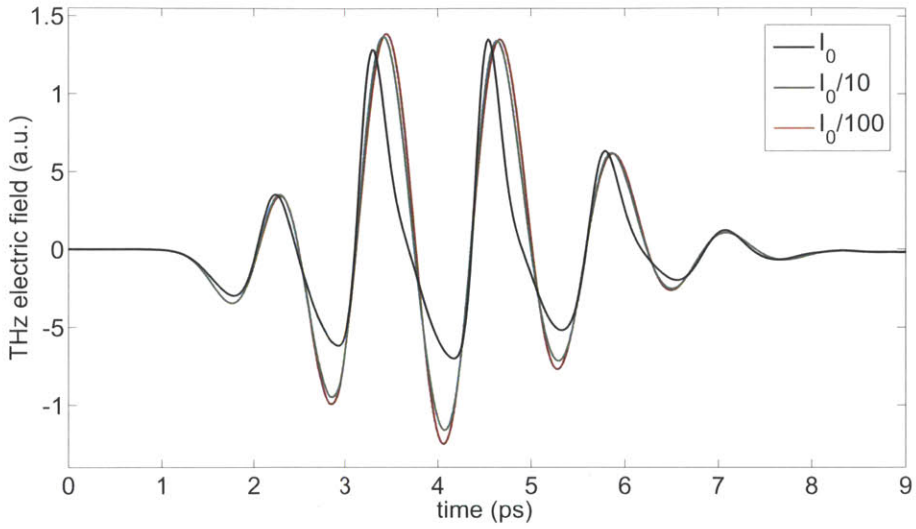

Figure 5-11: The intensity-dependent THz electric field normalized based on the linear dependence on optical intensity. The electric field with large vibrational amplitude is less than the normalized proportionality because the initial lattice movement is driven into the negative direction where the electric field is suppressed by the lattice cubic anharmonicity.

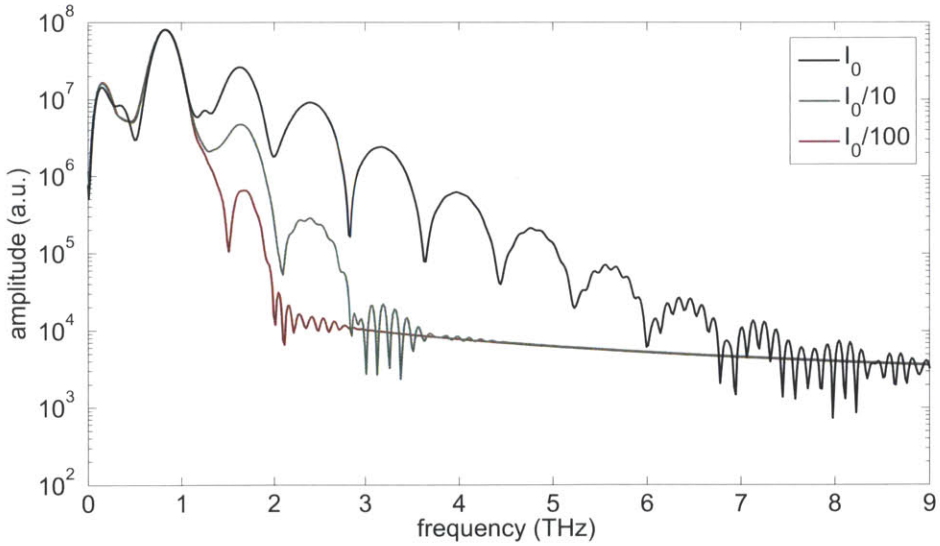

Figure 5-12: The corresponding intensity-dependent Fourier spectra of the THz fundamental and multiple harmonics generated by the lattice cubic anharmonicity.

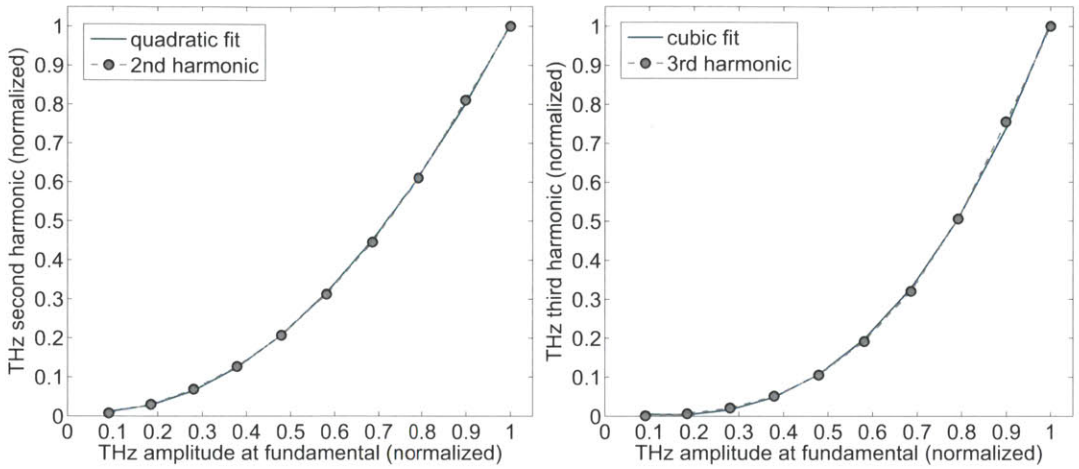

Figure 5-13: The amplitudes of the THz second and third harmonics show quadratic and cubic dependence of the THz fundamental generated through the cubic lattice anharmonicity.

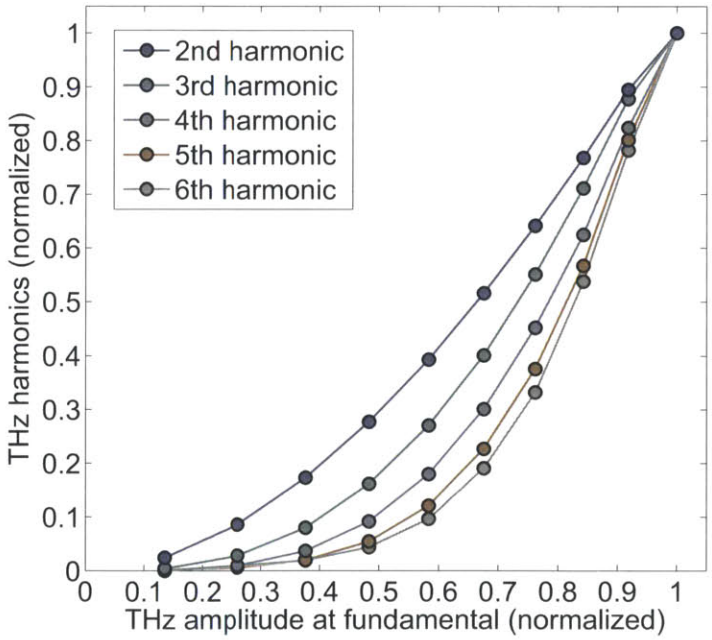

Figure 5-14: The normalized amplitudes of the multiple THz harmonics as a function of the amplitude of the THz fundamental generated through the cubic lattice anharmonicity.

to lattice anharmonicity.

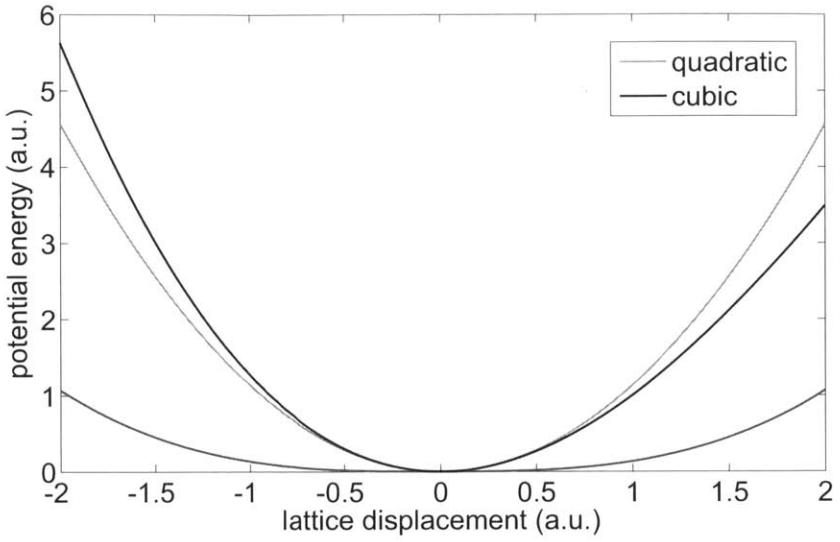

Figure 5-15: The potential energy surface along the ferroelectric soft mode of $LiNbO_3$, and the quadratic and cubic approximations around the local equilibrium point.

Figure 5-15 shows the potential energy surface with the quadratic and cubic approximations around the local equilibrium point in the spontaneous polarization type II. Since it shows mirror symmetry with the other type of polarization, the cubic term is taken into account for simplicity, and vibrations should be well approximated for the region of multiple harmonic generation and E-Q relation analysis.

The quadratic and cubic term is $\omega_{TO}^2 Q - aQ^2$ in this case and the coefficient a is a positive number. From the phonon vibration driving equation

$$\ddot{\vec{Q}} + \Gamma\dot{\vec{Q}} + \omega_{\mathrm{TO}}^2\vec{Q} - a\vec{Q}^2 \;=\; b_{12}\vec{E} + F_{ISRS} \tag{5.24}$$

it can be seen that the initial vibrational direction and amplitude is set by the driving force, and the electric field scales approximately with both the quadratic and cubic terms as $E \sim \omega_{TO}^2 Q - aQ^2$. The THz electric field in this case is therefore enhanced when Q is negative and suppressed when Q is positive due to contributions of the cubic term. The larger the vibrational amplitude, the larger this anharmonic effect is. This effect has been simulated in THz generation as shown in Figure 5-16 and Figure 5-17, with amplitudes of the electric field and lattice displacement, and the

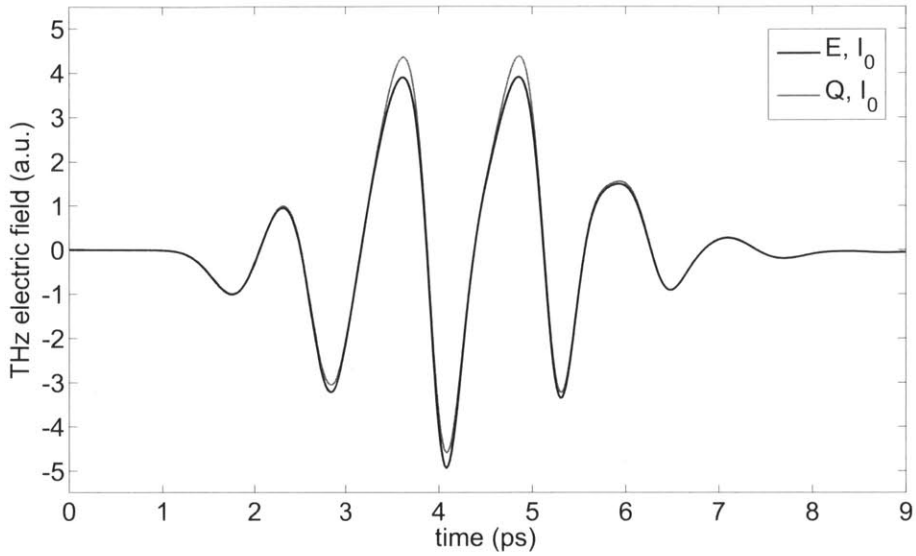

Figure 5-16: The amplitudes of the electric field and lattice displacement with high-intensity excitation. The electric field is enhanced when Q is negative and suppressed when Q is positive due to the lattice anharmonicity.

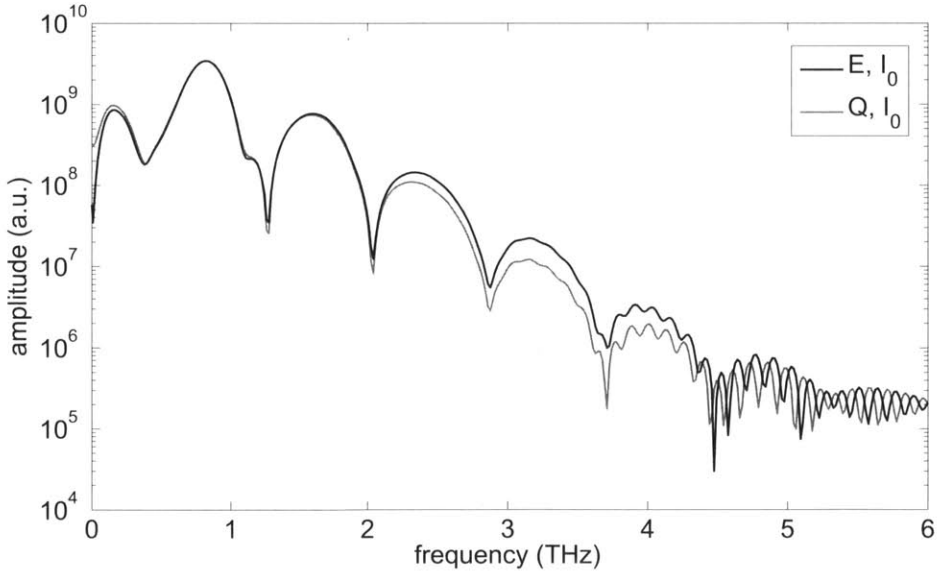

Figure 5-17: The corresponding Fourier spectra of the electric field and lattice displacement with high-intensity excitation and large vibrational amplitudes.

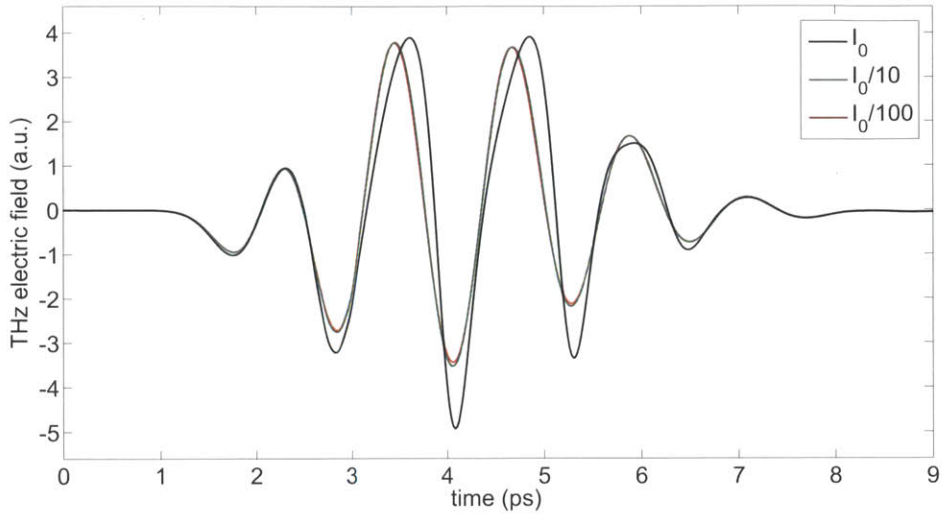

Figure 5-18: The intensity-dependent THz electric field normalized based on the linear dependence on the optical intensity. The electric field with large vibrational amplitude is less than the normalized proportionality because the initial lattice movement is driven into the negative direction where the electric field is enhanced by the lattice cubic anharmonicity.

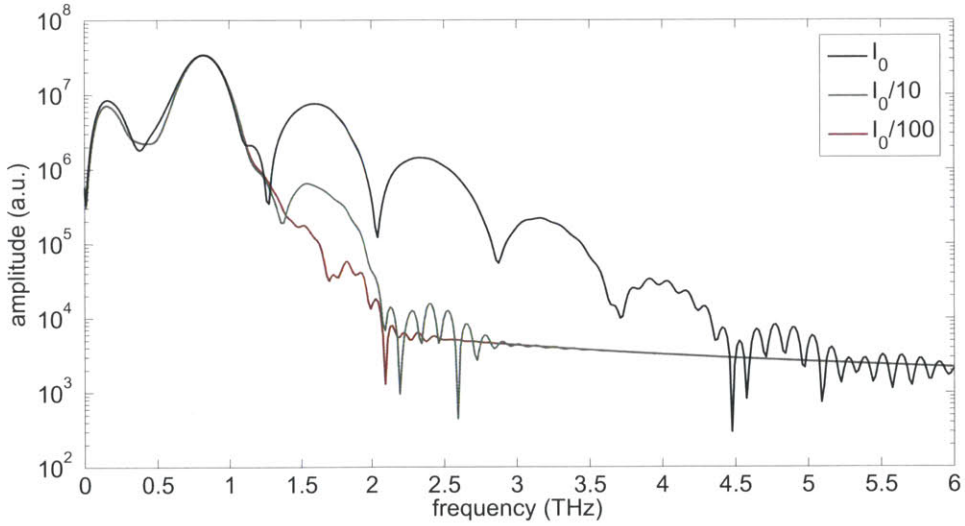

Figure 5-19: The corresponding intensity-dependent Fourier spectra of the THz fundamental and multiple harmonics generated through the cubic lattice anharmonicity.

corresponding Fourier spectra.

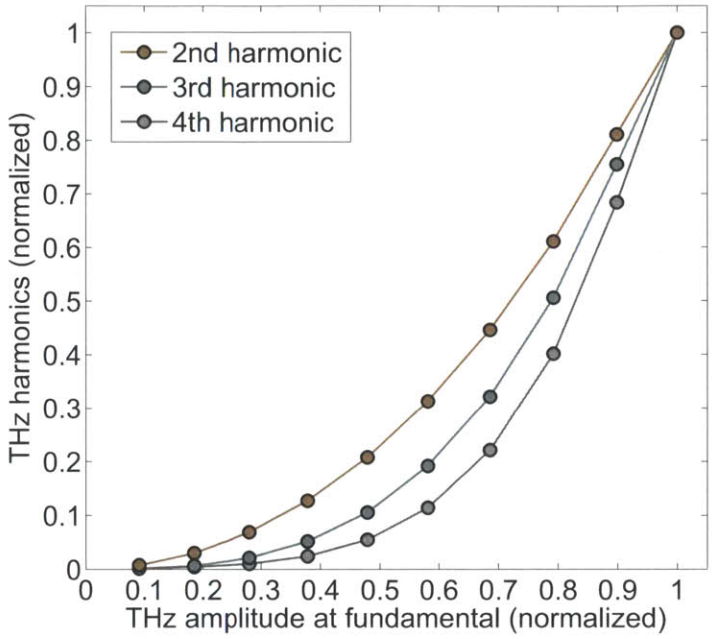

Figure 5-20: Normalized amplitudes of the multiple THz harmonics as a function of the amplitude of the THz fundamental generated through the cubic lattice anharmonicity.

The intensity-dependent THz electric field and the corresponding Fourier spectra are shown in Figure 5-18 and Figure 5-19. The electric fields have been normalized based on the linear dependence on the optical intensity, and it can be seen that the electric field with large vibrational amplitude is more than the normalized proportionality because the initial lattice movement is driven into the negative direction where the electric field is slightly enhanced by the lattice cubic anharmonicity.

In the THz electric field spectrum, the THz fundamental and multiple harmonics can be clearly observed at the high-intensity region. In Figure 5-20, the normalized amplitudes of higher order harmonics as functions of the amplitude of the THz fundamental are presented.

5.8 Phase modulation from lattice anharmonicity

THz phase modulation has been observed in high-power THz generation experiments in $LiNbO_3$ cooled to temperatures as low as 10K. In this section, simulations of intensity-dependent near-single-cycle THz pulses are presented in LN crystal with cubic lattice anharmonicity and reduced damping.

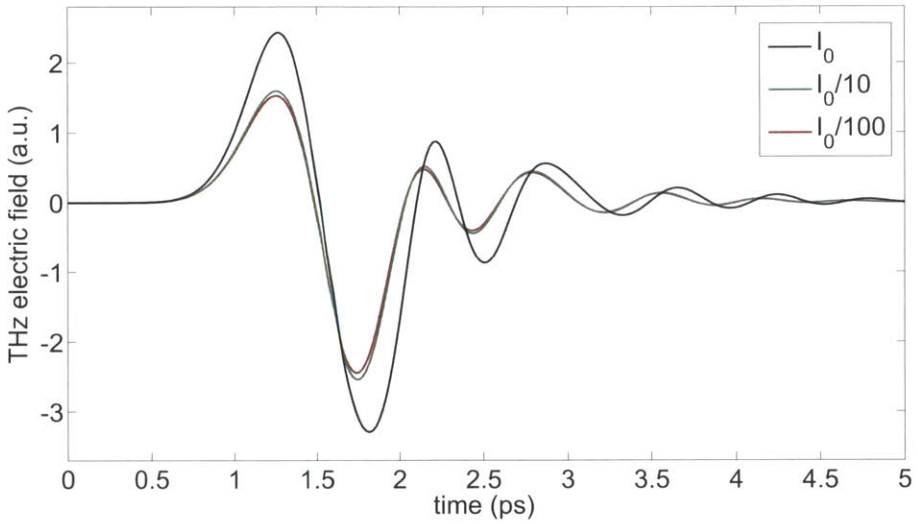

Figure 5-21: The intensity-dependent THz electric field in $LiNbO_3$ with cubic lattice anharmonicity and reduced damping. The amplitudes are normalized with linear dependence on optical intensities and phase modulation can be observed. The positions of both the peak and valley are intensity-dependent, and the oscillation period is longer at higher intensities.

As can been in Figure 5-21, the near-single-cycle THz pulses show a few more oscillations following the main peak, and the positions of both the peak and valley are intensity-dependent. The electric field amplitudes have been normalized with linear dependence on optical intensities and the phase modulation can be observed. In the time domain, the oscillation period is larger at higher intensities, and the extra time delay can be related to the intensity-dependent index change. The normalized amplitudes of the electric field and lattice vibrations at high and low optical intensities are presented in Figure 5-22, and it can be confirmed that the lattice vibrations closely follow the THz electric fields, and that the phase modulation reflects the lattice anharmonicity. The amplitudes of the THz electric fields in the frequency domain

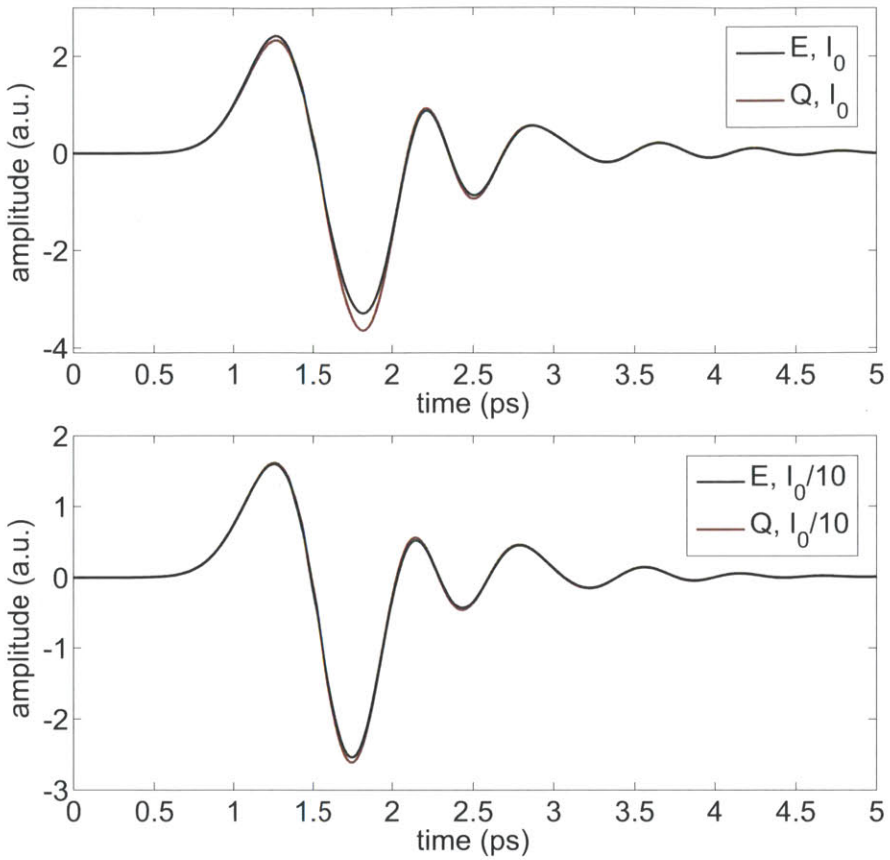

Figure 5-22: Normalized amplitudes of the electric field and lattice vibrations at high and low optical intensities. The lattice vibrations closely follow the THz electric fields, and the phase modulation reflects the lattice anharmonicity.

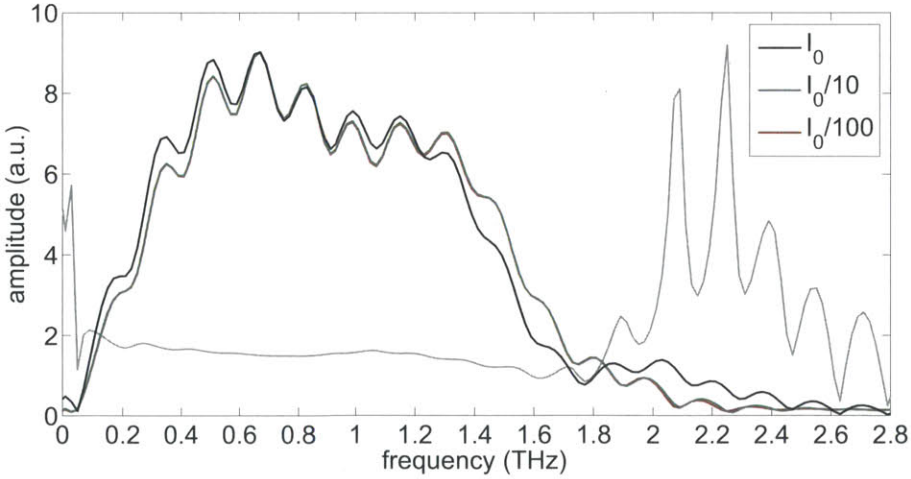

Figure 5-23: Amplitudes of the THz electric fields in the frequency domain where the spectral components at low and high frequencies are enhanced. The ratio between them shows the characteristic spectral change in nonlinear phase modulations.

are presented in Figure 5-23, and it can be seen that the spectral components at low and high frequencies are enhanced. The ratio between them shows the characteristic spectral change in nonlinear phase modulations.

5.9 Multiple harmonic generation experiment

Coherent anharmonic phonon-polaritons in ferroelectric crystals have been observed through wavevector overtone spectroscopy in $LiTaO_3$ [14] where up to 9 overtones were generated with high optical intensity excitation. Nonlinear phase modulation and harmonic generation were also reported through high-power THz generation in $LiNbO_3$ [55]. In this section, experimental results of THz multiple harmonic generation are presented.

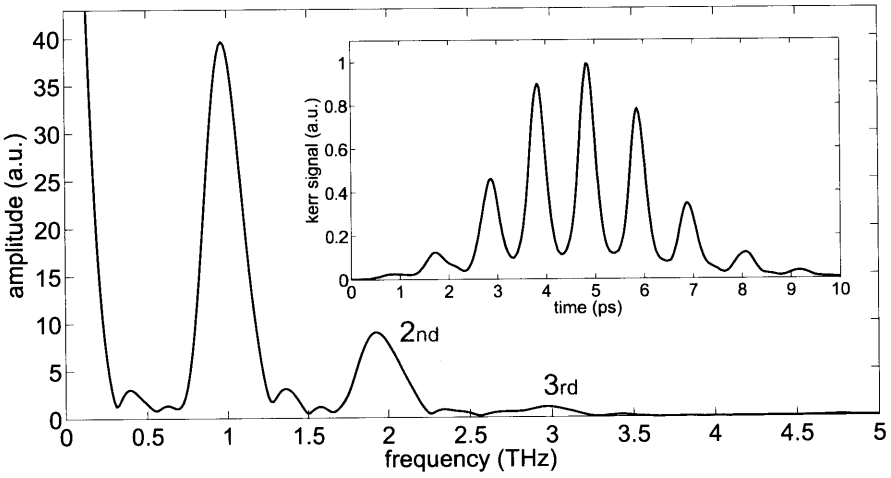

Figure 5-24: A third-order cross-correlation experiment between the optical chirp-and-delay etalon output and a transform-limited readout pulse in silica glass where second and third harmonics can be observed.

Pumped with the intensity front tilted quasi-sinusoidal modulated optical waveforms in a $LiNbO_3$ prism, the multiple-cycle phonon-polariton waves can be generated and continuously enhanced along with the coherent lattice vibrations that are strongly coupled with the electric field. If the vibrational amplitude is sufficiently large to reach the nonlinear region, harmonics of the fundamental frequency as determined by the

intensity modulation should be observable.

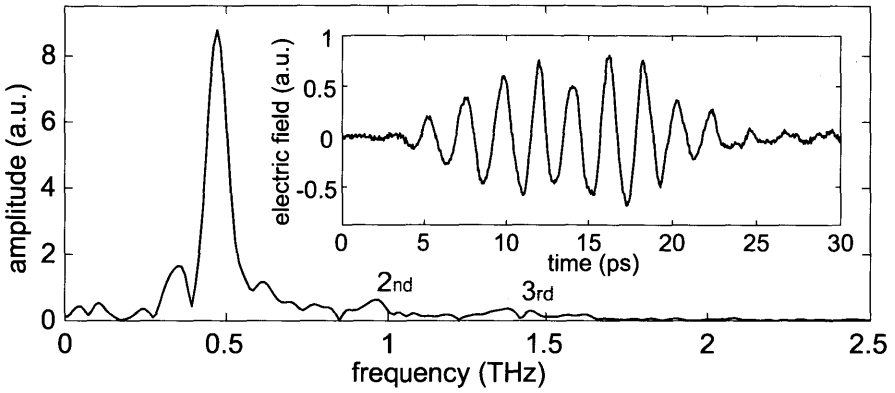

Figure 5-25: A multiple-cycle THz trace generated by a 6 mJ optical pump pulse where the second and third harmonics can be observed.

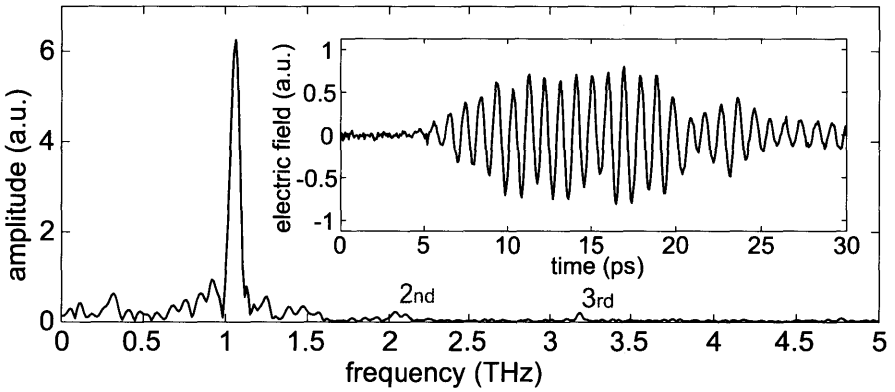

Figure 5-26: A multiple-cycle THz trace generated by a 6 mJ optical pump pulse where the second and third harmonics can be observed.

The third-order cross-correlation measurement between the optical chirp-and-delay etalon output and a transform-limited readout pulse in silica glass is shown in Figure 5-24, where some second and third optical harmonics can be observed. This is the optical input of the THz generation process, and the peak amplitudes of the second and third harmonics versus the fundamental are 0.226 and 0.0275 respectively.

The experimental results of generation of multiple-cycle THz waves pumped with 6 mJ optical pulses are shown in Figure 5-25 where the fundamental frequency is around 0.49 THz, and the peak amplitudes of the second and third harmonics relative to the fundamental are 0.0724 and 0.0345. In Figure 5-26 where the fundamental frequency

is around 1.06 THz, the peak amplitudes of the second and third harmonics versus the fundamental are 0.0276 and 0.0332. The experimental results of multiple-cycle THz waves pumped with 35 mJ optical pulses are shown in Figure 5-27 where the fundamental frequency is around 0.53 THz, and the peak amplitudes of the second, third, and fourth harmonics versus the fundamental are 0.1812, 0.0463, and 0.0285 respectively.

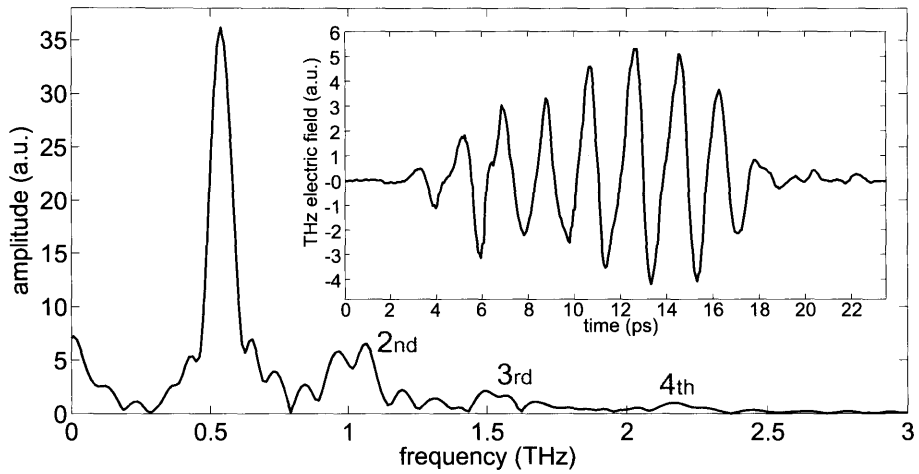

Figure 5-27: The experimental result of a multiple-cycle THz trace generated with a 35 mJ optical pump pulse, where the second, third, and fourth harmonics can be observed. Given the experimental geometry, actual harmonic components may be more than what were measured through electro-optic sampling. This may be due to the lattice nonlinearity of the $LiNbO_3$ crystal.

There are several processes involved in the multiple harmonic generation experiment. The higher-order harmonics in the optical input were mostly filtered by the following considerations: (a) the damping rates of THz pulses are significantly larger for higher frequency components above 1 THz; (b) in the experimental geometry, velocity matching was realized for a certain region of frequencies around the main peak for the optimization of THz total pulse energies, so the higher the frequencies, the less the phase matching condition was met. On the other hand, as the modulated optical waveform propagated through the sample, the phonon-polariton waves were continuously generated and enhanced. When the amplitudes of the electric fields and lattice vibrations approach the nonlinear region, higher-order harmonics of the fundamental should appear and propagate along with the fundamental. This can be confirmed by

the amount of harmonic components with various optical intensities and the appearance of new harmonic components in the THz waves. Another point to look at the nonlinearity is that in this experiment, the peak optical intensity is lowered since the pulse is spread spatiotemporally. The dimensions in the high-intensity case are 10 ps $\times$ 5 mm $\times$ 5 mm, so more harmonic components can be generated with more tightly focused pulses.

Chapter 6

Conclusions

The recent development of high-energy THz sources has made it possible to do various nonlinear optics and spectroscopy experiments in the THz regime. In this thesis, we presented general background on, and demonstrated experimental techniques for, the generation and enhancement of near-single-cycle and multiple-cycle THz pulses based on coherent optical excitation of phonon-polaritons in ferroelectric crystals such as $LiNbO_3$ and $LiTaO_3$. We showed that pulse energies can reach 50 μJ for near-single-cycle pulses with sub-picosecond duration and 10 μJ for multiple-cycle pulses with picosecond duration. These are achieved through noncollinear velocity matching geometry by tilting the intensity front of near-infrared ultrashort optical pulses or quasi-sinusoidal modulated waveforms. These THz outputs are very close approximations to Gaussian beams, and can be well collimated and focused into samples for time-resolved experiments in linear and nonlinear THz optics and spectroscopy. Collective coherent excitation and control of lattice dynamics along selected potential energy surfaces are of considerable interest, particularly properly tailoring of THz pulses to drive large amplitude motions associated with some aspects of macroscopic properties. Many macroscopic quantum phenomena, such as quantum coherence within a few energy levels, can be properly excited and observed with well-defined THz pulses and high field strength. Nonlinear coherent spectroscopy is relatively mature in the visible, infrared, and radio frequency regions, and the methods developed in this thesis can now allow for extensions of methods such as the photon echo and

multidimensional spectroscopy into the THz region.

Bibliography

[1] S. Adachi, R.M. Koehl, and K.A. Nelson. Real-space and real-time imaging of polariton wavepackets. *J. Lumin.*, 87-89:840–843, 2000.

[2] J. Ahn, A.V. Efimov, R.D. Averitt, and A.J. Taylor. Terahertz waveform synthesis via optical rectification of shaped ultrafast laser pulses. *Opt. Express*, 11:2486, 2003.

[3] A. Assion, T. Baumert, M. Bergt, T. Brixner, B. Kiefer, V. Seyfried, M. Strehle, and G. Gerber. Control of chemical reactions by feedback-optimized phase-shaped femtosecond laser pulses *Science*, 282:919-922, 1998.

[4] D.H. Auston, and P.R. Smith. Generation and detection of millimeter waves by picosecond photoconductivity. *Appl. Phys. Lett.*, 43:631, 1983.

[5] D.H. Auston, K.P. Cheung, J.A. Valdmanis, and D.A. Kleinman. Cherenkov radiation from femtosecond optical pulses in electro-optic media. *Phys. Rev. Lett.*, 53:1555-1558, 1984.

[6] Jr. A.S. Barker and R. Loudon. Dielectric properties and optical phonons in $LiNbO_3$. *Phys. Rev.*, 158:433-445, 1967.

[7] Jr. A.S. Barker and R. Loudon. Response functions in the theory of Raman scattering by vibrational and polariton modes in dielectric crystals. *Rev. Mod. Phys.*, 44:18-47, 1972.

[8] S. Bielawski, C. Evain, T. Hara, M. Hosaka, M. Katoh, S. Kimura, A. Mochihashi, M. Shimada, C. Szwaj, T. Takahashi, and Y. Takashima. Tunable narrowband terahertz emission from mastered laser-electron beam interaction. *Nature Physics*, 4:390–393, 2008.

[9] F. Blanchard, L. Razzari, H.-C. Bandulet, G. Sharma, R. Morandotti, J.-C. Kieffer, T. Ozaki, M. Ried, H.F. Tiedje, H.K. Haugen, and F.A. Hegmann. Generation of 1.5 μJ single-cycle terahertz pulses by optical rectification from a large aperture ZnTe crystal. *Opt. Express*, 15:13212C13220, 2007.

[10] N. Bloembergen. A quarter century of stimulated Raman scattering. *Pure and Appl. Chem.*, 59:1229-1236, 1987.

[11] G.D. Boyd and M.A. Pollack. Microwave nonlinearities in anisotropic dielectrics and their relation to optical and electro-optical nonlinearities. *Phys. Rev. B*, 7:5345-5359, 1973.

[12] M. Born and K. Huang. *Dynamical Theory of Crystal Lattices.* Oxford University Press, London, 1954.

[13] Ciaran Joseph Brennan. *Femtosecond wavevector overtone spectroscopy of anharmonic lattice dynamics in ferroelectric crystals.* PhD thesis, Massachusetts Institute of Technology, 1997.

[14] C.J. Brennan and K.A. Nelson. Direct time-resolved measurement of anharmonic lattice vibrations in ferroelectric crystals. *J. Chem. Phys.*, 107:9691, 1997.

[15] L. Brillouin. Diffusion of light and x-rays by a transparent homogeneous body. the influence of thermal agitation. *Ann. phys. (Paris)*, 17:88–122, 1922.

[16] M.H. Brodsky, E. Burstein, M. Cardona, L.M. Falicov, M.V. Klein, R.M. Martin, A. Pinczuk, A.S. Pine, and Y.-R. Shen. *Light Scattering in Solids.* Springer-Verlag, 1975.

[17] G.L. Carr, M.C. Martin, W.R. McKinney, K. Jordan, G.R. Neil, and G.P. Williams. High power terahertz radiation from relativistic electrons. *Nautre*, 420:153-156, 2002.

[18] A. Cavalleri, S. Wall, C. Simpson, E. Statz, D.W. Ward, K.A. Nelson, M. Rini, and R. W. Schoenlein. Tracking the motion of charges in a terahertz light field by femtosecond x-ray diffraction. *Nautre*, 442:664–666, 2006.

[19] Z. Chen, X. Zhou, C.A. Werley, and K.A. Nelson. Generation of high power tunable multicycle teraherz pulses. *Appl. Phys. Lett.*, 99:071102, 2011.

[20] R.Y. Chiao, C. H. Townes, and B.P. Stoicheff. Stimulated brillouin scattering and coherent generation of intense hypersonic waves. *Phys. Rev. Lett.*, 12:592–595, 1964.

[21] R. Claus, L. Merten, and J. Brandmüller. *Light scattering by phonon-polaritons.* Springer Tracts in Modern Physics, 1975.

[22] M. Posledovich, F. X. Winter, G. Borstel, and R. Claus. Properties of extraordinary polaritons in $LiNbO_3$. *phys. stat. sol. (b)*, 55:711, 1973.

[23] T.F. Crimmins, N.S. Stoyanov, and K.A. Nelson. Heterodyned impulsive stimulated raman scattering of phonon-polaritons in $LiTaO_3$ and $LiNbO_3$. *J. Chem. Phys.*, 117:2882–2896, 2002.

[24] Timothy Francis Crimmins. *Ultrahigh Frequency Characterization of Complex Materials using Transient Grating Techniques.* PhD thesis, Massachusetts Institute of Technology, 2000.

[25] J.R. Danielson, A.D. Jameson, J.L. Tomaino, H.Hui, J.D. Wetzel, Y.-S. Lee, and K.L. Vodopyanov. Intense narrow band terahertz generation via type-II difference-frequency generation in ZnTe using chirped optical pulses. *J. Appl. Phys*, 104:033111, 2008.

[26] T. Dekorsy, V.A. Yakovlev, W. Seidel, M. Helm, and F. Keilmann. Infrared phonon polariton resonance of the nonlinear susceptibility in GaAs. *Phys. Rev. Lett.*, 90:055508, 2003.

[27] L. Dhar, J.A. Rogers, and K.A. Nelson. Time-resolved vibrational spectroscopy in the impulsive limit. *Chem. Rev.*, 94 (1):157-193, 1994.

[28] T.P. Dougherty, G.P. Wiederrecht, and K.A. Nelson. Impulsive stimulated raman scattering experiments in the polariton regime. *J. Opt. Soc. Am. B.*, 9:2179–2189, 1992.

[29] T.P. Dougherty, G.P. Wiederrecht, K.A. Nelson, M.H. Garrett, H.P. Jenssen and C. Warde. Femtosecond resolution of soft mode dynamics in structural phase transitions. *Science*, 258:770–774, 1992.

[30] T.P. Dougherty, G.P. Wiederrecht, K.A. Nelson, M.H. Garrett, H.P. Jenssen, and C. Warde. Femtosecond time-resolved spectroscopy of soft modes in structural phase transitions of perovskites. *Phys. Rev. B*, 50:8996-9019, 1994.

[31] D. Dragoman and M. Dragoman. *Optical Characterization of Solids.* Springer, 2001.

[32] G. Eckhardt, R.W. Hellwarth, F.J. McClung, S.E. Schwarz, D. Weiner, and E.J. Woodbury. Stimulated Raman scattering from organic liquids. *Phys. Rev. Lett.*, 9:455-457, 1962.

[33] T. Bartel, P. Gaal, K. Reimann, M.Woerner, and T. Elsaesser. Generation of single-cycle THz transients with high electric-field amplitudes. *Opt. Lett.*, 30:2805-2807, 2005.

[34] M.R. Farrar, L.-T. Cheng, Y.-X. Yan, and K.A. Nelson. Impulsive stimulated brillouin scattering in KD_2PO_4 near the structural phase transition. *Quantum Electronics, IEEE Journal of*, 22:1453 – 1456, 1986.

[35] C. Fattinger and D. Grischkowsky. Terahertz beams. *Appl. Phys. Lett.*, 54:490, 1989.

[36] T. Feurer, N.S. Stoyanov, D.W. Ward, J.C. Vaughan, E.R. Statz, and K.A. Nelson. Terahertz polaritonics. *Annu. Rev. Mater. Res.*, 37:317–350, 2007.

[37] T. Feurer, J.C. Vaughan, and K.A. Nelson. Spatiotemporal coherent control of lattice vibrational waves. *Science*, 299:374–377, 2003.

[38] T. Feurer, J.C. Vaughan, T. Hornung, and K.A. Nelson. Typesetting of terahertz waveforms. *Opt. Lett.*, 29:1802–1804, 2004.

[39] S. Fleischer, Y. Zhou, R.W. Field, and K.A. Nelson. Molecular orientation and alignment by intense single cycle THz pulses. *Phys. Rev. Lett.*, 107:163603, 2011.

[40] C. Flytzanis. Infrared dispersion of second-order electric susceptibilities in semiconducting compounds. *Phys. Rev. B*, 6:1264, 1972.

[41] J.A. Fülöp, L. Pálfalvi, M.C. Hoffmann, and J. Hebling. Towards generation of mJ-level ultrashort THz pulses by optical rectification. *Opt. Express*, 19:15090, 2011.

[42] J.A. Fülöp, L. Pálfalvi, S. Klingebiel, G. Almási, F. Krausz, S. Karsch, and J. Hebling. Generation of sub-mJ terahertz pulses by optical rectification. *Opt. Lett.*, 37:557-559, 2012.

[43] G. Gallot, J. Zhang, R.W. McGowan, Tae-In Jeon, and D. Grischkowsky. Measurements of the THz absorption and dispersion of ZnTe and their relevance to the electro-optic detection of THz radiation. *Appl. Phys. Lett.*, 74:3450, 1999.

[44] E. Garmire, F.Pandarese, and C.H. Townes. Coherently driven molecular vibrations and light modulation. *Phys. Rev. Lett.*, 11:160-163, 1963.

[45] C. Garrett Nonlinear optics, anharmonic oscillators, and pyroelectricity. *IEEE Journal of Quantum Electronics*, 4:70-84, 1963.

[46] S. Ghimire, A. D. DiChiara, E. Sistrunk, P. Agostini, L. F. DiMauro, and D. A. Reis. Observation of high-order harmonic generation in a bulk crystal. *Nature Physics*, 7:138-141, 2011.

[47] O. Golonzka, M. Khalil, N. Demirdoven, and A. Tokmakoff. Vibrational anharmonicities revealed by coherent two-dimensional infrared spectroscopy. *Phys. Rev. Lett.*, 86:2154, 2001.

[48] D. Grischkowsky, S. Keiding, M.V. Exter, and Ch. Fattinger. Far-infrared time-domain spectroscopy with terahertz beams of dielectrics and semiconductors. *J. Opt. Soc. Am. B.*, 7:2006-2015, 1990.

[49] G. Grosso and G.P. Parravicini. *Solid State Physics.* Academic Press, 2000.

[50] W. Hayes and R. Loudon. *Scattering of light by crystals.* Wiley, New York, 1978.

[51] J. Hebling. Derivation of the pulse front tilt caused by angular dispersion. *Optical and Quantum Electronics*, 28:1759–1763, 1996.

[52] J. Hebling, G. Almasi, I. Kozma, and J. Kuhl. Velocity matching by pulse front tilting for large area thz-pulse generation. *Opt. Express*, 10:1161–1166, 2002.

[53] J. Hebling, A.G. Stepanov, G. Almasi, B. Bartal, and J. Kuhl. Tunable THz pulse generation by optical rectification of ultrashort laser pulses with tilted pulse fronts. *Appl. Phys. B: Lasers Opt.*, 78:593, 2004.

[54] J. Hebling, K.-L. Yeh, M.C. Hoffmann, B. Bartal, and K.A. Nelson. Generation of high power THz pulses by tilted pulse front excitation and their application possibilities. *J. Opt. Soc. Am. B.*, 25:B6-B19, 2008.

[55] J. Hebling, K.-L. Yeh, M.C. Hoffmann, and K.A. Nelson. High power THz generation, THz nonlinear optics, and THz nonlinear spectroscopy. *IEEE J. Selected Topics in Quantum Electronics.*, 14:345–353, 2008.

[56] G. Almási, J.A. Fülöp, L. Pálfalvi, and J. Hebling. Design of high-energy terahertz sources based on optical rectification. *Opt. Express*, 18:12311–12327, 2010.

[57] C.H. Henry and J.J. Hopfield. Raman scattering by polaritons. *Phys. Rev. Lett.*, 15:964–966, 1965.

[58] H. Hirori, A. Doi, F. Blanchard, and K. Tanaka. Single-cycle terahertz pulses with amplitudes exceeding 1 MV/cm generated by optical rectification in $LiNbO_3$. *Appl. Phys. Lett.*, 98:091106, 2011.

[59] M.C. Hoffmann, K.-L. Yeh, J. Hebling, and K.A. Nelson. Efficient THz generation by optical rectification at 1035 nm. *Opt. Express*, 15:11706, 2007.

[60] M.C. Hoffmann, J. Hebling, H.Y. Hwang, K.-L. Yeh, and K.A. Nelson. THz kerr effect. *Appl. Phys. Lett.*, 95:231105, 2009.

[61] M.C. Hoffmann, J. Hebling, H.Y. Hwang, K.-L. Yeh, and K.A. Nelson. THz-pump/THz-probe spectroscopy of semiconductors at high field strengths [Invited]. *J. Opt. Soc. Am. B.*, 26:A29, 2009.

[62] M.C. Hoffmann and J.A. Fülöp. Intense ultrashort terahertz pulses: generation and applications. *J. Phys. D: Appl. Phys.*, 44:083001, 2011.

[63] M.C. Hoffmann, S. Schulz, S. Wesch, S. Wunderlich, A. Cavalleri, and B. Schmidt. Coherent single-cycle pulses with MV/cm field strengths from a relativistic transition radiation light source. *Opt. Lett.*, 36:4473, 2011.

[64] T. Hornung, K.-L. Yeh, and K.A. Nelson. Terahertz nonlinear response in lithium niobate. In P. Corkum, D. Jonas, D. Miller, and A.M. Weiner, editors, *Ultrafast Phenomena XV*, pages 772–774, Berlin, 2007. Springer-Verlag.

[65] K. Huang. On the interaction between the radiation field and ionic crystals. *Proceedings of the Royal Society of London. Series A, Mathematical and Physical Sciences*, 208(1094):352–365, 1951.

[66] M. Liu, H. Y. Hwang, H. Tao, A.C. Strikwerda, K. Fan, G.R. Keiser, A.J. Sternbach, K.G. West, S. Kittiwatanakul, J. Lu, S.A. Wolf, F.G. Omenetto, X. Zhang, K.A. Nelson, and R.D. Averitt. Terahertz-field-induced insulator-to-metal transition in vanadium dioxide metamaterial. *Nature*, 487:345-348, 2012.

[67] I. Inbar and R.E. Cohen. Comparison of the electronic structures and energetics of ferroelectric $LiNbO_3$ and $LiTaO_3$. *Phys. Rev. B.*, 1193-1204, 1996.

[68] M. Jewariya, M. Nagai, and K. Tanaka. Enhancement of terahertz wave generation by cascaded $\chi^{(2)}$ processes in $LiNbO_3$. *J. Opt. Soc. Am. B.*, 26:A101, 2009.

[69] M. Jewariya, M. Nagai, and K. Tanaka. Ladder climbing on the anharmonic intermolecular potential in an amino acid microcrystal via an intense monocycle terahertz pulse. *Phys. Rev. Lett.*, 105:203003, 2010.

[70] I.P. Kaminow and W.D. Johnston, Jr. Quantitative determination of sources of the electro-optic effect in $LiNbO_3$ and $LiTaO_3$. *Phys. Rev.*, 160(3):519–522, 1967.

[71] N. Karpowicz, X. Lu and X.-C. Zhang. Terahertz gas photonics. *J. Mod. Opt.*, 56:1137-1150, 2009.

[72] I. Katayama, H. Aoki, J. Takeda, H. Shimosato, M. Ashida, R. Kinjo, I. Kawayama, M. Tonouchi, M. Nagai, and K. Tanaka. Ferroelectric soft mode in a $SrTiO_3$ thin film impulsively driven to the anharmonic regime using intense picosecond terahertz pulses. *Phys. Rev. Lett.*, 108:097401, 2012.

[73] H. Kawashima, M.W. Wefers, and K.A. Nelson. Femtosecond pulse shaping, multiple-pulse spectroscopy, and optical control. *Ann. Rev. Phys. Chem.*, 46:627–656, 1995.

[74] Richard Michael Koehl. *Spatial and Temporal Ultrafast Imaging and Control of Terahertz Wavepackets.* PhD thesis, Massachusetts Institute of Technology, 1995.

[75] R.M. Koehl and K.A. Nelson. Coherent optical control over collective vibrations traveling at light-like speeds. *J. Chem. Phys.*, 114:1443–1446, 2001.

[76] Y.-S. Lee. *Principles of terahertz science and technology.* Springer, 2009.

[77] K.-H. Lin, C.A. Werley, and K.A. Nelson. Generation of multicycle terahertz phonon-polariton waves in a planar waveguide by tilted optical pulse fronts. *Appl. Phys. Lett.*, 95:103304, 2009.

[78] M.E. Lines and A.M. Glass. *Principles and applications of ferroelectrics and related materials.* International series of monographs on physics. Clarendon Press, 1977.

[79] T. Lóffler, T. Hahn, M. Thomson, F. Jacob, and H. Roskos. Large-area electro-optic ZnTe terahertz emitters. *Opt. Express*, 13:5353, 2005.

[80] S.A. Maier. *Plasmonics: Fundamentals and Applications.* Springer, 2007.

[81] A. Mayer and F. Keilmann. Far-infrared nonlinear optics. I. $\chi^{(2)}$ near ionic resonance. *Phys. Rev. B*, 33:6954-6961, 1986.

[82] O.E. Martinez. Pulse distortions in tilted pulse schemes for ultrashort pulses. *Opt. Commun.*, 59:229-232, 1986.

[83] A.A. Maznev, T.F. Crimmins, and K.A. Nelson. How to make femtosecond pulses overlap. *Opt. Lett.*, 23:1378–1380, 1998.

[84] H. Merbold, A. Bitzer, and T. Feurer. Second harmonic generation based on strong field enhancement in nanostructured THz materials. *Opt. Express*, 19:7262, 2011.

[85] D.L. Mills and E. Burstein. Polaritons: the electromagnetic modes of media. *Rep. Prog. Phys.*, 37:817–926, 1974.

[86] M. Nagai, M. Jewariya, Y. Ichikawa, H. Ohtake, T. Sugiura, Y. Uehara, and K. Tanaka. Broadband and high power terahertz pulse generation beyond excitation bandwidth limitation via $\chi^{(2)}$ cascaded processes in $LiNbO_3$. *Opt. Express*, 17:11543, 2009

[87] S. Nakajima, Y. Toyozawa, and R. Abe. *The Physics of Elementary Excitations.* Springer series in solid-state sciences. Springer-Verlag, 1980.

[88] L. Pálfalvi, J. Hebling, J. Kuhl, Á. Péter, and K. Polgár. Temperature dependence of the absorption and refraction of Mg-doped congruent and stoichiometric $LiNbO_3$ in the THz range. *J. Appl. Phys.*, 97:123505, 2005.

[89] Benjamin John Paxton. *Development of Phonon-Polariton THz Spectroscopy, and The Investigation of Relaxor Ferroelectrics.* PhD thesis, Massachusetts Institute of Technology, 2006.

[90] P. Peier, S. Pilz, F. Müller, K.A. Nelson, and T. Feurer. Analysis of phase contrast imaging of terahertz phonon-polaritons. *J. Opt. Soc. Am. B*, 25:B70-B75, 2008.

[91] D. Pines. *Elementary Excitations in Solids.* W. A. Benjamin, New York, 1964.

[92] S.P.S. Porto, B. Tell, and T.C. Damen. Near-forward raman scattering in zinc oxide *Phys. Rev. Lett.*, 16, 450-452, 1966.

[93] T. Qi, Y.-H. Shin, K.-L. Yeh, K.A. Nelson, and A.M. Rappe. Collective Coherent Control: Synchronization of Polarization in Ferroelectric $PbTiO_3$ by Shaped THz Fields. *Phys. Rev. Lett.*, 102, 247603, 2009.

[94] K. Rabe, Ch.H. Ahn, and J.-M. Triscone. *Physics of Ferroelectrics: a modern perspective.* Springer, 2007.

[95] C.V. Raman and K.S. Krishnan. A new type of secondary radiation. *Nature*, 121:501–502, 1928.

[96] Richard N. Zare. Laser control of chemical reactions. *Science*, 279:1875-1879, 1998.

[97] V. Romero-Rochín, R.M. Koehl, C.J. Brennan, and K.A. Nelson. Anharmonic phonon-polariton excitation through impulsive stimulated Raman scattering and detection through wave vector overtone spectroscopy: Theory and comparison to experiments on lithium tantalate. *J. Chem. Phys.*, 111, 3559-3571, 1999.

[98] R. Ruppin and R. Englman. Optical phonons of small crystals. *Rep. Prog. Phys.*, 33:149–196, 1970.

[99] K. Sakai. *Terahertz Optoelectronics.* Springer, 2005.

[100] C.A. Schmuttenmaer. Exploring dynamics in the far-infrared with terahertz spectroscopy. *Chem. Rev.*, 104(4):1759, 2004

[101] C.V. Shank. Investigation of ultrafast phenomena in the femtosecond time domain. *Science*, 233:1276–1280, 1986.

[102] C.V. Shank and E.P. Ippen. Subpicosecond kilowatt pulses from a mode-locked cw dye laser. *Appl. Phys. Lett.*, 24:373–375, 1974.

[103] Y.R. Shen and N. Bloembergen. Theory of stimulated brillouin and raman scattering. *Phys. Rev.*, 137:A1787, 1965.

[104] Joshua Charles Vaughan. *Two-dimensional Ultrafast Pulse Shaping and its Application to Coherent Control and Spectroscopy.* PhD thesis, Massachusetts Institute of Technology, 2005.

[105] A.G. Stepanov, J. Hebling, and J. Kuhl. Generation, tuning, and shaping of narrow-band, picosecond THz pulses by two-beam excitation. *Opt. Express*, 12:4650, 2004.

[106] Nikolay Staykov Stoyanov. *Phonon-Polaritons in Bulk and Patterned Materials.* PhD thesis, Massachusetts Institute of Technology, 2003.

[107] N.S. Stoyanov, D.W. Ward, T. Feurer, and K.A. Nelson. Direct visualization of phonon-polariton focusing and amplitude enhancement. *J. Chem. Phys.*, 117:2897-2901, 2002.

[108] N.S. Stoyanov, D.W. Ward, T. Feurer, and K.A. Nelson. Terahertz polariton propagation in patterned materials. *Nature Materials*, 1:95-98, 2002.

[109] K. Tanaka, H. Hirori, and M. Nagai. THz nonlinear spectroscopy of solids. *IEEE Transactions on Terahertz Science and Technology*, 1:301, 2011

[110] M. Tonouchi. Cutting-edge terahertz technology. *IEEE Nature Photonics*, 1:97-105, 2007

[111] R. Trebino, K.W. DeLong, D.N. Fittinghoff, J.N. Sweetser, M.A. Krumbügel, B.A. Richman, and D.J. Kane. Measuring ultrashort laser pulses in the time-frequency domain using frequency-resolved optical gating. *Rev. Sci. Instrum.*, 68:3277, 1997.

[112] J.C. Vaughan, T. Feurer, and K.A. Nelson. Automated two-dimensional femtosecond pulse shaping. *J. Opt. Soc. Am. B*, 19:2489-2495, 2002.

[113] J.C. Vaughan, T. Hornung, T. Feurer, and K.A. Nelson. Diffraction-based femtosecond pulse shaping with a two-dimensional spatial light modulator. *Opt. Lett.*, 30:323-325, 2005.

[114] T. Volk and M. Wöhlecke. *Lithium niobate: defects, photorefraction and ferroelectric switching.* Springer, 2008.

[115] David Wayne Ward. *Polaritons: An Intermediate Regime Between Electronics and Photonics.* PhD thesis, Massachusetts Institute of Technology, 2005.

[116] D.W. Ward, J.D. Beers, T. Feurer, E.R. Statz, N. Stoyanov, and K.A. Nelson. Coherent control of phonon-polaritons in a terahertz resonator fabricated with femtosecond laser machining. *Opt. Lett.*, 29:2671–2673, 2004.

[117] A.M. Weiner, D.E. Leaird, G.P. Wiederrecht, and K.A. Nelson. Femtosecond pulse sequences used for optical manipulation of molecular motion. *Science*, 247:1317–1319, 1990.

[118] A.M. Weiner, D.E. Leaird, G.P. Wiederrecht, M.J. Banet, and K.A. Nelson. Spectroscopy with shaped femtosecond pulses: styles for the 1990s. In K.A. Nelson, editor, *Picosecond and Femtosecond Spectroscopy from Laboratory to Real World (SPIE Proc. v. 1209)*, pages 14–19, Bellingham, 1990.

[119] A.M. Weiner, D.E. Leaird, G.P. Wiederrecht, and K.A. Nelson. Femtosecond multiple-pulse impulsive stimulated Raman scattering spectroscopy. *J. Opt. Soc. Am. B*, 8:1264–1275, 1991.

[120] A.S. Weling and D.H. Auston. Novel sources and detectors for coherent tunable narrow-band terahertz radiation in free space. *J. Opt. Soc. Am. B*, 13:2783–2791, 1996.

[121] C.A. Werley, Q. Wu, K.-H Lin, C.R. Tait, A. Dorn, and K.A. Nelson. Comparison of phase-sensitive imaging techniques for studying terahertz waves in structured $LiNbO_3$. *J. Opt. Soc. Am. B*, 27:2350, 2010.

[122] C.A. Werley, S.M. Teo, and K.A. Nelson. Pulsed laser noise analysis and pump-probe signal detection with a DAQ card. *Rev. Sci. Inst.*, 82:123108, 2011.

[123] C.A. Werley, K. Fan, A.C. Strikwerda, S.M. Teo, X. Zhang, R.D. Averitt, and K.A. Nelson. Time-resolved imaging of near-fields in THz antennas and direct quantitative measurement of field enhancements. *Opt. Express*, 20:8551-8567, 2012.

[124] G.P. Wiederrecht, T.P. Dougherty, L. Dhar, and K.A. Nelson. Explanation of anomalous polariton dynamics in $LiTaO_3$. *Phys. Rev. B*, 51:916–931, 1995.

[125] K.K. Wong, editor. *Properties of lithium niobate.* Number 28 in EMIS datareviews series. INSPEC/Institution of Electrical Engineers, London, 2002.

[126] Y.-X. Yan, Jr. Edward B. Gamble, and K.A. Nelson. Impulsive stimulated scattering: General importance in femtosecond laser pulse interactions with matter, and spectroscopic applications. *J. Chem. Phys.*, 83:5391, 1985.

[127] Y.-X. Yan and K.A. Nelson. Impulsive stimulated light scattering. i. general theory. *J. Chem. Phys.*, 87:6240–6256, 1987.

[128] Y.-X. Yan and K.A. Nelson. Impulsive stimulated light scattering. ii. comparison to frequency-domain light scattering spectroscopy. *J. Chem. Phys.*, 87:6257–6265, 1987.

[129] C.L. Yang, Q. Wu, J.J. Xu, K.A. Nelson, and C.A. Werley. Experimental and theoretical analysis of THz-frequency, direction-dependent, phonon polariton modes in a subwavelength, anisotropic slab waveguide. *Opt. Express*, 18:26351, 2010.

[130] K.H. Yang, P.L. Richards, and Y.R. Shen. Generation of far-infrared radiation by picosecond light pulses in $LiNbO_3$. *Appl. Phys. Lett.*, 19:320, 1971.

[131] R. Yano and H. Gotoh. Tunable terahertz electromagnetic wave generation using birefringent crystal and grating pair. *Jpn. J. Appl. Phys.*, 44:8470–8473, 2005.

[132] K.-L. Yeh, M.C. Hoffmann, J. Hebling, and K.A. Nelson. Generation of 10 μJ ultrashort THz pulses by optical rectification. *Appl. Phys. Lett.*, 90:171121, 2007.

[133] K.-L. Yeh, J. Hebling, M.C. Hoffmann, and K.A. Nelson. Generation of high average power 1 kHz shaped THz pulses via optical rectification. *Opt. Comm.*, 13:3567–3570, 2008.

[134] K.-L. Yeh, T. Hornung, J.C. Vaughan, and K.A. Nelson. Terahertz amplification in high-dielectric materials. In P. Corkum, D. Jonas, D. Miller, and A.M. Weiner, editors, *Ultrafast Phenomena XV*, pages 802–804, Berlin, 2007. Springer-Verlag.

[135] K.-L. Yeh, E.R. Statz, J.C. Vaughan, T. Hornung, and K.A. Nelson. Terahertz polaritonics: High-field THz coherent control and spectroscopy. *Lasers and Electro-Optics Society, 2006. LEOS 2006. 19th Annual Meeting of the IEEE*, pages 138–139, Oct. 2006.

[136] Ka-Lo Yeh. *The generation of high field terahertz radiation and its application in nonlinear spectroscopy.* PhD thesis, Massachusetts Institute of Technology, 2009.

[137] X. Zhou, Z. Chen, C.A. Werley, H.Y. Hwang, and K.A. Nelson. High power single-cycle and tunable multi-cycle terahertz generation by phase-matched optical rectification. *CLEO:2011 - Laser Applications to Photonic Applications*, OSA Technical Digest, paper CMW3, Optical Society of America, 2011.

[138] O.C. Zienkiewicz, R.L. Taylor, and J.Z. Zhu. *Finite Element Method - Its Basis and Fundamentals.* Elsevier, sixth edition, 2005.